Washington University in St. Louis

Washington University Open Scholarship

Winter 12-15-2021

An Investigation of Sensory Percepts Elicited by Macro-Sieve Electrode Stimulation of the Rat Sciatic Nerve

Nikhil Shiva Chandra
Washington University in St. Louis

WASHINGTON UNIVERSITY IN ST. LOUIS

School of Engineering & Applied Sciences
Department of Biomedical Engineering

Dissertation Examination Committee:

Daniel Moran, Chair
Wilson Ray, Co-Chair
Dennis Barbour
Harold Burton
Leonard Green
Matthew MacEwan

An Investigation of Sensory Percepts Elicited by Macro-Sieve
Electrode Stimulation of the Rat Sciatic Nerve
by
Nikhil Shiva Chandra

A dissertation presented to
The Graduate School
of Washington University in
partial fulfillment of the
requirements for the degree
of Doctor of Philosophy

December 2021
St. Louis, Missouri

Table of Contents

List of Figures

List of Tables

Acknowledgments

Nikhil Shiva Chandra

Washington University in St. Louis

December 2021

Dedicated to my parents.

ABSTRACT OF THE DISSERTATION

Intuitive control of conventional prostheses is hampered by their inability to replicate the rich tactile and proprioceptive feedback afforded by natural sensory pathways. Electrical stimulation of residual nerve tissue is a promising means of reintroducing sensory feedback to the central nervous system. The macro-sieve electrode (MSE) is a candidate interface to amputees' truncated peripheral nerves whose unique geometry enables selective control of the complete nerve cross-section. Unlike previously studied interfaces, the MSE's implantation entails transection and subsequent regeneration of the target nerve. Therefore, a key determinant of the MSE's suitability for this task is whether it can elicit sensations at low current levels in the face of altered axon morphology and caliber distribution inherent to nerve regeneration.

This dissertation describes a combined rat sciatic nerve and behavioral model that was developed to answer this question. Four rats learned a go/no-go detection task with auditory stimuli and then underwent surgery to implant the MSE in the sciatic nerve. After healing, they returned to behavioral training and transferred their attention to monopolar electrical stimuli presented in one multi-channel and eight single-channel stimulus configurations. Current amplitudes varied based on the method of constant stimuli (MCS). A subset of single-channel configurations was tested longitudinally at two timepoints spaced three weeks apart.

Psychometric curves generated for each dataset enabled the calculation of 50% detection thresholds and associated slopes. For a given rat, the multi-channel configuration's per-channel current requirement for stimulus detection was lower than all corresponding single-channel thresholds. Single-channel thresholds for leads located near the nerve's center were, on average, half those of leads located more peripherally. Of the five leads tested longitudinally, three had

thresholds that decreased or remained stable over the three-week span. The remaining two leads' thresholds showed a significant increase, possibly due to scarring or device failure. Overall, thresholds for stimulus detection were comparable with more traditional penetrative electrode implants, suggesting that the MSE is indeed viable as a sensory feedback interface.

These results represent an important first step in establishing the MSE's suitability as a sensory feedback interface for integration with prosthetic systems. More broadly, it lays the groundwork for future experiments that will extend the described model to the study of other devices, stimulus parameters, and task paradigms.

Chapter 1: Introduction

Amputees face numerous challenges in coming to terms with limb loss, including reduced independence, degraded mobility, attenuated dexterity, despair over disfigurement, fear of stigmatization, and perceived diminishment of personal and professional prospects. The prevalence of depression and anxiety is higher among amputees compared with the general population (Shukla et al., 1982; Pillet and Didierjean-Pillet, 2001; Darnall et al., 2005). Advanced prosthetic limb replacements can play an important role in overcoming these challenges and improving the quality of amputees' lives.

Conventional prostheses cannot replicate the rich tactile and proprioceptive feedback afforded by the body's natural sensory pathways. Amputees compensate for this deficiency by allocating more visual attention than would otherwise be needed to maintain effective, closed-loop control. This is a significant cause of reported dissatisfaction with and abandonment of prosthetic devices (Biddiss and Chau, 2007). The development of technologies that can endow prostheses with useful sensory feedback is an area of active research.

Early attempts to incorporate feedback used mechanical means to transmit pressure information from prosthetic fingertips to the amputee's stump (Rosset, 1916; Conzelman et al., 1953). Later efforts shifted their focus to the creation of "cutaneous displays" whereby sensory information was transmitted to the stump skin using vibrators or electrical stimulators (Beeker et al., 1967; Mann and Reimers, 1970; Prior et al., 1976; Shannon, 1979). In the past two decades, a promising approach that has gathered momentum makes use of residual nerves' retained ability to transmit signals associated with original innervation targets even years after the amputation took place (Dhillon et al., 2004). The goal is to use implanted electrodes to relay sensory information from

prosthetic sensors and reintroduce sensory feedback to the central nervous system (Dhillon and Horch, 2005; Raspopovic et al., 2014; Tan et al., 2015; Davis et al., 2016; Charkhkar et al., 2018; Petrini et al., 2019).

An electrode's suitability as a sensory interface depends in part on the extent to which elicited sensations are perceived to originate from distinct locations in the phantom limb. Peripheral nerve axons are somatotopically organized, as axons with shared innervation targets remain clustered together throughout the nerve's length and up to the spinal cord (Hallin, 1990; Brushart, 1991). Therefore, a key metric of an electrode's performance is its ability to recruit discrete axon bundles throughout the nerve cross-section independently of one another, i.e., its "selectivity." Selectivity derives from the proximity of an electrode's leads to target axons as nearby axons can be activated by lower currents than axons further away. Lower currents are also associated with limited nerve damage and realistic percepts without paresthesia.

Numerous electrodes have emerged over the years, offering progressively greater intimacy with and selective control over target axons by deforming or penetrating the nerve (Navarro et al., 2005). The least invasive is the extraneural cuff electrode (ECE), whose leads abut the nerve perimeter and confer limited control of interior axons (Veraart et al., 1993). The flat-interface nerve electrode (FINE) brings interior axons closer to surface leads by flattening the nerve (Tan et al., 2014, 2015; Charkhkar et al., 2018). The longitudinal intrafascicular electrode (LIFE) is a thin, insulated filament that is inserted axially into a nerve fascicle and provides selective control of the fascicle with its exposed tip. This design is impractical for the control of multiple fascicles, which would require the separate insertion of multiple filaments (Lefurge et al., 1991; Dhillon et al., 2004). The transverse intrafascicular multichannel electrode (TIME) is also a filament design, but

overcomes the LIFE's single-fascicle limitation by penetrating the nerve perpendicularly so that leads distributed along its length can interface with different fascicles for wider nerve coverage (Boretius et al., 2010; Raspopovic et al., 2014; Petrini et al., 2019). The Utah slanted electrode array is a 2-dimensional grid of 96 metallic tines that penetrate the nerve to different depths so that each tine controls its own share of axons within the nerve's cross-section (Davis et al., 2016).

Regenerative electrodes (RE) take a different route to achieve axon intimacy. The archetypal RE is a flat disk that is implanted between the severed stumps of a transected nerve using attached conduits. These guide regenerating axons from the proximal stump through "transit zones" perforating the RE's surface to create a robust mechanical coupling between the RE and nerve structure. Interspersed leads provide selective recording and stimulation of axons.

In recent years, our group at Washington University has developed a new type of RE called the macro-sieve electrode (MSE; MacEwan et al., 2016). The MSE distinguishes itself from more typical RE designs with its nine exceptionally large transit zones, which collectively occupy an area greater than 2 mm^2 and are minimally obstructive to axon growth. The transit zones' boundaries are defined by a central hub and eight radiating spokes that together house eight metallized leads – four "core" channels located on the central hub (labeled C1, C2, C3, and C4), and four "peripheral" channels located on alternating spokes (labeled P1, P2, P3, and P4). Simulations have shown that with these eight leads, the MSE can selectively recruit axon clusters with wide nerve coverage by the coordinated application of cathodic and anodic currents (i.e., current steering; Zellmer, 2014). This sets it apart from other interfaces that seek greater selectivity by increasing the number of channels (e.g., Tan et al., 2014; Davis et al., 2016). The robust

stability, close intimacy with target axons, and selective control afforded by the MSE's regenerative design make it an attractive candidate for delivering sensory feedback.

Regenerated axons differ markedly from their undisrupted counterparts in both morphology and caliber distribution, with thinner myelin sheaths, a tendency towards smaller calibers, and shorter separation between the nodes of Ranvier (Beuche and Friede, 1985; Friede and Beuche, 1985; Negredo et al., 2004; Castro et al., 2008). Accordingly, the electrophysiological response of regenerated axons interfaced by the MSE should diverge from that of undisrupted axons interfaced by the more conventional electrodes described in previous paragraphs. Prior simulation work by our group has shown that regenerated axons' recruitment thresholds should not be inherently higher or lower than those of undisrupted axons. Instead, regenerated axons near the stimulating lead should have lower thresholds than corresponding undisrupted axons, while those further away should have higher thresholds (Zellmer et al., 2018). This result is instructive as it suggests that the MSE can indeed elicit localizable sensory percepts at current amplitudes comparable with other interfaces. However, establishing the MSE's suitability as a sensory feedback interface for clinical applications cannot rely solely on simulations – it requires *in vivo* measurements of stimulus detection thresholds and discriminability.

Conventionally, the assessment of an electrode's performance as a sensory feedback interface has relied on reports by implanted human subjects of felt sensations triggered by different stimulus configurations. (Dhillon and Horch, 2005; Raspopovic et al., 2014; Tan et al., 2014, 2015; Davis et al., 2016; Charkhkar et al., 2018; Petrini et al., 2019). This approach precludes the testing of early-stage devices such as the MSE, with its invasive and irreversible implantation procedure. Animal models can lay the groundwork for future clinical studies in humans.

Rodent behavioral models have long provided a useful vehicle for the systematic investigation of various sensory modalities (Laing et al., 1974; Kelly and Masterton, 1977; Uchida and Mainen, 2003; Otto et al., 2005; Gaese et al., 2006; Stuttgen et al., 2006; Butovas and Schwarz, 2007; Huber et al., 2008; Adibi and Arabzadeh, 2011; Mayrhofer et al., 2013). Additionally, the rat sciatic nerve has long been a preferred model for the investigation of peripheral nerve injury and repair (Savastano et al., 2014). Together, these facts motivated the development of a combined rat sciatic nerve and behavioral model (CRSNB model) for the characterization of sensory percepts elicited by MSE stimulation. It is this model that forms the topic of this dissertation.

1.1 Research Objectives

The central aim of this project was to apply the CRSNB model to the measurement of detection thresholds and slopes for various MSE stimulus configurations. Implanted rats performed a go/no-go detection task based on the method of constant stimuli (MCS) for one "multi-channel" stimulus configuration in which all eight MSE channels passed equal currents simultaneously, and for eight "single-channel" configurations in which each channel passed current alone. The resulting data enabled the derivation of psychometric curves depicting the probability of stimulus detection as a function of current amplitude. These curves allowed the calculation of detection thresholds, i.e., current amplitudes for which the likelihood of detection was 50%, and of associated slope values that measured the sensitivity of detection likelihood to changes in current amplitude.

Calculated threshold and slope values provided valuable insights into the MSE's performance as a sensory feedback interface. In particular, they confirmed our intuition that the multi-channel configuration's per-channel current requirement for stimulus detection should be lower than all corresponding single-channel thresholds. They further demonstrated that single-channel detection

thresholds were not uniform across the nerve, as thresholds for core channels were approximately half those for peripheral channels. Finally, they permitted a preliminary assessment of longitudinal device stability that produced mixed but somewhat encouraging results.

1.2   Structure of the Dissertation

This dissertation describes the development of the CRSNB model and its application to the measurement of current detection thresholds under MSE stimulation. It is divided into five chapters. The present chapter (Chapter 1**)** introduces the research topic and gives an outline of the research objectives (i.e., specific aims).

Chapter 2 gives an in-depth account of the history of prosthetics, the etiology and epidemiology of limb amputation, the types of prostheses in prevalence today, and the importance of sensory feedback. It goes on to discusses the structure of the nervous system (with particular emphasis on the peripheral nervous system) and the membrane dynamics underlying the action potential. It then provides an overview of the different types of electrodes that have been used to provide sensory feedback, the evolution of REs, and the development of the MSE.

Chapter 3 describes all aspects of the development of the CRSNB model and its application to the measurement of detection thresholds. It describes in detail the construction and programming of the experimental apparatus. It describes the methods used to train the rats on a go/no-go detection task using auditory stimuli, the surgical procedure, and how the healed rats then resumed training on the detection task and transitioned from auditory to electrical stimulation. It concludes with a comprehensive explanation of the methods used to generate psychometric curves, assess goodness of fit, identify outliers, calculate thresholds and slopes, and estimate confidence intervals.

Chapter 4 provides a detailed account of the CRSNB model's execution for four rats over a two-year period. It provides a detailed account of the data collection for each rat and presents the results of the analysis that followed. It further interprets these results in the context of assessing the MSE's suitability as a sensory feedback interface.

Chapter 5 is more speculative than the preceding chapters as it explores different ideas for improving the CRSNB model and carrying it forward. It begins with an examination of whether choices made early in the model's design could have impacted measured threshold and slope values. It next offers a series of recommendations for increasing the efficiency of data collection. It concludes with suggestions for future simulation studies, for ways to extend the CRSNB model beyond the measurement of thresholds and slopes, and for other electrode interfaces that would be ideal candidates for testing with this model.

Chapter 2: Background

The following chapter discusses at length the etiology and epidemiology of limb loss, the history and classification of upper-limb prosthetic implements, past attempts to imbue prostheses with feedback, the organization and function of the peripheral nervous system, the fundamentals of nerve excitation, the design of various peripheral nerve interfaces, the evolution of regenerative electrodes, our group's development of the macro-sieve electrode, and an overview of rodent behavioral models and psychophysics.

2.1   Limb Loss in the United States

The number of Americans living with limb loss today exceeds 1.6 million, and this number is projected to more than double by 2050 (Ziegler-Graham et al., 2008). Lower limb amputations constitute roughly 65% of the total, and nearly 80% of these are caused by dysvascular disease. In contrast, the vast majority (92%) of upper limb amputations are caused by trauma. **Figure 2.1** summarizes these data. Dillingham et al. (2002) provides a more comprehensive breakdown of limb loss by amputation level. These data are summarized for upper-limb amputees in **Table 2.1**. It is notable that the vast majority of upper-limb amputations (91.9%) are at or below the level of the wrist. The next two most prevalent levels are transradial (3.5%) and transhumeral (3.0%) amputations. Less than 2% of the total are through-elbow, shoulder, bilateral, or forequarter.
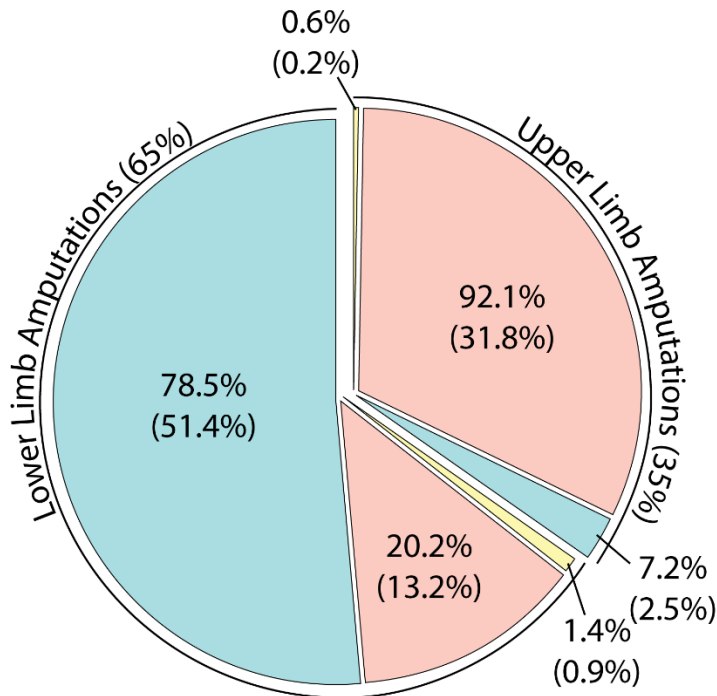
Figure 2.1: Breakdown of limb amputations by type and etiology in 2005 (adapted from Ziegler-Graham et al., 2008). There are two types – lower limb and upper limb. There are three etiologies – dysvascular disease (blue), trauma (red), and cancer (yellow). Each slice of the pie chart has two percentages. The top percentage is the proportion of amputations of the slice's type to have the slice's etiology. The bottom percentage (in parentheses) is the proportion of all amputations caused by the slice's type/etiology combination. Thus, 78.5% of lower-limb amputations proceed from dysvascular disease, while 51.4% of all amputations are of the lower limbs and caused by dysvascular disease.

Table 2.1: Breakdown of upper-limb amputations based on hospital discharges from 1988-1996 (Dillingham et al., 2002).

Level	Total (%)
Total	166,076 (100%)
Wrist and Below	152,573 (91.9%)
Transradial	5,839 (3.5%)
Through-Elbow	854 (0.5%)
Transhumeral	5,007 (3.0%)
Shoulder	755 (0.5%)
Bilateral	462 (0.3%)
Forequarter	586 (0.4%)
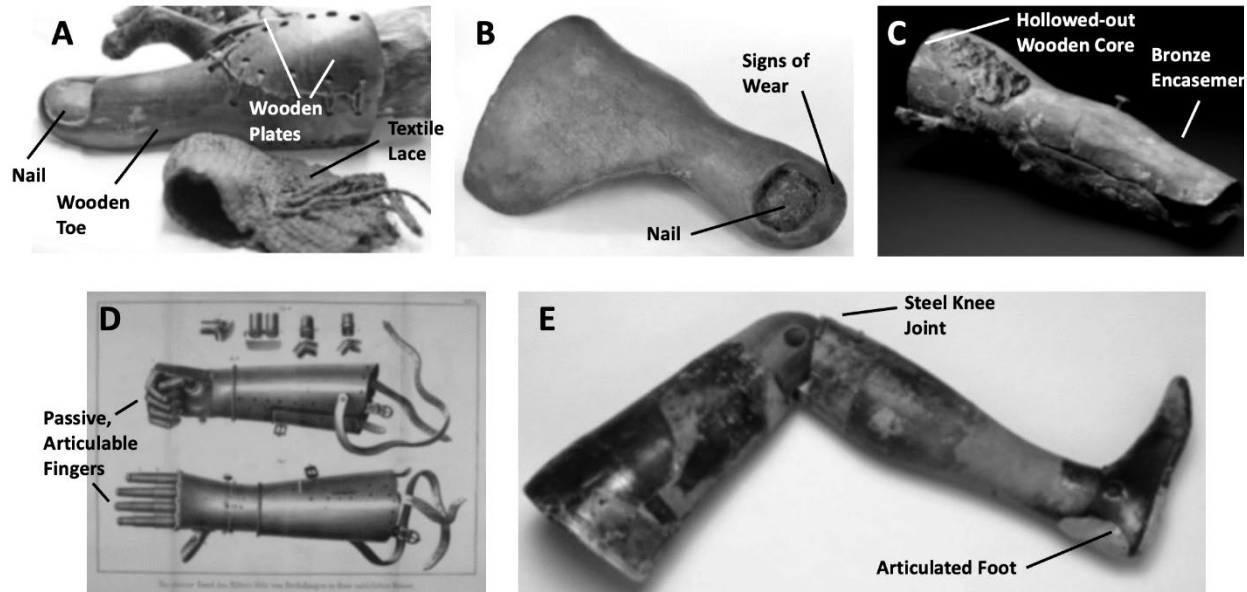
Figure 2.2: (A) Prosthetic toe from Egypt's 18th dynasty (adapted from Finch, 2011). (B) Greville Chester Toe (adapted from Finch, 2011). (C) Capua Leg (adapted from Otte and Hazubski, 2021). (D) Engraving of the second iron hand of Götz von Berlichingen (adapted from Ashmore et al., 2019). (E) Anglesey Leg (adapted from Thurston, 2007).

2.2   Prosthetics Use Through the Ages

Ancient history is replete with stories of prosthetic replacements for body parts lost to injury or disease. The Hindu *Rig Veda* (circa 2,000 BCE) tells the tale of the warrior queen Vishpala who, after losing a leg on the battlefield, wore an iron prosthesis so she could fight once more. The Greek historian Herodotus (484-425 BCE) wrote of Hegesistratus, who escaped Spartan captivity by cutting off his own foot and replacing it with a wooden substitute. Pliny the Elder (23-79 CE) describes a hand of iron constructed for the Roman general Marcus Sergius, who fought and was injured in the 2nd Punic War (218-201 BCE). In each case, no physical artifact exists to confirm the account.

The oldest limb prosthesis in actual possession was discovered during the excavation of an Egyptian tomb dating back to the 18th dynasty (circa 1550-1300 BCE). The mummy of a middle-aged woman was found whose right big toe had been amputated and replaced with a wooden

prosthesis in three parts – a longitudinal wooden corpus that formed the main body of the toe and two wooden plates (**Figure 2.2A**). The toe was fashioned realistically and even included a nail. It was affixed firmly to the wearer by wrapping a broad textile lace around the forefoot. This allowed the wearer to move freely without compromising stability. Indeed, the sole of the prosthetic toe shows obvious marks of use (Nerlich et al., 2000).

Another well-known example of Egyptian prosthetic technology is the Greville Chester Toe, acquired by the British Museum in 1881 (**Figure 2.2B**). Its construction has been dated to before 600 BCE, and in appearance it resembles the right big toe and a portion of the foot. The toe appears to have served both cosmetic and functional purposes, as careful examination reveals that it once carried a false nail and shows clear signs of wear in several locations (Finch, 2011).

The ancient Romans also left behind evidence of prosthetic engineering. Perhaps the most prominent example is the Capua leg, named for the site of its 1884 excavation in Capua, Italy (**Figure 2.2C**). Believed to have been built circa 300 BCE, it consisted of a hollowed-out wooden core encased in bronze. The wooden core's interior hollow was padded with cloth to accommodate the wearer's stump. The device was probably worn with the aid of leather straps tied to a bronze waistband. It was destroyed in a German bombing raid of London during World War II (Finch, 2011; Otte and Hazubski, 2021).

The emergence of gunpowder at the dawn of Europe's renaissance saw a marked increase in limb amputation among soldiers. In 1504, a German knight named Gottfried "Götz" von Berlichingen lost his right hand in battle after being struck by a cannonball splinter. Over the next quarter century, he would go on to commission two "iron hands" – the first shortly after his injury, and the second around 1530. The first iron hand had three finger blocks (corresponding to the thumb,

the index and middle fingers, and the ring and little fingers, respectively) that could be locked in position with a spring mechanism and released by pressing a button. The second was more realistic in appearance, with five articulated fingers that could be positioned passively (**Figure 2.2D**). Despite its inferior appearance, the first iron hand's ability to grip objects firmly afforded it great versatility – numerous accounts exist of how von Berlichingen used it to hold cutlery, grasp a shield, control a horse's reins, and write with a quill (Otte, 2020).

A noted prosthetist of the same era was Ambroise Paré (1510-1590), often credited as one of the fathers of modern surgery. Noting the desperation and suicidality of soldiers following limb amputation, he set about devising artificial limbs to restore their will to live (Hernigou, 2013). He designed a mechanical leg prosthesis with a fixed equinus position, a locking knee, and a suspension harness – features that remain in use to the present day (Thurston, 2007). He also built a mechanical hand called "Le Petit Lorrain" that was operated by catches and springs and worn into battle by a French Army captain in 1551 (Thurston, 2007).

In 1815, Henry William Paget, Earl of Uxbridge and commander of British forces in the Battle of Waterloo, was struck in the right knee necessitating amputation. He later wore a prosthetic leg, developed by James Potts, that came to be known as the Anglesey Leg (**Figure 2.2E**). Constructed primarily of wood, it had a knee joint of steel whose movement was synchronized with an articulated foot using catgut tendons (Thurston, 2007). The Anglesey leg was brought to America, where it was improved upon by Benjamin Franklin Power with the addition of a heel spring. This variation came to be known as the "American Leg."

The American Civil War (1861-1865) deprived thousands of soldiers of their limbs, spurring an era of exciting innovations in prosthetics design. Many soldiers themselves took an interest in the

field. Notable among these was James Edward Hanger, a Confederate soldier who at 18 became the first recorded casualty to lose a limb in the war. Frustrated with the shortcomings of his standard issue replacement leg, he started designing his own devices with improved hinging, rust-free levers, and rubber pads. He went on to found Hanger, Inc., which remains one of the largest manufacturers of prosthetic devices today (Labbe, 2018).

The 20th Century was witness to many gigantic leaps in prosthetics technology. Dorrance's invention of the split hook in 1912, coupled with the invention of the Bowden cable, gave rise to the body-powered family of prostheses that remains in use today. The computer age brought with it sophisticated microcontrollers that led to the emergence of another class of prostheses, which detected minor movements of residual stump musculature and translated these into control signals for electrically actuated joints (i.e., EMG prostheses). I discuss the state of modern upper-limb prostheses in greater detail in the next section.

2.3 Classification of Modern Upper-Limb Prostheses

Upper-limb prostheses fall into two main groups – passive and active. Passive prostheses lack internal mechanisms for joint actuation and rely instead on manual adjustment. They may serve a primarily cosmetic function, although some passive prostheses are capable of grasping objects if appropriately positioned by the other hand. Active prostheses do possess internal mechanisms for joint actuation. They come in two varieties – body-powered and myoelectric (or electrically-powered). **Figure 2.3** depicts this classification scheme.
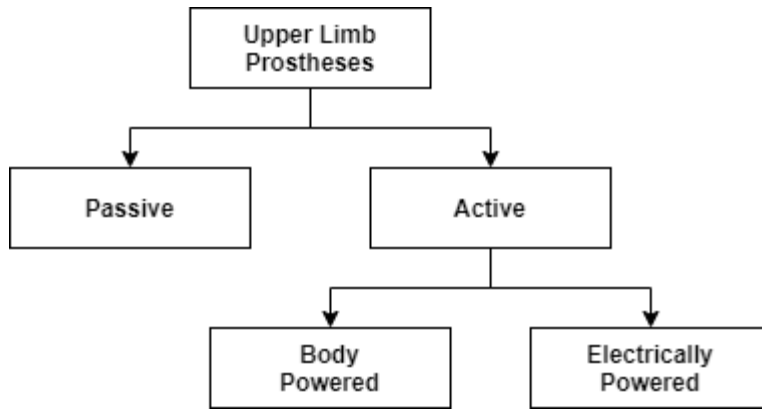
Figure 2.3: Classification of upper-limb prostheses in the present day.

2.3.1 Body-Powered Prostheses

Body-powered prostheses (BPPs) use mechanical means to translate the movement of an intact

body part into a joint actuation at the terminal device (**Figure 2.4A**). A typical BPP has a Bowden

cable that is attached to a fixed anchor point at one end, and to an actuating joint at the other end.

Moving the terminal device away from the anchor point increases tension in the Bowden cable,

pulling on the joint and opening the terminal device. Returning the terminal device to its original

location releases the tension, allowing a spring to actuate the joint in the opposite direction and the

terminal device to close. Given the limited number of degrees of freedom, users of these prostheses

generally prefer hook-shaped over hand-shaped terminal devices, sacrificing cosmesis for greater

ease of movement and visibility of manipulated objects (Biddiss and Chau, 2007).

2.3.2 Myoelectric Prostheses

Myoelectric prostheses (MEPs) use electrodes to detect electromyographic (EMG) activity

generated by the contraction of residual musculature, and onboard microcontrollers to translate

these into control signals for electrically actuated joints (**Figure 2.4B**). The level of amputation

(corresponding to the degree of residual muscular preservation) dictates how many movements

may be controlled independently. The use of microcontrollers enables the coordinated actuation
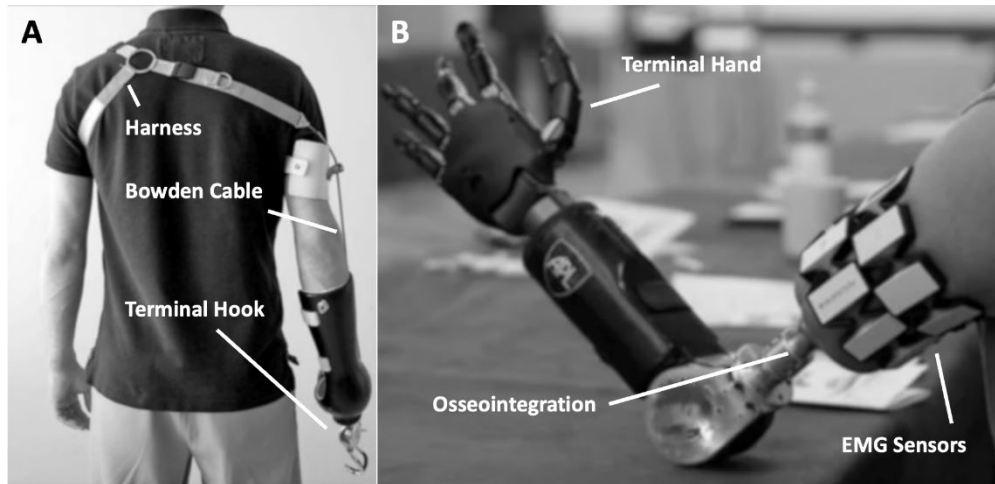
Figure 2.4: (A) A body-powered prosthesis with a terminal hook (adapted from Berning et al., 2014). **(B)** An osseointegrated myoelectric prosthesis with a terminal hand (adapted from Arm Dynamics' website[1]).

of multiple joints using a small number of control signals, making MEPs well-suited to terminal devices with superior cosmesis and greater versatility than the hooks typically associated with BPPs. Multi-functional design allows users to switch between different modes of operation, extending MEPs' usefulness to a multitude of tasks (Meijer and Nazarpour, 2014).

Targeted Muscle Reinnervation

MEPs' electrodes are often housed in the prosthetic socket to allow detection of muscle contractions in the limb stump. Patients with transhumeral or shoulder amputations that leave little stump musculature intact may undergo a procedure called "targeted muscle reinnervation," wherein residual nerves are redirected to the chest and anastomosed with the pectoralis major muscle (**Figure 2.5**). The resulting transfer of motor function means that motor commands sent to the missing limb produce contractions in the chest. An array of electrodes placed across the newly

---

[1] Arm Dynamics (accessed October 2021) https://www.armdynamics.com/research-and-technology/prosthetic-technology
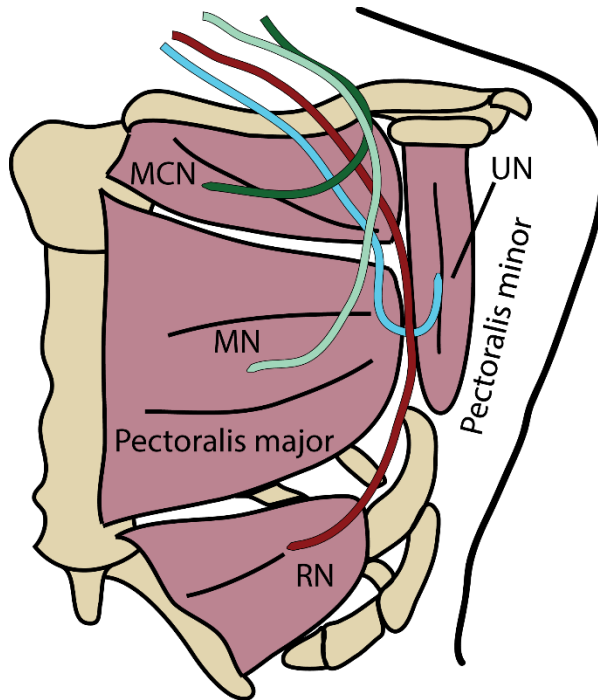
Figure 2.5: Targeted muscle reinnervation. Without a limb stump from which to detect EMG signals, surgical redirection of truncated nerves to the chest musculature produces a concomitant transfer of motor function (adapted from Kuiken et al., 2011).

innervated chest muscles detects these contractions providing a basis for prosthetic control (Kuiken et al., 2004; Kuiken, 2006; Kuiken et al., 2007b, 2011).

2.4 Natural Mechanisms of Sensory Feedback

Natural sensory pathways provide a rich tapestry of tactile and proprioceptive information that plays a crucial role in the execution of movements and the manipulation of objects. Specialized structures called "mechanoreceptors" transduce specific stimuli into action potentials that travel down associated afferents to the central nervous system where they are perceived as sensations. The principle of mechanoreceptor operation is independent of location, modality, receptive field, and spatial acuity: Surface deformation of a stimulated mechanoreceptor alters the permeability of ion-channels in its associated afferent, inducing a depolarizing current. Sufficient depolarization

triggers one or more action potentials that ultimately propagate to the brain's somatosensory cortex. (I discuss in detail nerve cells, ion-channels, and the transmission of action potentials later in this chapter.)

Cutaneous mechanoreceptors provide tactile feedback from objects in contact with the skin. Their distribution is especially dense in the glabrous surface of the human hand and foot (Johansson and Vallbo, 1983). They may be classified based on their response to sustained skin indentation: slowly-adapting (SA) units respond with a sustained discharge of action potentials; fast-adapting (FA) units respond with a burst of action potentials at stimulus onset and cessation. Thus, SA units are more suited to the detection of force and pressure, whereas FA units are more suited to the detection of motion. A second mode of classification is based on receptive field characteristics. Type I units have small receptive fields with well-defined boundaries; Type II units have larger fields whose boundaries are less distinct (Johansson and Vallbo, 1983).

Specific cutaneous mechanoreceptors include FA-I units (also known as Meissner corpuscles) that reside in the dermal papillae close to the skin's surface. With their dense distribution and rapid adaptation to skin deformation, they are highly sensitive to motion and low frequency vibration making them well-suited to the detection of movement and grip. SA-I units (Merkell cells) sit on the tips of epidermal sweat ridges. Like Meissner corpuscles, they too are densely distributed but have much smaller receptive fields. Their slow adaptation to sustained deformation makes them ideally suited to the detection of form and texture. FA-II units (Pacinian corpuscles) lie deep in the subcutaneous layer. Their vast receptive fields and low spatial acuity make them especially sensitive to distant vibrations arising from tool manipulation. SA-II units (Ruffini endings) reside in the dermis layer. They have large receptive fields, low density, poor spatial acuity, and adapt
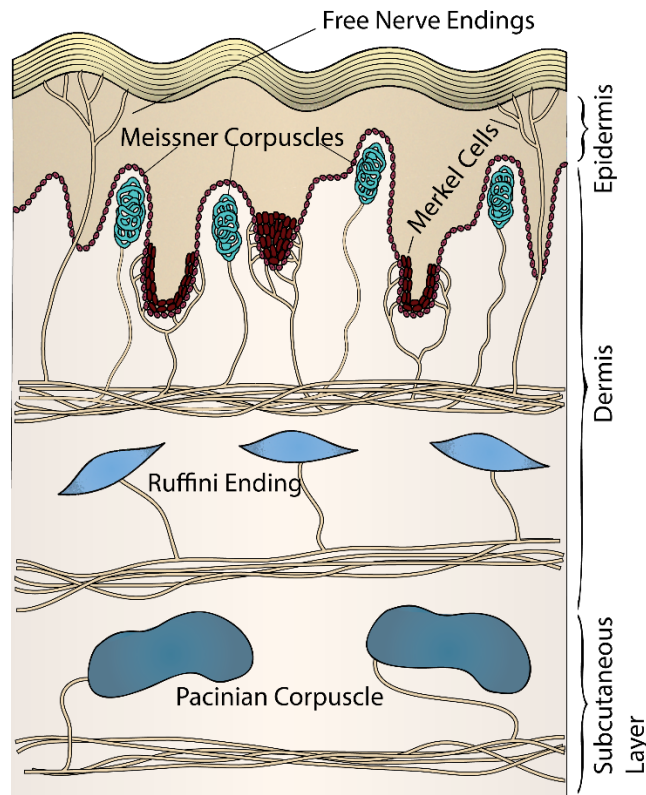
Figure 2.6: Cutaneous mechanoreceptors in the glabrous skin of the human hand. Adapted from Purves et al. (2012).

slowly to sustained deformation. These attributes make them particularly sensitive to skin stretch – they play an important role in the detection of tangential forces, hand shape, and movement direction (Purves et al., 2012). **Figure 2.6** depicts the distribution of cutaneous mechanoreceptors in the glabrous skin of the human hand.

Proprioceptive mechanoreceptors provide information about body position and orientation. They include muscle spindles and Golgi tendon organs. Muscle spindles consist of 4-8 intrafusal muscle fibers encapsulated by a layer of connective tissue; afferent axons wrapped around these fibers have mechanically-activated ion-channels that open as the muscle stretches, triggering action potentials. Afferents come in two varieties: Group Ia afferents are fast-adapting and report the rate of muscle length change; Group II afferents adapt more slowly and report instantaneous muscle

length. Golgi tendon organs comprise Group Ib afferents that are interspersed among tendons'

collagen fibers. They estimate muscle tension, and hence give an idea of how much the muscle is

loaded.

Yet another mode of classification identifies mechanoreceptors by associated fiber type.

Proprioceptive mechanoreceptors have large, myelinated fibers (Aα) with high conduction

velocities up to 120 m/s. Cutaneous mechanoreceptors have slightly smaller myelinated fibers

(Aβ) with conduction velocities up to 75 m/s. Nociceptive and thermoceptive units have small,

myelinated fibers (Aδ) that conduct signals at up to 30 m/s, or miniscule unmyelinated fibers (C)

that conduct at up to 2 m/s.

2.5   Sensory Feedback in Prostheses

Childress (1973) proposed three pathways for closed-loop control in a prosthetic system, labeled

A, B, and C. Pathway A passes audio and visual cues directly to the central nervous system via the

sense organs and is prevalent across all prosthetic systems existent today. Pathway B derives

sensory information from embedded prosthetic sensors and transmits them to the user via
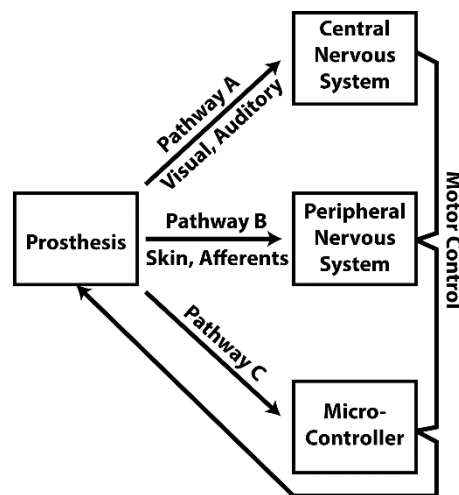
Figure 2.7: Three feedback pathways for closed-loop control of a prosthesis (adapted from Childress, 1973).

19

cutaneous or peripheral nerve stimulation. Pathway C also derives sensory information from sensors but transmits it to controller circuits that generate artificial reflexes, bypassing the need for conscious user response. These pathways are depicted pictorially in **Figure 2.7**.

Despite MEPs' reputation as newer and more "high-tech" options, BPPs retain their popularity because the direct mechanical linkage (Bowden cable) between the terminal device and shoulder harness enables the transmission of force feedback. This allows the user to develop internal schemes for closed-loop force control, reducing but not eliminating the need for compensatory visual attention (Brown et al., 2017). In contrast, MEPs possess no inherent mechanism for force or haptic feedback. Their users must rely heavily on visual cues, and to a lesser extent, auditory and vibratory cues originating from actuating motors, to bridge the feedback gap and maintain effective control (Brown et al., 2017). Users of BPPs and MEPs especially report the need for excessive visual attention as a significant contributor to device dissatisfaction (Atkins et al., 1996; Biddiss and Chau, 2007). Technology that provides sensory feedback for closed-loop control can help to alleviate this problem.

2.5.1 Modes of Prosthetic Sensory Feedback

Antfolk et al. (2013) described two categories of sensory feedback for upper-limb prostheses: modality-matched and sensory-substitution. Modality-matched feedback uses the same modality as the sensory input to deliver information to the user. Sensory-substitution feedback reports one modality of sensory information using another modality.
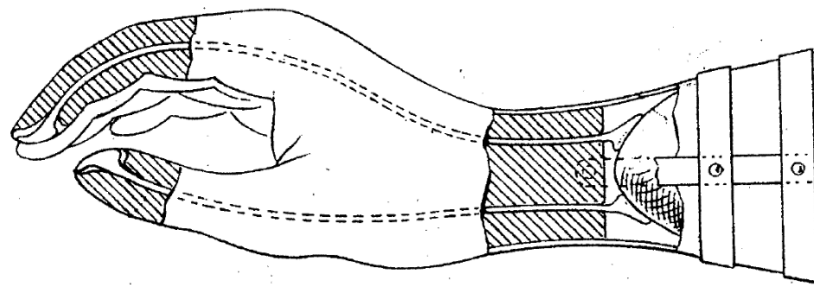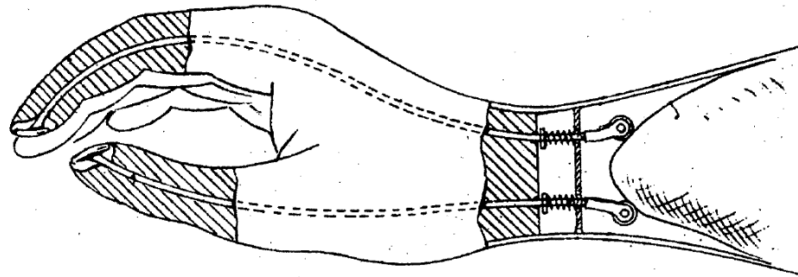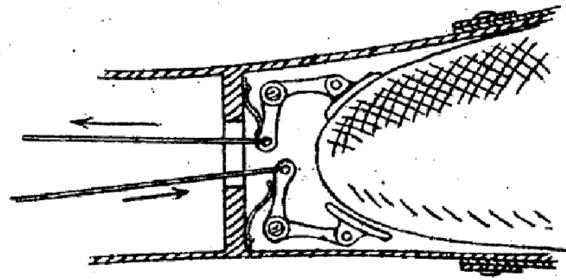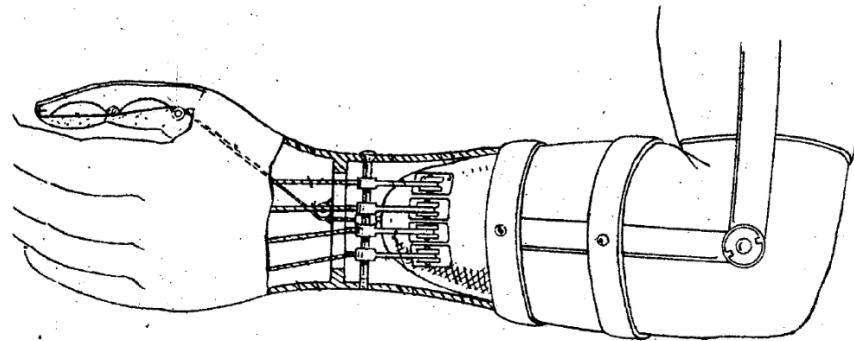
Figure 2.8: Mechanisms for integrating sensory feedback with a hand prosthesis proposed by Rosset (1916).

Modality-Matched Feedback

An early example of modality-matched feedback was Rosset's (1916) patented mechanism to transmit finger pressure to an amputee's stump using wooden or metallic rods attached to the fingertips of a prosthetic hand. The rods' other ends lay in loose contact with the stump. Longitudinal displacement of the rods by pressure exerted at the fingertips would cause them to press against the stump, providing a modicum of displaced haptic feedback. Rosset also proposed an alternative pneumatic mechanism in which the rods were replaced by hoses with air reservoirs at either end. Pressure exerted at the fingertip reservoirs would cause the stump reservoirs to inflate, extending the sensation of pressure to the stump (**Figure 2.8**).

Other examples emerged over the next hundred years. Conzelman et al. (1953) described a similar mechanism as Rosset's based on hydraulic pressure. Meek et al. (1989) extended the work of Rosset and Conzelman by using electrical circuitry to transmit force information to the residual stump via motor-driven "pushers." Patterson and Katz (1992) developed a similar system which instead used a vibrotactile or pressure cuff wrapped around the stump. After observing that amputees developed a phantom map of their lost hand on the stump surface, Antfolk et al. (2012) developed a closed pneumatic system to transfer tactile input from each fingertip to the corresponding stump location.

A more speculative form of modality-matched feedback derives from Kuiken's work in targeted muscle reinnervation (see **Section 2.3.2**), wherein redirected residual nerves transfer motor function to the chest muscles to enable EMG control of a myoelectric prosthesis. Kuiken et al. (2007a) reported that amputees who underwent this procedure also experienced a transfer of sensation, so that touching their chests evoked sensations in their missing limbs. Kuiken and his colleagues have speculated that sensors placed in a prosthetic hand could one day relay force and

temperature information to stimulators placed on the chest skin, providing modality-matched feedback.

2.5.2 Sensory-Substitution Feedback

Conzelman's 1953 patent also included an early example of sensory-substitution feedback, in which pressure applied to the prosthetic fingertip would close a circuit and activate a vibrating disk placed against the amputee's stump. The following years saw the development of numerous such "cutaneous displays" that transduced sensory information in vibrotactile stimuli delivered to residual stump skin. Kawamura (1971) affixed a mechanical vibrator inside the socket of a myoelectric prosthesis; the vibrational amplitude was proportional to the electrical output of a strain gauge located in the terminal device. Mann and Reimers (1970) mounted a pair of electromechanical stimulators on an amputee's stump, whose vibrations stroked the skin tangentially. Coordinated variation of the two amplitudes produced a sensation whose perceived location between the stimulators corresponded to the elbow angle.

Cutaneous displays based on electrical stimulation also emerged during this period. For example, Beeker et al. (1967) equipped a prosthetic hand with a piezoelectric crystal that emitted an electrical signal under deformation. Delivery of this unmodulated signal to the skin produced an electric shock. Prior et al. (1976) proposed the integration of strain gauges with myoelectric prostheses to guide graded electrical stimulation of skin corresponding to hand-opening and strength of grasp. Shannon (1979) reported the placement of strain gauges on the index finger of a myoelectric prosthesis. These transduced the patient's gripping force into electrical stimuli that were applied to the skin directly above the median nerve. The resulting feedback improved patient confidence in controlling the prosthesis.
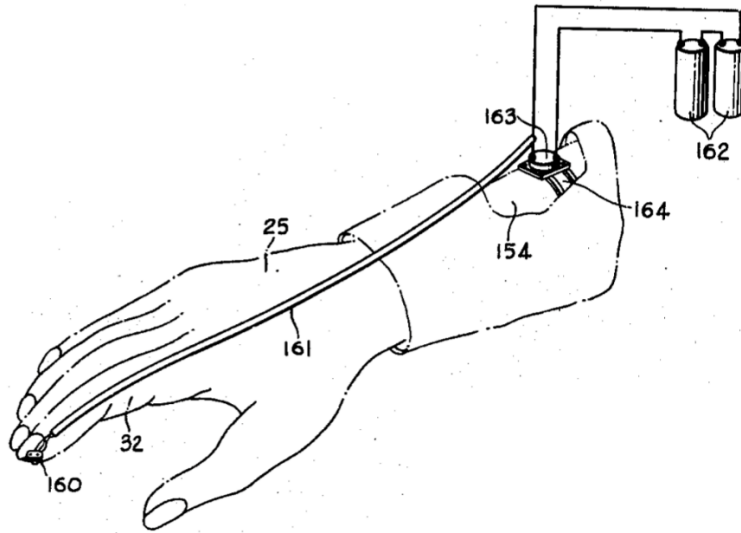
Figure 2.9: Sensory-substitution feedback as proposed by Conzelman et al. (1953). The application of pressure to the prosthetic fingertip closed a circuit, switching on a vibrator pressed against the limb stump.

In the past few decades, electrocutaneous displays have given way to implanted electrodes that electrically stimulate peripheral nerve tissue to induce sensory percepts in the phantom limb (Dhillon and Horch, 2005; Raspopovic et al., 2014; Tan et al., 2014; Davis et al., 2016; Charkhkar et al., 2018; Petrini et al., 2019). This final form of sensory-substitution feedback is the foundation of this dissertation. Before embarking on a more detailed description of the various interfaces that have been developed, I discuss in the sections that follow the structure and function of the peripheral nervous system and the physiological basis of electrical nerve stimulation.

2.6   The Pathway to Sensation

The nervous system is a network of tissues that transmits electrical signals between different parts of the body. In vertebrates, it has two parts: the central nervous system, which consists of the brain and spinal cord, and the peripheral nervous system, which transmits signals to and from the central nervous system and the rest of the body.

Peripheral nerves are cordlike bundles of fiber enclosed within a protective sheath of connective tissue. Nerve fibers called axons transmit motor commands from the spinal cord to the skeletal muscles, sensory information from various receptors back to the spinal cord, and signals to and from the internal organs and viscera. The human body has 43 pairs of peripheral nerves. 12 pairs are cranial nerves that emerge from the brain and play a role in the motor control of the face, head, neck, and shoulders, the transmission of sensory information from the sense organs, and parasympathetic control of blood pressure and heart rate. The other 31 pairs are spinal nerves that emanate from the spinal cord and innervate targets throughout the body.

The spinal nerves are labeled by their point of origin in the spinal column. Moving rostral to caudal, there are 8 cervical nerves (C_1-C_8), 12 thoracic nerves (T_1-T_{12}), 5 lumbar nerves (L_1-L_5), 5 sacral nerves (S_1-S_5), and 1 coccygeal nerve (Coc_1). Each spinal nerve is formed by the merger of ventral and dorsal roots that exit the spinal column via the intervertebral foramen. The ventral roots are populated by motor neurons, while the dorsal roots are populated by sensory neurons. The dermatome provides a useful visualization of how each spinal nerve maps to different parts of the body (**Figure 2.10**).

In **Section 2.4**, I discussed the multitude of mechanoreceptors that transduce tactile and proprioceptive stimuli into action potentials. I now describe how this sensory information makes its way to the central nervous system. Mechanoreceptors have associated axons whose ion permeabilities are altered by deformation to trigger action potentials. These "first-order" axons extend from their affiliated receptors to the spinal column and travel upwards ipsilaterally to the caudal medulla. Here, they synapse with "second-order" neurons that decussate and then rise contralaterally to the ventral posterior lateral nucleus (VPL) of the thalamus, where they then
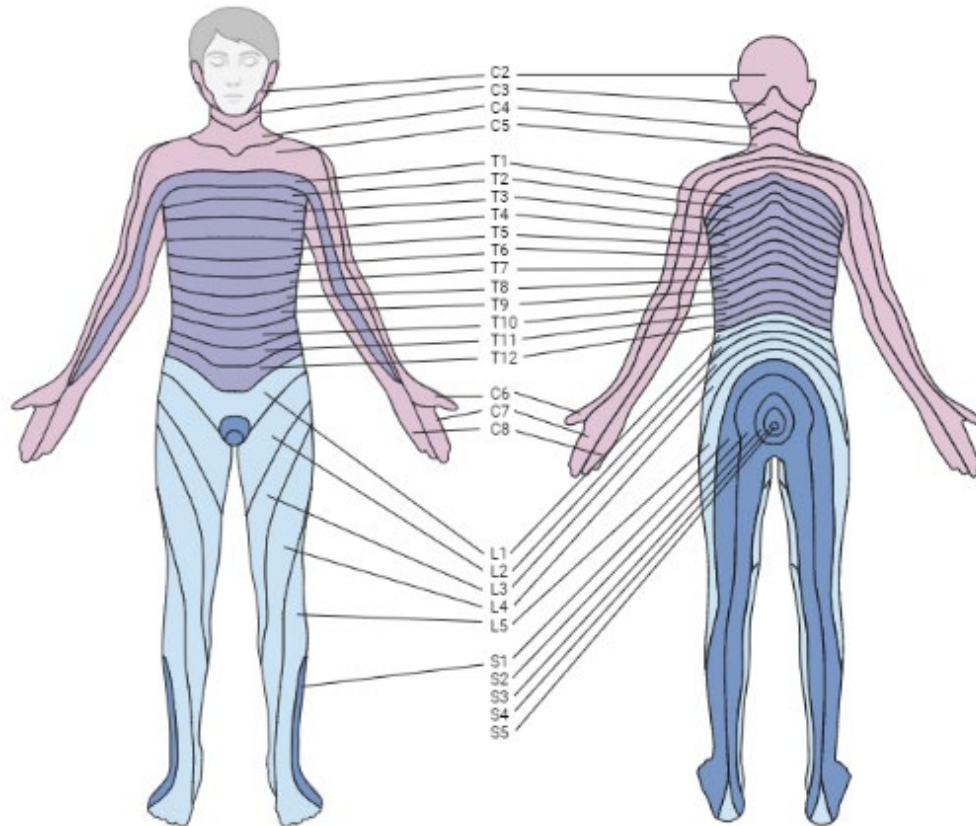
Figure 2.10: The human dermatome. Each pair of spinal nerves innervate a prescribed set of targets. This figure was created on BioRender.com.

synapse with "third-order" neurons whose axons project through the thermal capsule and on to the primary somatosensory cortex (SI), located on the postcentral gyrus of the brain.

2.7 Somatotopic Organization of Peripheral Nerves

Figure 2.11A depicts the cross-sectional organization of a peripheral nerve. Groups of axons form discrete bundles called fascicles that are surrounded by a layer of connective tissue called the perineurium. The axons pass through a delicate matrix of connective tissue called the endoneurium. The tunnels marked by their passage are called endoneurial tubes, and these can play an important role in nerve regeneration following injury. Outside the fascicles there lies a
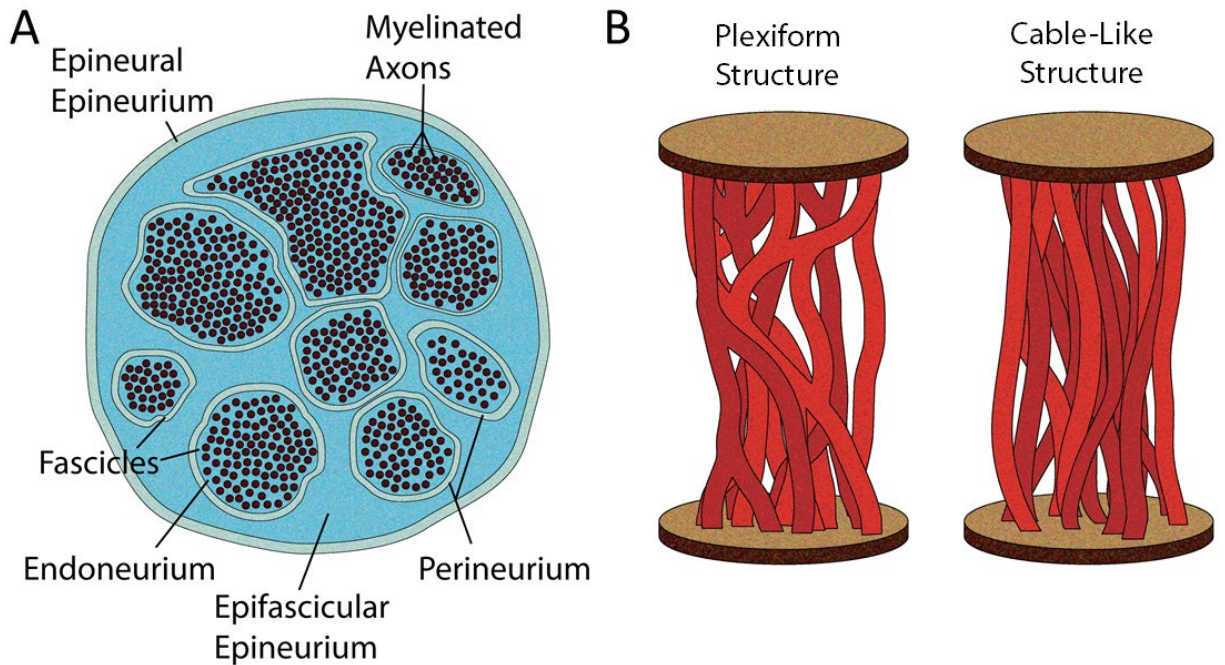
Figure 2.11: (A) Cross-sectional organization of a peripheral nerve. **(B)** Plexiform and cable-like structures of longitudinal fascicular organization. Adapted from Stewart (2003).

loose connective tissue called the epifascicular epineurium. This condenses at the perimeter to form a protective sheath called the epineural epineurium (Stewart, 2003).

Longitudinally, fascicular organization assumes a plexiform structure in proximal nerve segments, and a more cable-like structure in distal nerve segments (**Figure 2.11B**; Jabaley et al., 1980; Stewart, 2003). Despite this fascicular complexity, peripheral nerves follow a somatotopic organization as axons with shared innervation targets remain clustered together throughout the nerve's length (Brushart, 1991). This somatotopy plays an important role in electrode interface design, as discussed later in this chapter.

2.8 Peripheral Nerve Regeneration Following Injury

Seddon (1942) described three levels of severity for peripheral nerve injury. The mildest type of injury is neurapraxia (e.g., tourniquet paralysis), which is characterized by a temporary loss of

motor and sensory function followed by complete recovery. Axonotmesis is a more severe form of injury that involves severance of axons (e.g., crush injury) without disruption to the surrounding connective tissue. The most severe is neurotmesis (e.g., transection injury), in which axons are severed along with the complete disruption of the supporting nerve structure.

Damaged peripheral nerve axons possess a remarkable capacity for regeneration, although the extent of recovery depends on the severity of injury (Nguyen et al., 2002). After an axon is severed, distal segments that are separated from their cell bodies undergo Wallerian degeneration. Schwann cells remove the resulting debris and line the walls of the surrounding endoneurial tubes to create an environment conducive to axon growth. Proximal segments are drawn by the distal release of neurotrophic factors, eliciting directed regeneration. For axonotmesis injuries, the survival of the endoneurial tubes means that many regenerating axons will reach their original innervation targets, ensuring a high degree of functional recovery. In contrast, neurotmesis injuries' disruption of the endoneurial tubes greatly reduces the likelihood that regenerating axons emerging from the proximal stump will find their way back to their original distal targets. The resulting degradation of somatotopy leads to a poor restoration of sensory and motor function (Merzenich and Jenkins, 1993; Lago and Navarro, 2006).

2.9 Electrical Properties of the Nerve Cell

2.9.1 Structure of the Nerve Cell

A nerve cell has three main structural components: the soma, the axon, and dendrites. The soma (or cell body) houses the nucleus, mitochondria, endoplasmic reticulum, Golgi apparatus, and other organelles common to a wide range of cell types. The soma receives excitatory and inhibitory signals from other nerve cells via its short dendritic processes. The axon is an elongated projection
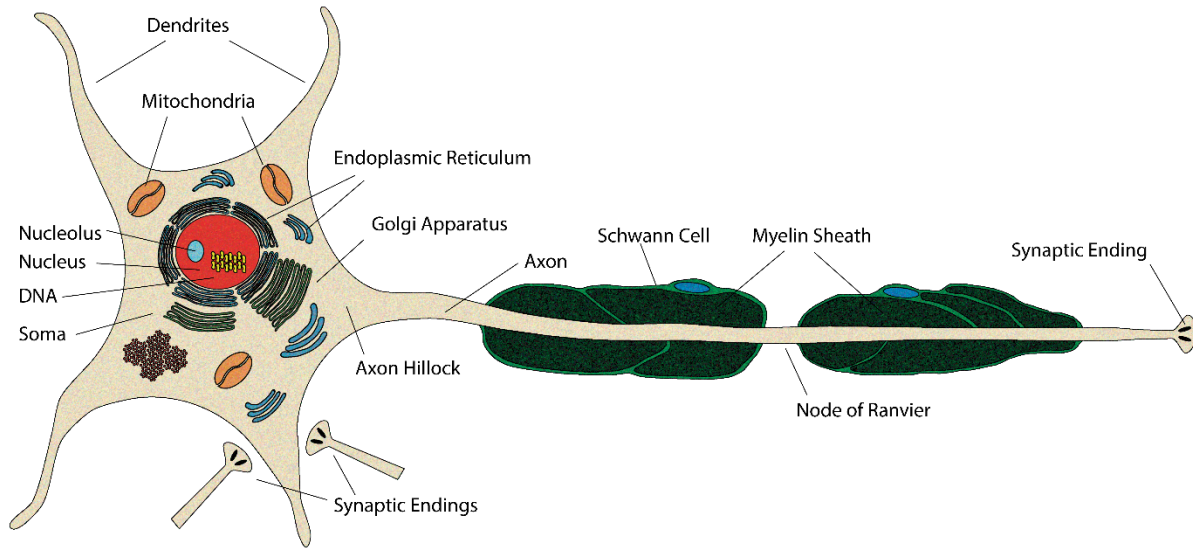
Figure 2.12: Structure of a myelinated nerve cell.

that transmits outgoing signals in the form of action potentials to other neurons. In mammals, axons may be surrounded by Schwann cells that form an insulating layer called the myelin sheath. This insulation is punctuated at regular intervals by gaps called the nodes of Ranvier. **Figure 2.12** depicts the structure of a myelinated nerve cell.

2.9.2 The Cell Membrane

The nerve cell membrane is a phospholipid bilayer that regulates the passage of ions and molecules between the intracellular and extracellular spaces. Certain ions (Na^+, K^+, Cl^-) exhibit a cross-membrane concentration gradient that is maintained by a network of active and passive ion pumps (**Figure 2.13**). These gradients give rise to a voltage difference across the membrane. Selective permeability of embedded ion-channels permits the use of the Nernst equation to calculate the voltage difference arising from a single ion species' concentration gradient. For the kth ion species,

$$E_k = -\frac{z_k F}{RT} \ln \frac{c_{i,k}}{c_{o,k}}, \tag{2.1}$$
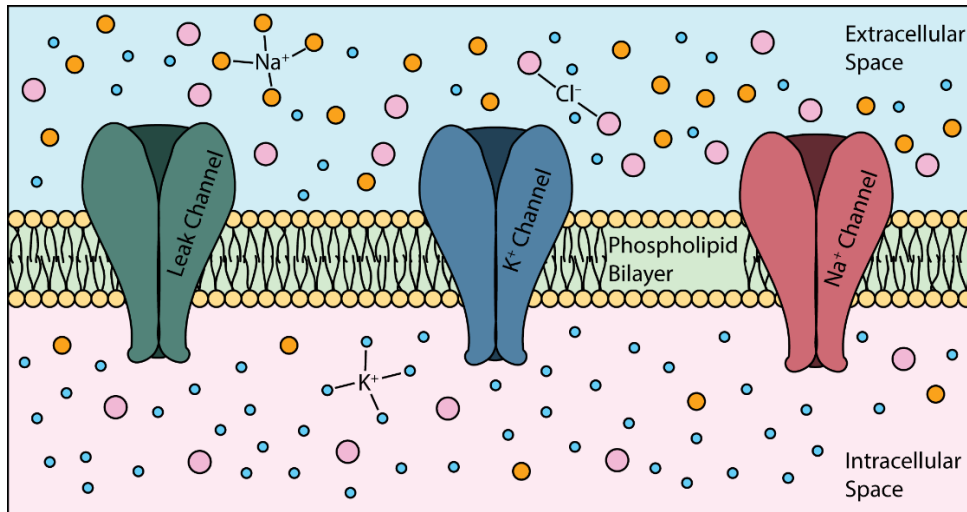
Figure 2.13: The nerve cell membrane regulates the passage of ions and molecules between the intracellular and extracellular spaces.
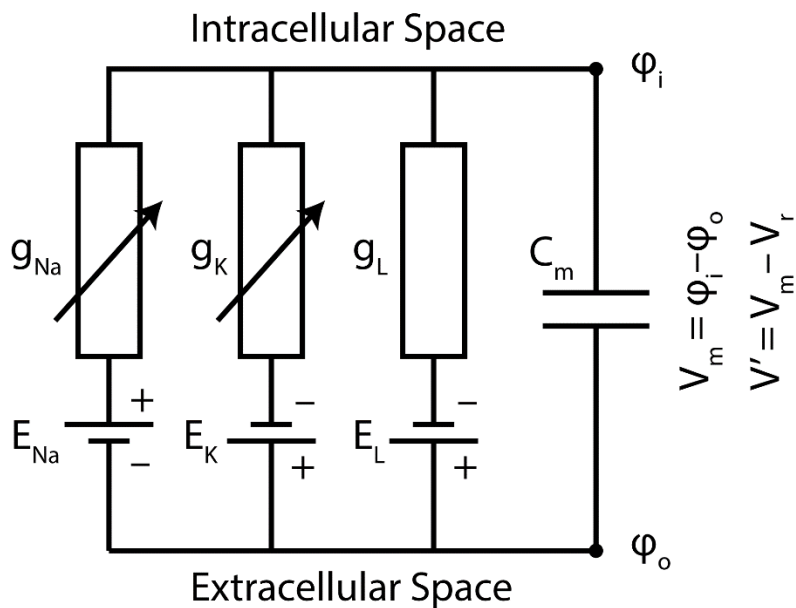
Figure 2.14: The parallel conductance model of an excitable cell membrane. The model assumes independent conductance channels for Na^+, K^+, and Cl^- ions. The batteries depict the Nernst potential of each ion. Note that Cl^- ions pass through "leak" channels – hence the subscript L.

where E_k is the Nernst potential, z_k is the ion's valency, F is Faraday's constant, R is the ideal gas constant, T is the temperature, and $c_{i,k}$ and $c_{o,k}$ are the intracellular and extracellular concentrations, respectively. When $V_m = E_k$, then the k-ions' electrostatic flux precisely balances their diffusive flux so that the net flux is zero.

The presence of multiple ion species in the intracellular and extracellular space means that no single value of V_m can equilibrate the flow of all ions simultaneously. Instead, V_m reaches a dynamic steady state called the resting potential, V_r, at which the net flow of current across the membrane is zero. By modeling the membrane as an electrical circuit (**Figure 2.14**) and applying Kirchhoff's current law, we obtain

$$V_r = \frac{g_{Na}E_{Na} + g_K E_K + g_L E_L}{g_{Na} + g_K + g_L}, \tag{2.2}$$

where g_{Na}, g_K, and g_L are ion-specific membrane conductances. Typical values for V_r lie in the -60 to -70 mV range.

2.9.3 Membrane Dynamics

Below a certain threshold (passive domain), a depolarizing current stimulus causes the cellular membrane to behave like an RC-circuit

$$V'(t) = (V_0' - I_s R_m)e^{-t/\tau} + I_s R_m, \tag{2.3}$$

where $V' = V_m - V_r$, R_m is the membrane resistance, C_m is the membrane capacitance, and $\tau = R_m C_m$ is a time constant (**Figure 2.15**). Stimulation above this threshold triggers an action potential (active domain). In the active circuit model of membrane potential, the current flowing across the membrane I_m has both capacitive and ionic components (**Figure 2.14**). Each ionic component I_k depends on the instantaneous membrane potential V_m, the ion's Nernst potential E_k,
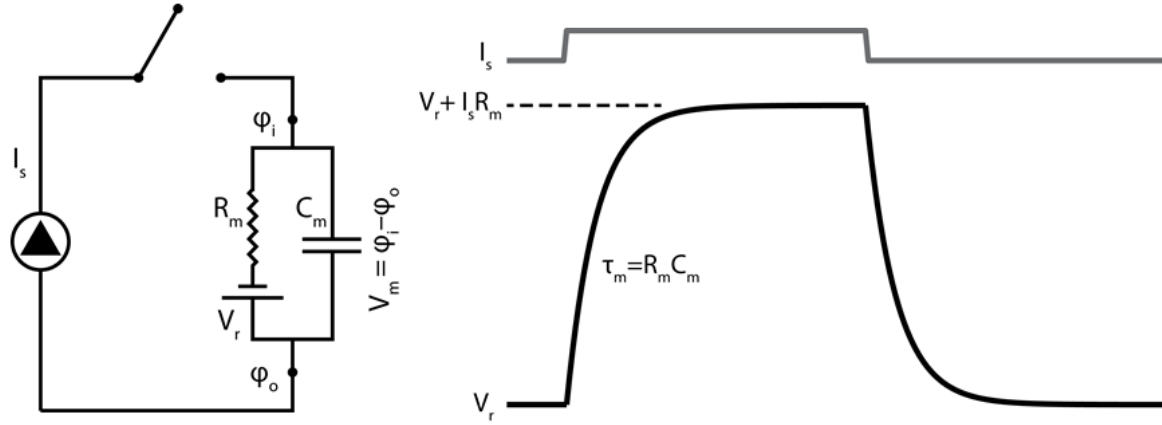
Figure 2.15: The cell membrane responds to subthreshold depolarization as a passive RC-circuit

and the instantaneous conductance g_k of k-specific ion-channels that reside in the membrane. Thus,

$$I_k = g_k(V_m, t)(V_m - E_k). \qquad (2.4)$$

The net membrane current is

$$I_m = C_m \frac{dV_m}{dt} + g_{Na}(V_m, t)(V_m - E_{Na}) + g_K(V_m, t)(V_m - E_K) + g_L(V_m - E_L), \qquad (2.5)$$

where the conductances g_{Na} and g_K are both time- and voltage-dependent and the leak ion conductance g_L is presumed constant.

2.9.4 The Hodgkin-Huxley Model

Hodgkin and Huxley's model of the squid giant axon provided the first comprehensive description of the complex membrane dynamics underlying the action potential (1952, 1952a, 1952b, 1952c, 1952d). Their experiments showed how the coordinated variation of ion-specific channel conductances are responsible for the action potential's characteristic shape (**Figure 2.16**).
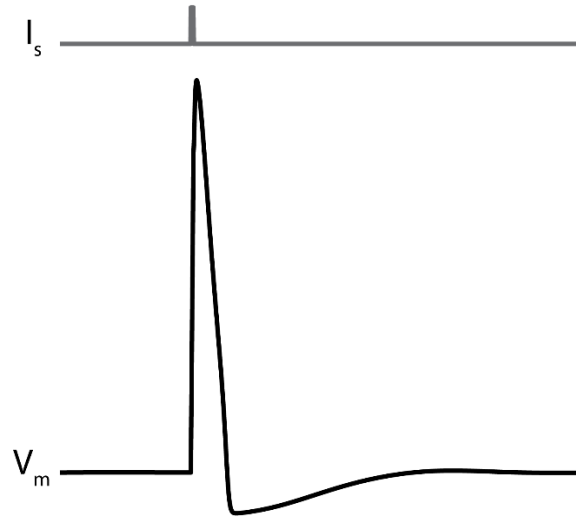
Figure 2.16: Suprathreshold depolarization of the cell membrane induces an action potential.

Using a space-clamped axon immersed in sea water, Hodgkin and Huxley observed that the application of a depolarizing voltage clamp V_c caused an initial capacitive spike followed by an inward current that reversed direction after some delay and asymptoted at some steady value. Repeating this measurement for an axon immersed in a solution with reduced sodium concentration, they concluded that the inward and outward currents were mediated by sodium and potassium ions, respectively. **Figure 2.17** depicts the response of a simulated axon membrane to a voltage clamp when immersed in normal and reduced sodium solutions.

Hodgkin and Huxley separated the sodium and potassium currents for different voltage clamps by making three assumptions. First, that the potassium currents for normal (I_K) and reduced (I_K') sodium solutions were equal, i.e., $I_K = I_K'$. Second, that the sodium currents I_{Na} and I_{Na}' shared the same time course even though they may have differed in amplitude and direction. Third, that $dI_k/dt = 0$ for the first one-third of the time taken by I_{Na} to reach its initial peak. By plotting I_m' against I_m and taking the initial slope, they obtained a proportionality factor k. The delayed onset

33
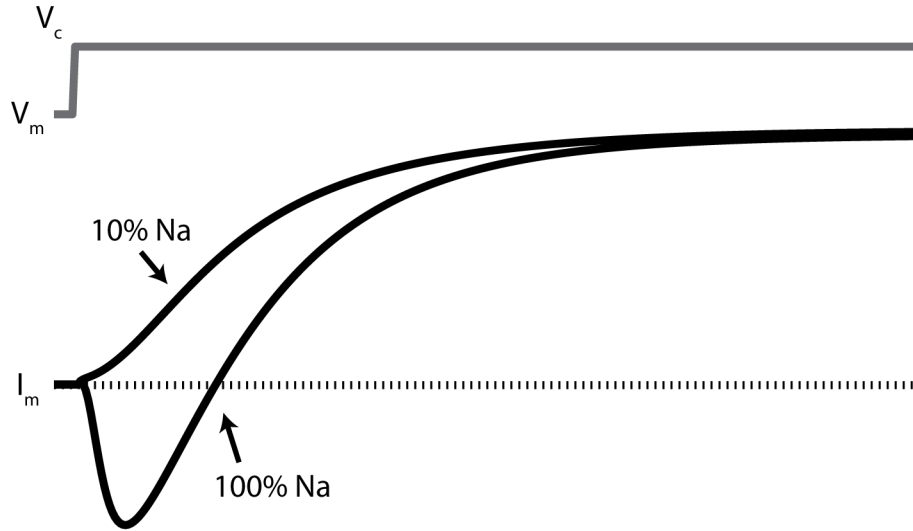
Figure 2.17: Current response of the squid giant axon to voltage clamp while immersed in sea water (100% Na) and a reduced sodium solution (10% Na).

of I_K implied that $I'_{Na} = kI_{Na}$. This enabled the calculation of I_{Na} and I_K in terms of the measured

membrane currents I_m and I'_m using the following algebraic manipulations:

$$
\begin{aligned}
I_m - I'_m &= (I_{Na} + I_K) - (I'_{Na} + I_K) \\
&= (I_{Na} - I'_{Na}) + (I_K - I'_K) \\
&= I_{Na} - I'_{Na} \\
&= I_{Na}(1 - k).
\end{aligned}
\tag{2.6}
$$

Therefore,

$$
I_{Na} = \frac{I_m - I'_m}{1 - k} \text{ and } I_K = \frac{I'_m - kI_m}{1 - k}.
\tag{2.7}
$$

The separated time courses of sodium and potassium currents (**Figure 2.18**) allowed the

calculation of corresponding ion-specific conductances as

$$
g_{Na} = \frac{I_{Na}}{V_c - E_{Na}} \text{ and } g_K = \frac{I_K}{V_c - E_K}.
\tag{2.8}
$$

34
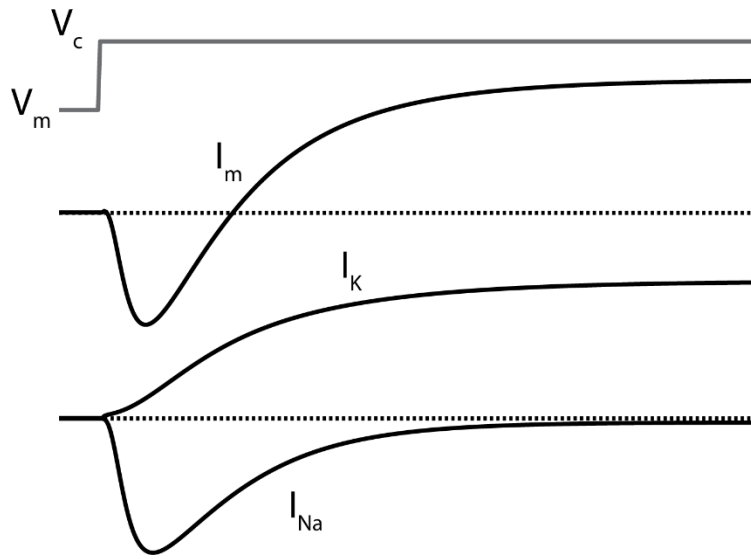
Figure 2.18: Time courses of membrane current I_m and separated sodium and potassium currents I_{Na} and I_K following a typical voltage clamp V_C. The sodium current is characterized by a sudden inward rush of sodium ions followed by a gradual return to zero. The potassium current's time course is somewhat sigmoidal and asymptotes to a steady value as the voltage clamp continues.
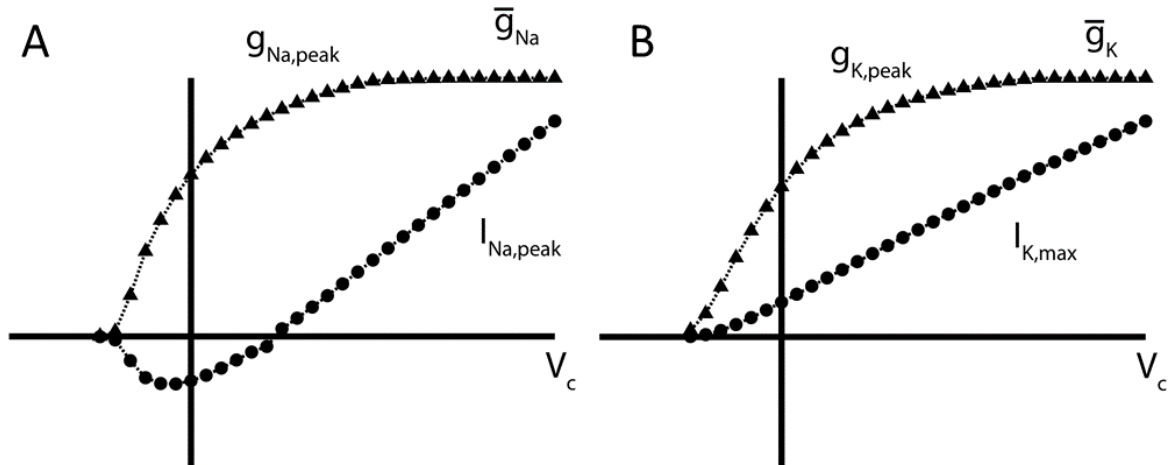
Figure 2.19: Peak currents for **(A)** sodium and **(B)** potassium ions, together with their corresponding peak conductances, for a range of voltage clamps. Conductances for both sodium and potassium asymptote to their maximum values $\bar{g}_{Na}$ and $\bar{g}_K$ for higher clamps.

For each voltage clamp V_c, Hodgkin and Huxley noted the peak sodium and potassium currents and used these to plot the corresponding ion-specific conductances. These asymptoted to their maximum values $\bar{g}_{Na}$ and $\bar{g}_K$ for higher values of V_c (**Figure 2.19**).

A careful examination of the data led Hodgkin and Huxley to conclude that the conductance of each potassium ion-channel was proportional to the fourth power of some variable n that obeyed first-order kinetics:

$$g_K(t) = \bar{g}_K[n(t)]^4 \tag{2.9}$$

$$\text{and} \quad \frac{dn}{dt} = \alpha_n(V')(1-n) - \beta_n(V')n. \tag{2.10}$$

Note that the rate constants α_n and β_n depend on the membrane's deviation from the resting potential, $V' = V_m - V_r = V_c - V_r$.

Solving the differential equation yields

$$n(V_c, t) = n_\infty(V_c) + \big(n_0 - n_\infty(V_c)\big)e^{-t/\tau_n(V_c)}, \tag{2.11}$$

$$\text{where } n_\infty(V_c) = \alpha_n(\alpha_n + \beta_n)^{-1} \text{ and } \tau_n(V_c) = (\alpha_n + \beta_n)^{-1}. \tag{2.12}$$

The above equation has the correct form to fit the experimentally derived potassium conductance $g_K(t)$. The optimal fit for each voltage clamp can be obtained by adjusting the parameters n_∞ and τ_n, allowing the calculation of the rate constants as

$$\alpha_n(V') = \frac{n_\infty(V_c)}{\tau_n(V_c)} \text{ and } \beta_n(V') = \frac{1 - n_\infty(V_c)}{\tau_n(V_c)}. \tag{2.13}$$

After calculating α_n and β_n for various voltage clamp values, Hodgkin and Huxley used curve fitting to obtain

$$\alpha_n(V') = \frac{0.01(10 - V')}{\exp\left(\frac{10 - V'}{10}\right) - 1} \text{ and } \beta_n(V') = 0.125 \exp\left(\frac{-V'}{80}\right). \tag{2.14}$$

To characterize the rise and fall of the sodium conductance's time course under voltage clamp, Hodgkin and Huxley proposed the interaction of two competing processes – an activating process mediated by the third power of some variable m, and an inactivating process mediated by the first power of some variable h. Both variables were assumed to obey first-order kinetics. Thus,

$$g_{Na}(t) = \bar{g}_{Na}[m(t)^3]h(t), \tag{2.15}$$

$$\frac{dm}{dt} = \alpha_m(1 - m) - \beta_m m, \tag{2.16}$$

$$\text{and } \frac{dh}{dt} = \alpha_h(1 - h) - \beta_h h. \tag{2.17}$$

Solving these differential equations yielded the following expressions:

$$m(V_c, t) = m_\infty(V_c) + \left(m_0 - m_\infty(V_c)\right)e^{-t/\tau_m(V_c)}, \tag{2.18}$$

$$\text{and } h(V_c, t) = h_\infty(V_c) + \left(h_0 - h_\infty(V_c)\right)e^{-t/\tau_h(V_c)}. \tag{2.19}$$

Hodgkin and Huxley made two simplifying assumptions – first, that sodium conductance would drop to zero after infinite time, i.e., $h_\infty(V_c) = 0$, and second, that sodium conductance prior to depolarization was zero, i.e., $m_0 = 0$. This gave the following equation for $g_{Na}(t)$:

$$g_{Na}(t) = \bar{g}_{Na}[m_\infty(V_c)]^3 \, h_0\left(1 - e^{-t/\tau_m(V_c)}\right)^3 e^{-t/\tau_h}. \tag{2.20}$$

By fitting $m_\infty(V_c)$, $\tau_m(V_c)$, and $\tau_h(V_c)$ to the observed time course of $g_{Na}(t)$ for different voltage clamps, plots of $\alpha_m(V')$, $\beta_m(V')$, $\alpha_h(V')$, and $\beta_h(V')$ were obtained. Regression analysis yielded the following formulas:

$$\alpha_m(V') = \frac{0.1(25 - V')}{\exp\left(\frac{25 - V'}{10}\right)} \text{ and } \beta_m(V') = 4\exp\left(-\frac{V'}{18}\right) \qquad (2.21)$$

$$\text{and } \alpha_h(V') = 0.07\exp\left(-\frac{V'}{20}\right) \text{ and } \beta_h(V') = \left\{\exp\left[\frac{(30 - V')}{10}\right] + 1\right\}^{-1}. \qquad (2.22)$$

The equations presented thus far provide a mathematical description of the membrane dynamics of a space-clamped, unmyelinated squid giant axon. What is remarkable is that Hodgkin and Huxley achieved this feat without having direct knowledge of the actual mechanisms underlying the membrane's variable permeability to sodium and potassium ions. Today, we know that this variability arises due to voltage sensitive proteins associated with each ion channel. Potassium channels have four activating protein molecules that open with membrane depolarization. Sodium channels have three activating molecules and one inactivating molecule that open and close, respectively, with membrane depolarization. The variables n, m, and h may each be reinterpreted as the probability of their corresponding protein molecules being open. Correspondingly, the probability that a potassium channel is open to the passage of ions is the joint probability n^4. Similarly, the probability that a sodium channel is open is m^3h.

Figure 2.20 shows how the time courses of n, m, and h align with the action potential. The rapid opening of m-gates triggers an inrush of sodium ions and a sharp depolarization of the membrane potential. The delayed opening of the n-gates allows potassium ions to flow in the opposite direction and tempers the depolarization wrought by increased sodium conductance. The slow
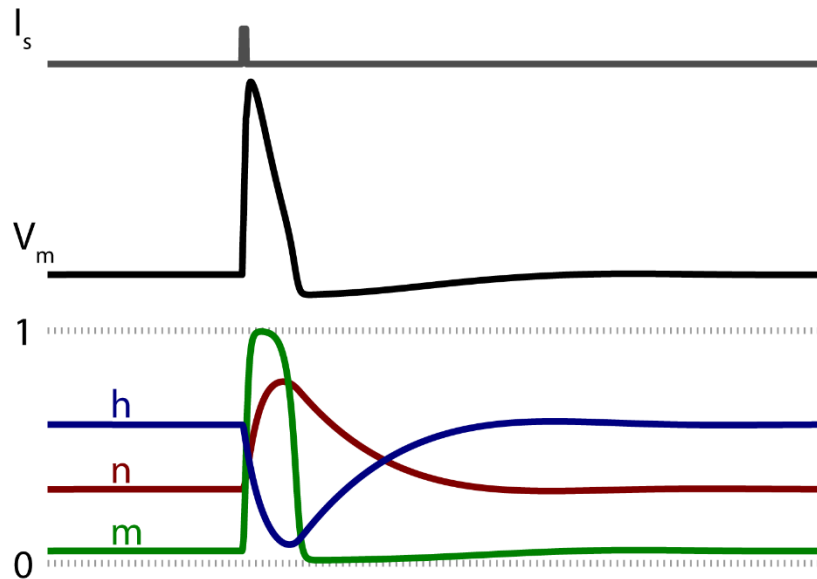
Figure 2.20: Time course of an action potential together with the corresponding time courses of n, m, and h gates.

closing of the h-gates shuts off the sodium channels, allowing the potassium conductance to dominate and repolarize the membrane, terminating the action potential.

Extending the Model to Mammals

The Hodgkin-Huxley model was developed by suspending the unmyelinated squid giant axon in a seawater bath at 6˚C. In later years, new models emerged that were tailored to the behavior of myelinated mammalian axons at higher temperatures. Chiu et al. (1979) published a quantitative description of membrane currents in myelinated rabbit nerve at 14˚C. Notably, their model was predicated on an absence of potassium current at the nodes of Ranvier. Although the transient inward sodium current still mediated the action potential's rapid depolarization phase, the ensuing repolarization depended wholly on the leak current. Sweeney et al. (1987) built upon these results to describe the transmission of action potentials through myelinated axons at 37˚C, creating the so-called "CRRSS" model.
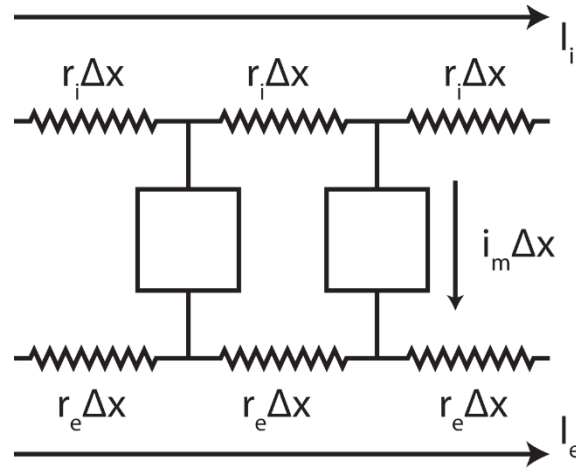
Figure 2.21: The core conductance model divides an axon into segments of length Δx.

2.9.5 The Core Conductance Model

The Hodgkin-Huxley model was developed with an axon whose membrane potential was kept uniform along its length using a space-clamp. In the absence of a space-clamp, an action potential induced by a localized membrane depolarization will propagate down the axon's length – this is the basis for signal transmission within a neuron.

The core conductance model regards the axon as a cable comprised of repeated segments of length Δx (**Figure 2.21**). Assume axial symmetry. Let there be clearly defined intracellular and extracellular spaces that are separated by the axon's membrane. Let the axon's diameter be a. Let r_i, I_i, and ϕ_i be the intracellular axial resistance [Ω/cm], current, and potential measured with respect to a distant ground. Let r_e, I_e, and ϕ_e be the corresponding quantities for the extracellular space. Let $R_i = r_i \cdot \pi a^2$ be the specific resistivity of the intracellular space. Let r_m be the membrane (leakage) resistance times length [$\Omega \cdot$ cm] and c_m the membrane capacitance per unit length [μF/cm]. Let i_m be the membrane current per unit length of axon and let $I_m = i_m/2\pi a$ be the membrane current per unit area. Let i_p be an applied extracellular current per unit length. It can be shown that

$$\frac{\partial^2 V_m}{\partial x^2} = (r_i + r_e)i_m + r_e i_p. \tag{2.23}$$

Further, since $r_e \approx 0$ and $i_p = 0$ in the absence of a stimulating current, the above equation may be further reduced to

$$I_m = \frac{a}{2R_i}\frac{\partial^2 V_m}{\partial x^2}. \tag{2.24}$$

Thus, the membrane current is directly proportional to the membrane potential's 2nd spatial derivative in the axial direction. Recall that the Hodgkin-Huxley formulation expresses the same membrane current as the sum of capacitive and ionic currents:

$$I_m = C_m\frac{\partial V_m}{dt} + \bar{g}_{Na}m^3h(V_m - E_{Na}) + \bar{g}_K n^4(V_m - E_K) + \bar{g}_L(V_m - E_L). \tag{2.25}$$

Equating the two expressions for I_m yields

$$\frac{\partial V_m}{\partial t} = \frac{a}{2R_i C_m}\frac{\partial^2 V_m}{\partial x^2} - \frac{1}{C_m}\sum \text{ionic currents}. \tag{2.26}$$

The above equation provides a basis for the computational simulation of a propagating action potential.

2.9.6 Local Circuit Currents

An axon that has been excited at a particular site to the point of triggering an action potential experiences an inrush of sodium ions causing a localized buildup of positive charge in the intracellular space. This creates a potential gradient with respect to adjacent axon segments in a different phase of excitation, resulting in the flow of charge carriers in closed loop trajectories called local circuit currents. The passage of these currents across the membrane at downstream coordinates causes the membrane at these coordinates to depolarize. Continued depolarization at these downstream coordinates eventually reaches a threshold at which point the membrane's
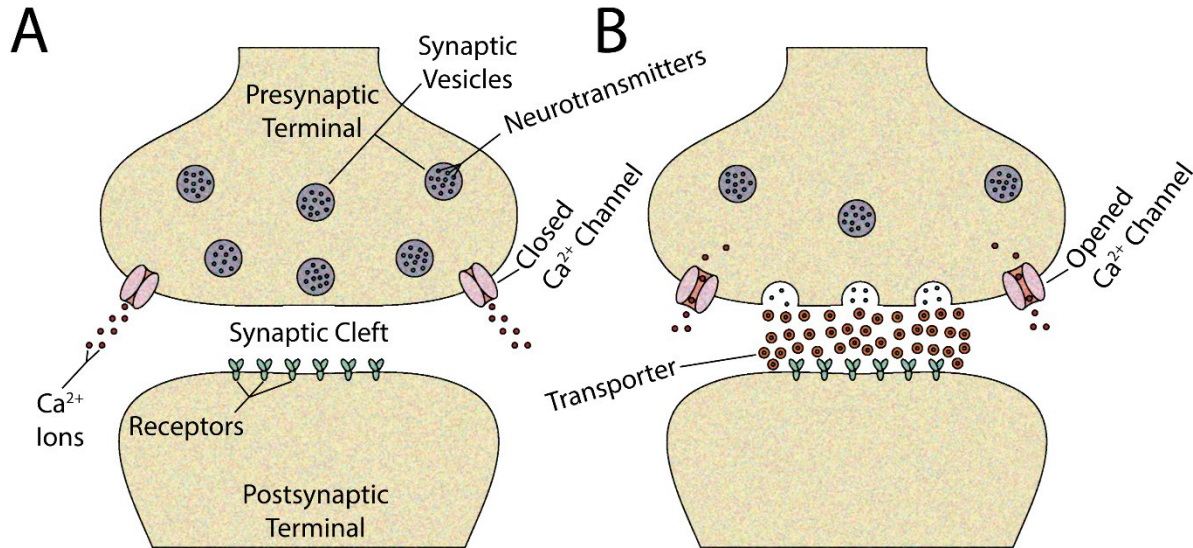
Figure 2.22: Mechanism of synaptic transmission.

permeability to sodium ions matches that at the original site. In this manner, the action potential propagates down the length of the axon.

For a myelinated axon, the effective insulation provided by the myelin sheath ensures that the passage of local circuit currents into the extracellular space (and accompanying downstream membrane depolarization) is restricted to the nodes of Ranvier. Moreover, the fact that virtually no current is lost in the internodal space means that downstream excitation of axon segments is more efficient than with an unmyelinated axon. For this reason, action potentials propagate far more quickly through myelinated axons than unmyelinated axons of the same diameter.

2.9.7 Synaptic Transmission

Neurons communicate with each other or with muscle cells through unidirectional signaling structures called synapses. A synapse has three parts: the presynaptic terminal, located at the end of the signaling neuron's axon; the postsynaptic terminal, associated with a dendrite or the soma of the receiving neuron; and the synaptic cleft, which separates the two terminals (**Figure 2.22A**).

The arrival of an action potential at the presynaptic terminal causes an influx of calcium ions, triggering the release of excitatory or inhibitory neurotransmitters into the synaptic cleft (**Figure 2.22B**). The uptake of these neurotransmitters at the postsynaptic terminal depolarizes or hyperpolarizes the receiving neuron's membrane potential (depending on the neurotransmitter). This effect is additive, as sufficient depolarization corresponding to high levels of synaptic activity triggers an action potential in the receiving neuron. Thus, whereas the transmission of information within a neuron is electrical, the transmission of information between neurons is chemical.

2.10 Electrode Interfaces to the Peripheral Nervous System

An electric current flowing in the vicinity of a peripheral nerve axon depolarizes its membrane and induces a train of action potentials. Stimulated efferent axons deliver action potentials to neuromuscular junctions and activate associated motor units – this is the basis for functional electrical stimulation (FES), a therapeutic intervention that affords motor control to individuals paralyzed by brain or spinal cord injuries (MacEwan et al., 2016). In contrast, action potentials induced in an amputee's afferent axons travel to the brain and elicit sensations perceived to originate in the phantom limb (Dhillon et al., 2004). Thus, electrical stimulation of an amputee's residual nerve stump can provide a foundation for closed-loop prosthetic control. The development of electrodes that interface with peripheral nerve and transduce the output of embedded prosthetic sensors into felt sensations constitutes an active area of neuroprosthetics research today.

For an electrode to be a viable sensory feedback interface, it must elicit sensations identifiable with distinct locations in the phantom limb. The inherent somatotopy of peripheral nerve axons is favorable to electrodes that can selectively recruit discrete axon clusters with wide nerve coverage. Such selectivity derives in part from the proximity of the electrode's metallized leads to the
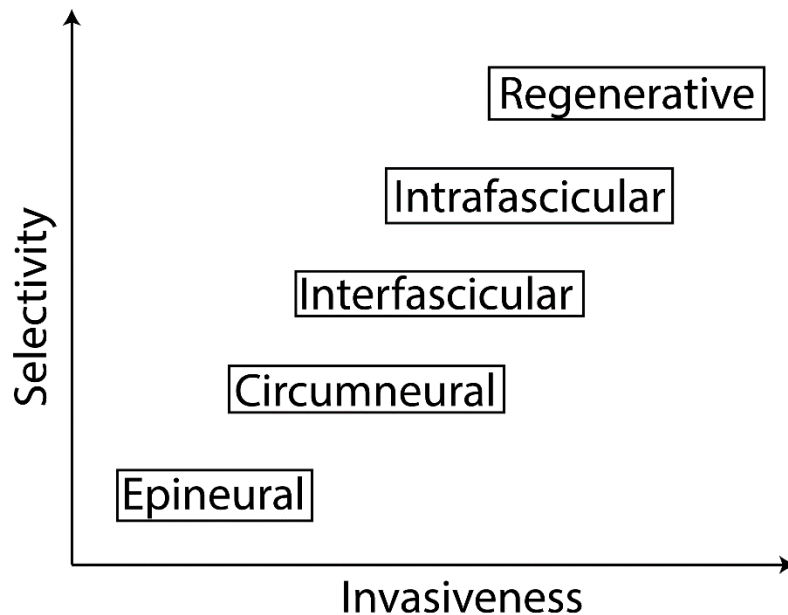
Figure 2.23: Peripheral nerve interfaces' selectivity rises with invasiveness (adapted from Navarro et al., 2005).

targeted axons, since nearby axons require lower activating currents than axons that are further away. Thus, there is a close relationship between an electrode's invasiveness and its selectivity, as illustrated in **Figure 2.23**.

2.10.1 Epineural and Circumneural Electrodes

Least invasive of all are the epineural electrodes (**Figure 2.24A**), which are affixed directly to the nerve's surface by suture (Navarro et al., 2005). Next are the circumneural electrodes (**Figure 2.24B**), which wrap around the nerve so that leads lining the inner surface lie adjacent to the nerve's periphery. The extraneural cuff electrode (ECE) is a silastic tube or spiral (Loeb and Peck, 1996) that provides selective control of superficial axons but whose control over more interior axons is limited (Veraart et al., 1993; Choi et al., 2001). The flat-interface nerve electrode (FINE) overcomes this limitation by deforming the nerve to bring interior axons closer to the periphery and within the control of its surface leads (**Figure 2.24C**; Tyler and Durand, 2002).

44
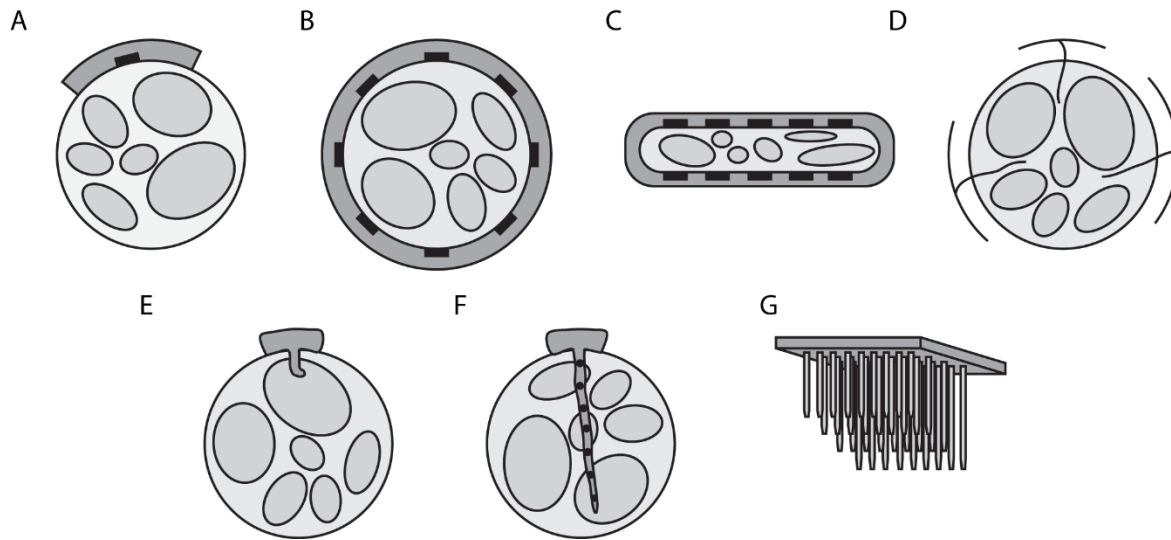
Figure 2.24: (A) Epineural electrode. **(B)** Extraneural cuff electrode (ECE). **(C)** Flat interface nerve electrode (FINE). **(D)** Slowly penetrating interfascicular cuff electrode (SPINE). **(E)** Longitudinal intrafascicular electrode (LIFE). **(F)** Transverse intrafascicular multichannel electrode (TIME). **(G)** Utah slanted electrode array (USEA).

2.10.2 Interfascicular Electrodes

The next level of invasiveness is occupied by electrodes whose leads penetrate the nerve's epineural sheath and take up residence in the epifascicular epineurium, i.e., interfascicular electrodes. The most prominent example is the slowly penetrating interfascicular electrode (**Figure 2.24D**; SPINE). This is a silicone rubber tube with blunt "elements" extending radially into the lumen. The tube's end is frayed to form four "beams." When splayed out, the material's inherent elasticity causes the beams to return to their original position. Thus, following implantation, the beams exert a small amount of force upon the nerve via the radial elements, which slowly penetrate the epineurium without further surgical intervention (Tyler and Durand, 1997).

2.10.3 Intrafascicular Electrodes

Intrafascicular electrodes are those that break through both the epineural sheath and the perineurium to place their leads inside the fascicular space. There are two types. The longitudinal intrafascicular electrode (**Figure 2.24E;** LIFE) is a thin, electrically insulated wire filament that

enters a fascicle axially so that its exposed tip interfaces that fascicle alone (Malagodi et al., 1989; Lefurge et al., 1991; Nannini and Horch, 1991; Dhillon et al., 2004). This design has proved effective for both stimulation and recording applications, but it is impractical for the interfacing of multiple fascicles as this requires the separate insertion of multiple filaments. The transverse intrafascicular multichannel electrode (**Figure 2.24F**; TIME) overcomes this barrier by penetrating the nerve perpendicularly so that multiple leads along its length may reside within separate fascicles (Boretius et al., 2010; Raspopovic et al., 2014).

Penetrative Microelectrode Arrays
Penetrative microelectrode arrays constitute a highly invasive electrode class comprising 1- or 2-dimensional grids of metallic tines that each house one or more channels for stimulating or recording neural activity. In contrast to the flexibility afforded by intrafascicular electrodes' filaments, a microelectrode array's tines can be rigid and therefore mechanically mismatched with nerve tissue. This renders them prone to being damaged or causing damage to surrounding tissue following implantation, especially when they are implanted in high-movement regions such as a limb. The most relevant example is the Utah slanted electrode array (**Figure 2.24G**; USEA), a 2-dimensional grid whose tines penetrate the nerve to varying depths so that axon clusters from throughout the nerve fall under the ambit of a nearby tine (Branner et al., 2004; Davis et al., 2016).

2.10.4 Regenerative Electrodes
Perhaps the most invasive of all are the regenerative electrodes (RE). The archetypal RE (or "sieve" electrode) is a flat, perforated disk with affixed conduits on either side. It is implanted between the transected stumps of a peripheral nerve. Regenerating axons from the proximal stump pass through the disk's perforations (or "transit zones") to robustly integrate the electrode into the

nerve's structure. Leads interspersed among the transit zones enable the recording or stimulation of nearby axons.

Numerous iterations of this design have emerged in the last 50 years. Among the earliest recorded was Frishkoff, Goldstein, and Hambrecht's abortive attempt (1965-1967) to record the activity of the cat sciatic nerve using a 1-cm diameter, 250-μm thick ceramic button perforated by 25-μm transit zones equipped with recording electrodes (reported by Kovacs et al., 1992). Marks (1969) reported axon growth through the pores of a Teflon wafer implanted in the sciatic nerve of a bullfrog. Mannard et al. (1974) poured epoxy over silver wires, milled the epoxy into a disk-shape, and drilled 100-μm transit zones through each wire to create electrified channels for recording the activity of bullfrog sciatic axons.

Edell (1986) created a silicon microgrid of "slotted" transit zones and performed the first recording of regenerated mammalian nerve activity using the rat tibial nerve. Subsequent studies built upon this success, building REs capable of both stimulating and recording regenerated axons in rat peroneal nerve (Kovacs et al., 1992), rat glossopharyngeal nerve (Akin et al., 1994), rat sciatic nerve (Navarro et al., 1996), and rabbit sciatic nerve (Dario et al., 1998).

The intrinsic rigidity of silicon makes it a poor choice of substrate for building a long-term peripheral nerve interface. Bearing this in mind, Stieglitz et al. (1997) reported the fabrication of a multichannel RE from polyimide, a lightweight, flexible substrate noted for its thermal, mechanical, and chemical stability. Navarro et al. (1998) subsequently demonstrated the recording and stimulation of rat sciatic nerve axons regenerated through a polyimide sieve.
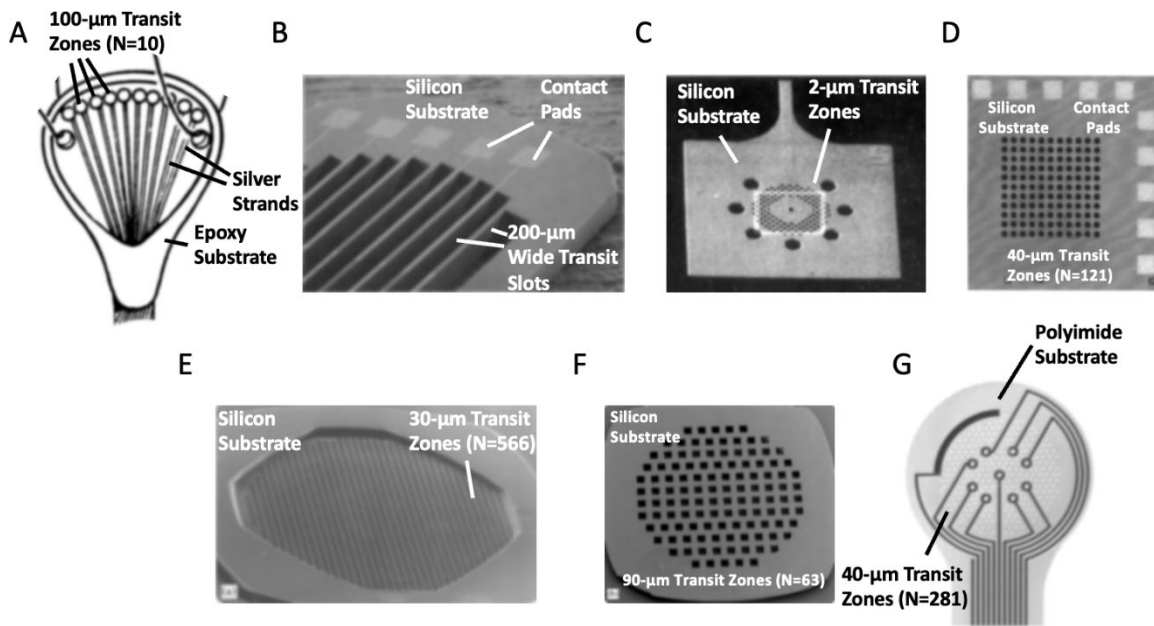
Figure 2.25: (A) Early RE design (adapted from Mannard et al., 1974). **(B-F)** Various silicon REs (adapted from Edell, 1986; Akin et al., 1994; Navarro et al., 1996; Wallman et al., 2001). **(G)** Polyimide RE (adapted from Negredo et al., 2004).

The advent of microfabrication technologies for silicon and polyimide brought with it the prospect of creating high-transparency REs with transit zones small enough to interface axons at or near the individual level. The commonly held rationale was that this would reduce the computational complexity otherwise required to separate the recorded activity of multiple axons, and also simplify the stimulation paradigm required for selective axon recruitment. Although axon regeneration has been reported through transit zones as small as 2 µm (Bradley et al., 1992), such small diameters are associated with constrictive axonopathy and obstruct functional recovery to the level required for sensorimotor restoration (Rosen et al., 1990; Navarro et al., 1996). An ideal diameter ranging from 40 to 65 µm has been suggested previously (Navarro et al., 1996), and efforts to increase the number of transiting axons – and hence functional recovery – have focused on increasing the number of transit zones (Wallman et al., 2001; Lago et al., 2007). However, the notion that the number of myelinated fibers distal to the RE eventually reach control values
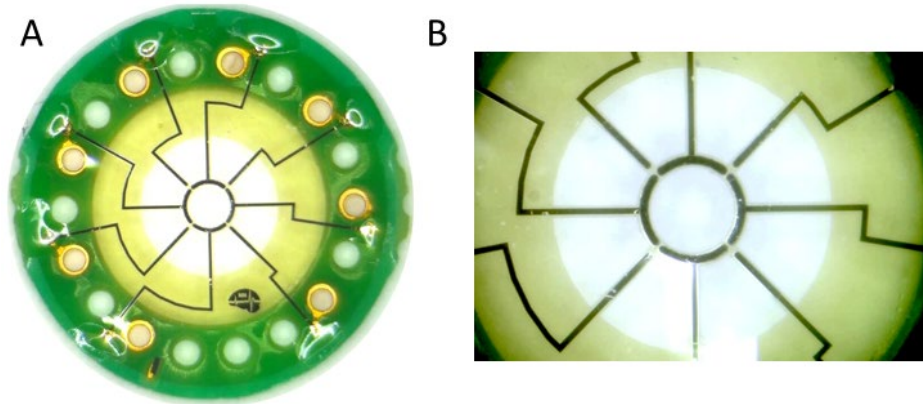
Figure 2.26: (A) The macro-sieve electrode. **(B)** Close-up of the active region.

(Ceballos et al., 2002) is likely more reflective of the branching inherent to axon regeneration than the nominal increase in axons traversing the RE's plane of activation (Negredo et al., 2004).

The Macro-Sieve Electrode

The macro-sieve electrode (MSE) is a highly transparent RE-variant composed of three concentric rings: an inner active region, a middle polyimide ring, and an outer PCB ring (**Figure 2.26A**). The MSE maximizes functional recovery with the active region's nine large transit zones whose combined area exceeds 2 mm^2 (**Figure 2.26B**). The middle polyimide ring contains embedded traces that deliver current stimuli from the PCB ring's solderable through-holes to the active region.

Within the active region, the transit zones' boundaries are defined by a central hub and eight radiating spokes. The central hub holds four "core" Pt-Ir leads with a curved geometry. Each of these core leads is 32,000 μm^2 in area. An additional four "peripheral" leads are located on alternating radial spokes. These have a straight geometry and are each 22,500 μm^2 in area.

Zellmer (2014) has shown that the MSE can selectively recruit any axon cluster in the nerve's cross-section by the coordinated application of cathodic and anodic currents (i.e., current steering;
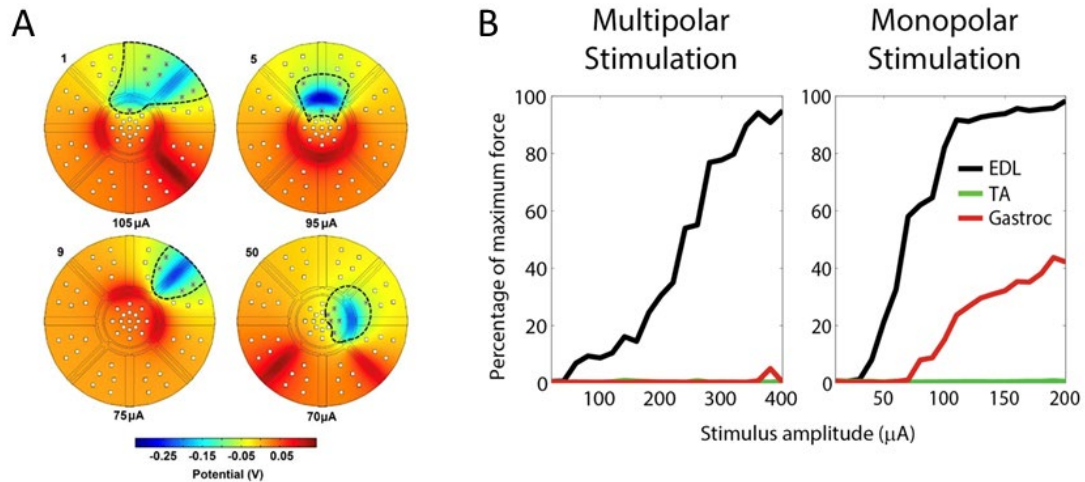
Figure 2.27: (A) Multipolar stimulation profiles (i.e., current steering) can selectively recruit discrete axon clusters throughout the nerve (reproduced from Zellmer, 2014). Activation by cathodic potentials (blue) is countered by hyperpolarizing anodic potentials (red), restricting axon recruitment to the encircled regions. **(B)** *In vivo* demonstration of selective muscle activation by multipolar stimulation (reproduced from Zellmer, 2014). EDL – extensor digitorum longus muscle. TA – tibialis anterior muscle. Gastroc – gastrocnemius muscle.

Figure 2.27). Zellmer et al. (2018) further suggest that recruitment thresholds for regenerated axons are not inherently higher or lower than those of undisrupted axons, but depend on their distance from the stimulating lead and the manner of stimulation. Accordingly, they predict that regenerated axons located near the stimulating lead should have lower thresholds than undisrupted axons and that those further away should have higher thresholds. This has important implications for selectivity, as it suggests that recruited clusters of regenerated axons may be even more confined in their extent than corresponding clusters of undisrupted axons would be under identical stimulus conditions. The prospect of delivering a high degree of selective control with just eight leads makes the MSE's candidacy as a potential sensory feedback interface particularly attractive. A previous *in vivo* study by MacEwan et al. (2016) tested the MSE's ability to recruit distal musculature selectively. A similar *in vivo* assessment of the MSE's sensory capabilities is required.

2.11 Assessing an Electrode's Sensory Performance

To date, the assessment of an electrode's sensory performance has followed a somewhat predictable pattern. First, a small number of human subjects undergo implantation of one or more electrodes on a short- or long-term basis. Next, the implanted subjects undergo regular testing sessions in which they report the location, quality, and stability of elicited percepts in response to various stimulus configurations. There is a particular focus on the effect of modulating current amplitude, pulse width, and frequency. Finally, the study may conclude with a demonstration of closed-loop control based on feedback from embedded prosthetic sensors linked with the implanted electrodes.

Notable findings from such assessments may be generalized across multiple electrode types. First, stimulation by channels targeting different fascicles induces percepts that map to known innervation patterns for undisrupted nerves, underscoring the preeminence of axon somatotopy (Dhillon et al., 2004; Dhillon and Horch, 2005; Raspopovic et al., 2014; Tan et al., 2014, 2015; Davis et al., 2016). Second, elicited sensations can be stable longitudinally, but the degree of stability likely depends on the electrode type (Tan et al., 2014, 2015; Davis et al., 2016). Third, the quality of elicited sensations depends strongly on the particular waveform used to stimulate the nerve. For example, Tan et al. (2014, 2015) observed that biphasic, rectangular pulse trains induced electricity-like tingling sensations (i.e., paresthesia) that felt far from natural, and that this effect could be mitigated through pulse-width modulation. Most intriguingly, different modulating frequencies and pulse widths' upper- and lower-bounds were found to correspond to different modes of sensation (tapping, constant pressure, vibration, and rubbing on a textured surface). Davis et al. (2016) made similar observations.

Such testing has the decided advantage that humans are equipped with the power of speech and understanding and can therefore relate their sensory experiences to researchers directly with minimal training required. However, this approach precludes the testing of unproven electrodes in the early stages of development, particularly those such as the MSE whose implantation procedure requires nerve transection and is therefore irreversible. Although animals cannot directly relate their sensory experience (especially with regards to the quality of sensation), a well-designed animal model can yield valuable insights into an electrode's performance as a sensory feedback interface. These insights can inform the design of future iterations and provide eventual justification for clinical trials.

Rodent behavioral models are useful platforms for the systematic study of sensation. Such models have previously been applied to the characterization of the rodent vibrissal system (e.g., Stuttgen et al., 2006; Adibi and Arabzadeh, 2011; Mayrhofer et al., 2013), olfactory system (e.g., Laing et al., 1974; Uchida and Mainen, 2003), auditory system (e.g., Kelly and Masterton, 1977; Gaese et al., 2006), and even the response to direct cortical stimulation (e.g., Otto et al., 2005; Butovas and Schwarz, 2007; Huber et al., 2008). The remainder of this dissertation describes the development and execution of a combined rat sciatic nerve and behavioral (CRSNB) model for the measurement of MSE detection thresholds using the method of constant stimuli (MCS).

Chapter 3: The Combined Rat Sciatic Nerve and Behavioral Model

Food-restricted, male, Lewis rats learned a go/no-go detection task to measure psychometric detection thresholds and slopes for various MSE stimuli applied to the sciatic nerve. The probability of stimulus detection at threshold was 50%. The rats were trained with auditory stimuli prior to MSE implantation. After achieving criterion performance (>90% successful detections on two consecutive training days), the rats underwent surgical implantation of the MSE in the right sciatic nerve. During surgery, they also underwent construction of a head-cap containing an embedded connector for interfacing with an external stimulator. Training resumed with auditory stimuli 8-10 weeks post-surgery. Upon reestablishing criterion performance, training progressed to the use of combined auditory and sciatic stimuli presented synchronously. Mid-session suspension of auditory stimuli shaped responses to sciatic stimulation alone. Total suspension of auditory stimuli followed a few sessions later. The rats were subsequently trained with fixed intensity current stimuli until they reached criterion performance. They then progressed to stimulus intensities that varied based on the method of constant stimuli (MCS), in which current amplitudes were selected randomly without replacement from a predefined list. MCS was applied for nine monopolar stimulus configurations – one multi-channel configuration in which equal currents passed through all eight MSE channels simultaneously, and eight single-channel configurations in which each channel passed current alone. The resulting datasets enabled the derivation of psychometric curves depicting the probability of correct stimulus detection as a function of current intensity, and the subsequent calculation of detection thresholds and slopes. **Figure 3.1** summarizes the experimental protocol.
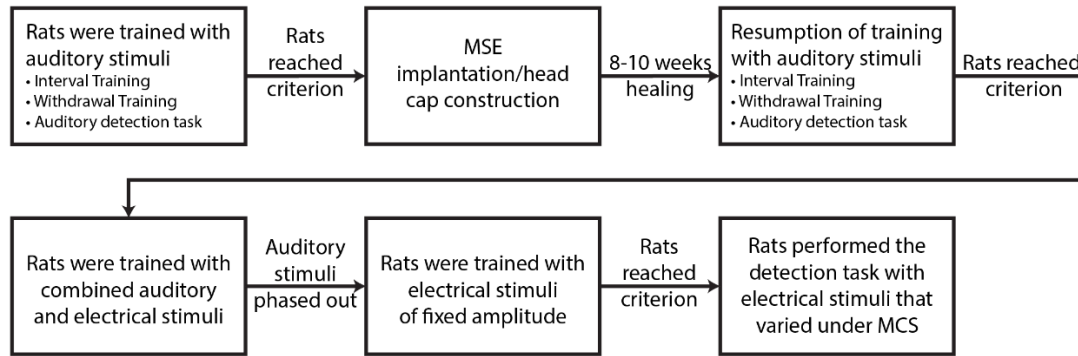
Figure 3.1: Main stages of the experimental protocol.

All experimental procedures were conducted in accordance with regulations specified by the Institutional Animal Care and Use Committee at Washington University School of Medicine in St. Louis.

3.1 Experimental Apparatus

The experimental apparatus consisted of behavioral and electrophysiological modules, a voltage converter that relayed TTL signals between the two modules, and a commutator assembly that relayed stimuli from the electrophysiological module to the implanted MSE (**Figure 3.2**).

3.1.1 Behavioral Module Hardware

Rats performed the go/no-go detection task within the behavioral module, which was built using equipment from Med Associates, Inc. (St. Albans, VT, United States) and Coulbourn Instruments (Lehigh Valley, PA, United States). This consisted of a modular Skinner box (height 12", depth 10", width 12") enclosed within a sound- and light-attenuating chamber. The panel on the Skinner box's right side had three vertical bays (each of width 3"). The central bay housed (from top to bottom) a house light, a 2,900 Hz tone generator, and a nose-poke detector (diameter 1"; centered 2.5" above floor). The left bay housed a rectangular food magazine (width 2¼", height 1¾"; bottom edge was flush with floor) that was connected to a food pellet dispenser for 20-mg food
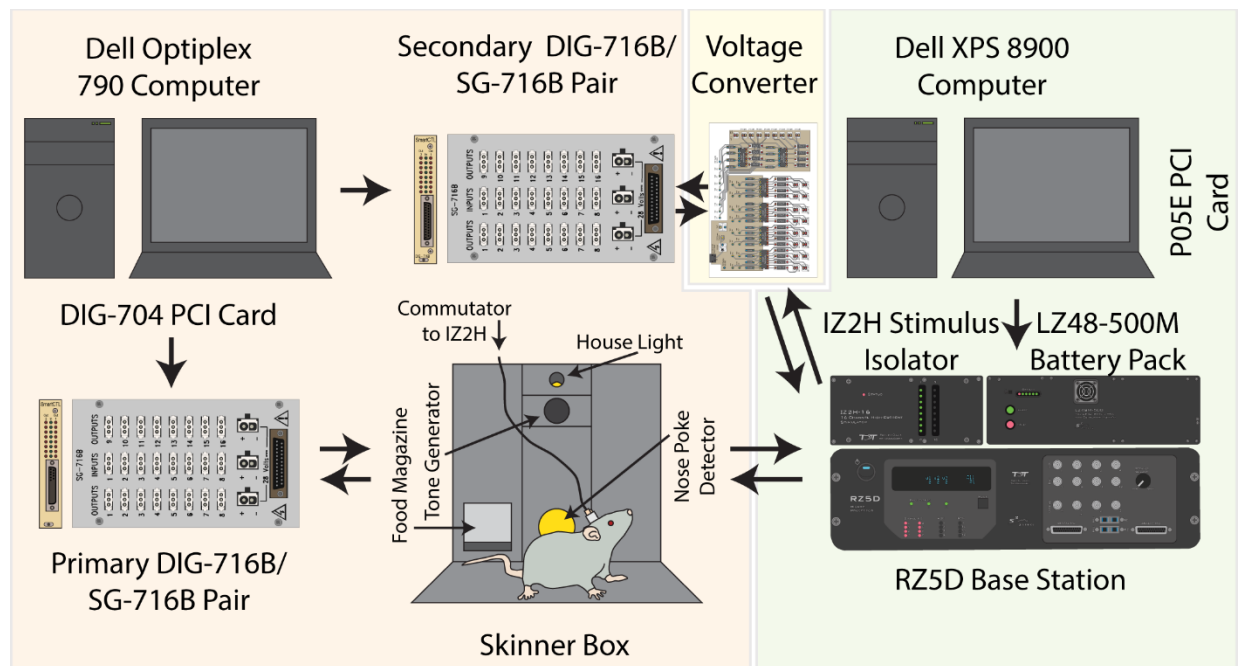
Figure 3.2: Schematic of the experimental apparatus. The behavioral module (highlighted in orange) interfaced with the electrophysiological module (highlighted in green) via the voltage converter (highlighted in yellow).

pellets (BioServ, Prospect, CT, United States; #F0163). The right bay housed no instrumentation. An external, hand-held push button enabled manual interventions such as switching between or combining auditory and electrical stimuli, controlling the house light, or dispensing food pellets.

Holes drilled in the Skinner box's ceiling accommodated a webcam for remote monitoring of rat behavior and the commutator assembly. All protruding edges within the Skinner box (primarily, these were to be found on the food magazine) were milled down in the machine shop to prevent snagging the rat's head-cap and tearing it from the skull. **Figure 3.3** provides a detailed view of the Skinner box interior.

The behavioral module was controlled by a Dell Optiplex 790 computer equipped with a DIG-704 PCI card for controlling multiple Skinner boxes simultaneously. Communications with each Skinner box were mediated by a dedicated DIG-716B SmartCtrl interface module and an SG-716B
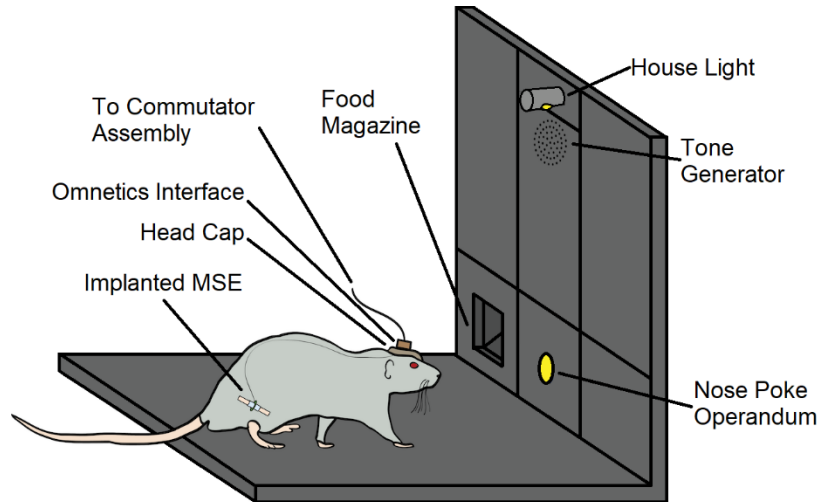
Figure 3.3: Detailed view of the Skinner box interior.
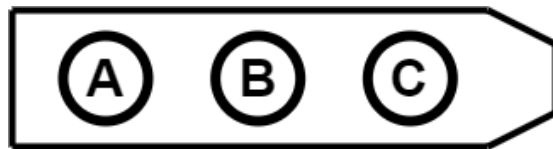
Figure 3.4: The SG-716B SmartCtrl connection panel's 24 channels each had an associated 3-pin Molex connector.
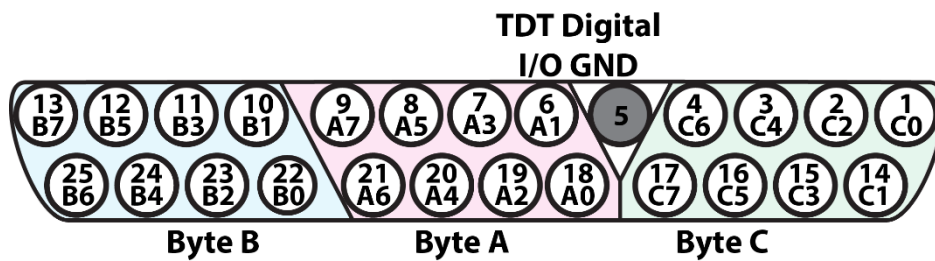
Figure 3.5: The RZ5D base station's digital I/O port.

Table 3.1: Components used in behavioral module.

Item	Manufacturer	Part Number
Computer	Dell	Optiplex 790
PCI Card	Med Associates, Inc.	DIG-704
SmartCtrl Interface Module	Med Associates, Inc.	DIG-716B
SmartCtrl Connection Panel	Med Associates, Inc.	SG-716B
Sound and Light Attenuating Chamber	Med Associates, Inc.	ENV-017M
Modular Test Cage System	Coulbourn Instruments	H10-11R-TC
Shock Floor for Rat Test Cage	Coulbourn Instruments	H10-11R-TC-SF
Drop Pan for Rat Test Cage	Coulbourn Instruments	H10-11R-TC-DP
Nose-Poke Detector	Coulbourn Instruments	H10-09R
Nose-Poke RJ11-to-Molex-Adapter	Coulbourn Instruments	H91-21
Food Magazine	Med Associates, Inc.	ENV-200R2M
Food Magazine Head Entry Detector	Med Associates, Inc.	ENV-254CB
Pellet Dispenser (20 mg)	Med Associates, Inc.	ENV-203-20
House Light	Coulbourn Instruments	E11-01
Tone Generator (2,900 Hz)	Med Associates, Inc.	ENV-223A
Hand-Held Push Button	Med Associates, Inc.	SG-205
Webcam	Ailipu Technology Company	ELP-USB100-W05MT-DL36
Fisheye Lens Attachment for Smartphone	Habor	N/A

SmartCtrl connection panel with 16 output and 8 input channels (**Figure 3.4**). Each channel had a corresponding 3-pin Molex connector (labeled Pin A, Pin B, and Pin C). For all 24 channels, voltages at Pin A and Pin C remained fixed at 28 V and GND, respectively. The 16 output channels behaved as ON/OFF switches by varying ΔV_{AB} between 28 V (ON state) and 0 V (OFF state). The input channels monitored ΔV_{BC} to register the presence (corresponding to $\Delta V_{BC} = 0$ V) or absence (corresponding to $\Delta V_{BC} = 28$ V) of input signals.

In actual practice, the behavioral module used two DIG-716B/SG-716B pairs. The primary pair controlled the Skinner box. The secondary pair relayed signals to and from the voltage converter, enabling the transmission of coordinating TTL signals to and from the electrophysiological module. **Table 3.1** lists all components used in the behavioral module.

Table 3.2: Components used in electrophysiological module.

Item	Manufacturer	Part Number
Computer	Dell	XPS 8900
PCI Card	Tucker-Davis Technologies	P05E
Base Station	Tucker-Davis Technologies	RZ5D
Stimulus Isolator	Tucker-Davis Technologies	IZ2H
Battery	Tucker-Davis Technologies	LZ48-500M
DB26-to-DB25 Adapter	Tucker-Davis Technologies	DBF-MiniDBM

3.1.2 Electrophysiological Module Hardware

The electrophysiological module was controlled by a Dell XPS 8900 computer with an installed P05E PCI card that interfaced with an RZ5D base station. The RZ5D drove an IZ2H stimulus isolator powered by an LZ48-500M battery pack. The IZ2H passed electrical stimuli to the rat's implanted electrode via a custom-made slip-ring commutator assembly and a skull-mounted connector. The IZ2H connected to the commutator assembly via a DB26-to-DB25 DBF-MiniDBM adapter.

The RZ5D had a DB25 digital I/O port (**Figure 3.5**) that served as a TTL signaling interface at voltages up to 5 V. Pin 5 served as GND. The remaining 24 pins were split evenly into 3 bytes of 8 bits each (Byte A, Byte B, Byte C). Bytes A and B were configured to receive incoming TTL signals stepped down from 28 V by the voltage converter (16 bits corresponding to the SG-716B's 16 output channels). Byte C was configured to emit TTL signals to be stepped up to 28 V by the voltage converter (8 bits corresponding to the SG-716B's 8 input channels). **Table 3.2** lists equipment used in the construction of the electrophysiological module.

3.1.3 Voltage Converter Hardware

The voltage converter stepped down 28 V signals from the secondary SG-716B's 16 output channels to TTL signals to be fed into Bytes A and B of the RZ5D's digital I/O port. It also stepped up TTL signals from Byte C of the RZ5D's digital I/O port to 28 V to be fed into the SG-716B's 8 input channels.

Step-Down Circuitry

Figure 3.6A shows the circuit used to step down one SG-716B output channel's signal from 28 V to TTL levels. The circuit's left side had two terminals T1 and T2, corresponding respectively to Pins A and B of the channel's Molex connector. In the OFF state, $V_A = V_B = 28$ V relative to GND so that $V_{12} = \Delta V_{AB} = 0$ V. The two terminals were separated by a 2.7 kΩ resistor in series with an optical relay's LED. The circuit's right side had three terminals T3, T4, and T5. Terminal T3 was separated from T4 and T5 by the optical relay's MOSFET. T4 was connected to one of Byte A or Byte B's bits. A 510 Ω resistor lay between T4 and T5. V_3 was fixed to 3.3 V and V_5 to 0 V relative to TDT GND.

In the absence of current flow across the 510 Ω resistor, $\Delta V_{45} = 0$ V. However, when the SG-716B output channel switched to its ON state, the voltage at Pin B would drop to GND so that $\Delta V_{12} = \Delta V_{AB} = 28$ V. The ensuing flow of current across the optical relay's LED would "open" the MOSFET, allowing current to flow from T3 to T5 and across the 510 Ω resistor so that ΔV_{45} rose to a non-zero value registered as an input signal at Byte A or B.

Step-Up Circuitry

Figure 3.6B shows the circuit used to step up the TTL output of one channel in Byte C to 28 V. On the circuit's left side were two terminals T1 and T2, corresponding to the Byte C channel and TDT GND, respectively. The two terminals were separated by a 510 Ω resistor in series with an
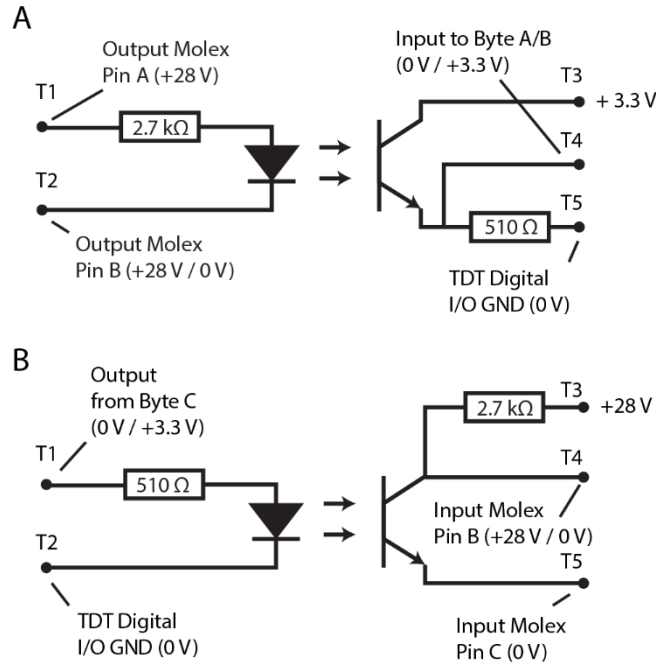
Figure 3.6: (A) Circuit for stepping down output from secondary SG-716B output channel from 28 V to TTL levels, for input into Byte A or Byte B of the RZ5D's digital I/O port. **(B)** Circuit for stepping up TTL output from Byte C of the RZ5D's digital I/O port to 28 V, for input into the secondary SG-716B.

optical relay's LED. On the right side were three terminals T3, T4, and T5. T3 and T4 were separated from T5 by the optical relay's MOSFET. T3 and T4 were separated by a 2.7 kΩ resistor. T4 and T5 corresponded to Pins B and C, respectively, of an SG-716B input channel's Molex connector. The voltages T3 and T5 were fixed at 28 V and 0 V relative to GND, respectively.

When the Byte C channel was in the OFF state, $\Delta V_{12} = 0$ V and no current flowed across the optical relay's LED. The opposing MOSFET remained "closed" so that $\Delta V_{45} = \Delta V_{BC} = 28$ V, which registered as an absence of input at the behavioral module. When the Byte C channel switched ON, the flow of current across the optical relay's LED "opened" the MOSFET so that current flowed from T3 to T5. This dropped V_4 to GND so that $\Delta V_{45} = \Delta V_{BC} = 0$ V, which the behavioral module registered as the presence of an input signal.

Printed Circuit Board

The voltage converter's printed circuit board (PCB) was designed using KiCad and fabricated by Advanced Circuits (Aurora, CO, United States). All components were purchased from Digi-Key (Thief River Falls, MN, United States) and soldered to the PCB by hand (**Table 3.3**). Segments of double-stranded wire were used to connect the PCB to 24 Molex connectors (3-pin) for interfacing with the secondary SG-716B's input and output channels. Care was taken to connect the wire strands to the correct Molex pins – A and B for output channels, and B and C for input channels. Double-stranded wire was also used to connect the PCB board to a 2-pin Molex connector that interfaced with one of the SG-716B's power terminals. Additionally, the 25 wires of a DB25 ribbon cable were soldered to designated through-holes in the PCB. These wires served to transmit signals between the PCB and Bytes A, B, and C of the RZ5D's digital I/O port. All solder joints were reinforced with generous applications of 2-part epoxy (Permatex, Solon, OH). The PCB was secured within a protective enclosure into whose lid were cut holes to accommodate the double-stranded wires and DB25 ribbon cable. **Figure 3.7** illustrates the voltage converter's PCB layout in detail.

Table 3.3: Components used in the construction of the voltage converter's printed circuit board.

Item	Digi-Key Part Number	Quantity
5 V DC Power Supply	Q1039-ND	1
Micro-USB Receptacle	609-4618-1-ND	1
3.3 V Linear Dropout	296-35591-1-ND	1
0.47 mF Capacitor	490-9182-1-ND	1
1 mF Capacitor	490-9146-1-ND	1
Dip Socket	AE9992-ND	6
LTV-847 Opto-Coupler	160-1370-5-ND	6
2.7 kW Resistor	2.7KH-ND	24
510 Ω Resistor	CF14JT510RCT-ND	24
Protective Enclosure	SR172-IA-ND	1
Double-Stranded Wire	CN210BR-100-ND	100 ft
DB25 Ribbon Cable	H7MXH-2506M	1
Molex Housing (3-Pin)	WM1221-ND	24
Molex Crimp Terminals (3-Pin)	WM1000-ND	48
Molex Housing (2-Pin)	23-0019091026-ND	1
Molex Crimp Terminals (2-Pin)	WM1101-ND	2
Sn/Pb Solder (63/37)	82-117-ND	1
Flux	SMD291	1
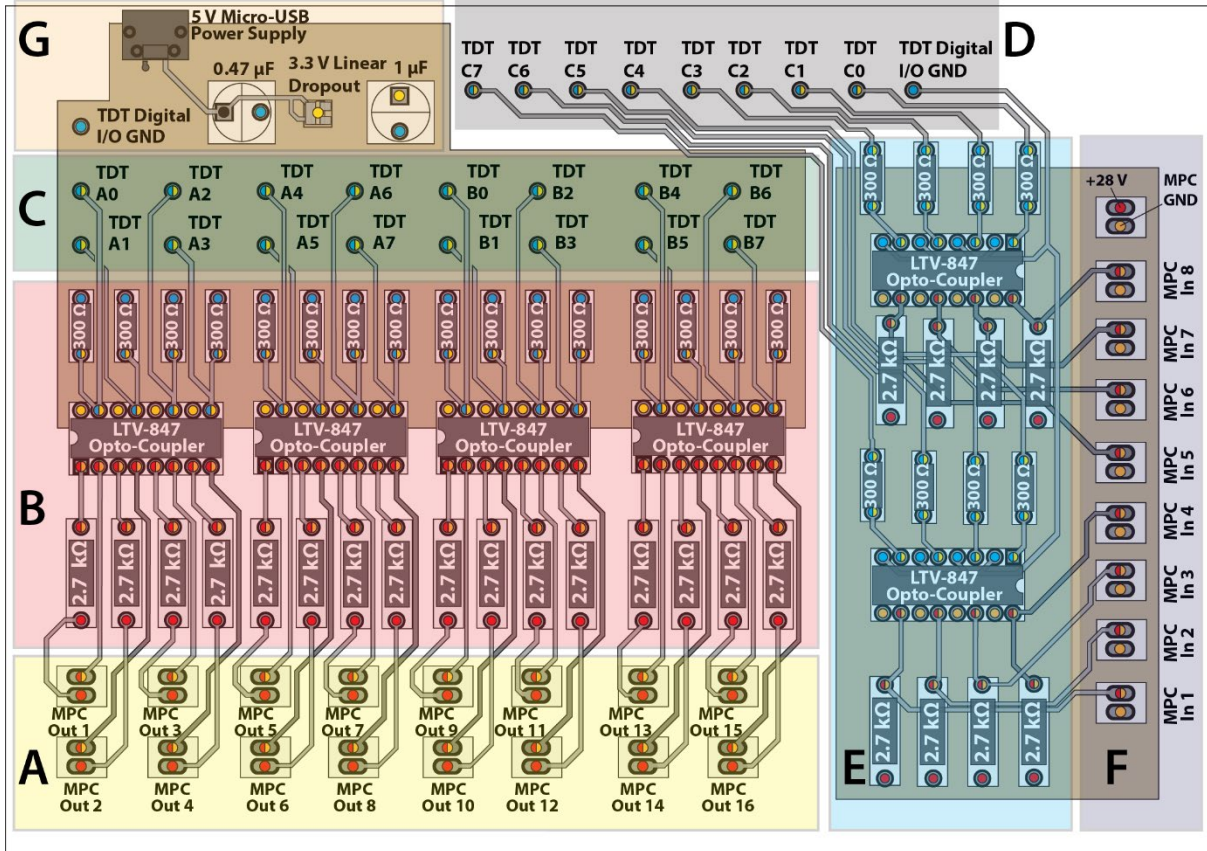
Figure 3.7: The voltage converter's printed circuit board had 7 main regions (labeled **A** through **G**) and two layers (top and bottom). **(A)** This region contained 16 pairs of through-holes labeled MPC Out 1-16. Segments of double-stranded wire were used to connect each through-hole to Pin A and Pin B of a 3-pin Molex connector that interfaced with one of the 16 output channels of the secondary SG-716B. **(B)** This region contained 16 sets of 2.7 kΩ resistors, 510 Ω resistors, and optical relays for stepping 28 V signals down to 3.3 V. The 16 optical relays were housed in four LTV-847 Opto-Coupler chips. **(C)** This region contained 16 through-holes labeled TDT A0-A7 and TDT B0-B7, through which wires from a DB25 ribbon cable were soldered. These wires transmitted stepped down signals to the corresponding pins of Byte A and Byte B in the RZ5D's digital I/O port. **(D)** This region contained 8 through-holes labeled TDT C0-C7, and a 9th labeled TDT Digital I/O GND. These connected with the corresponding pairs of Byte C and TDT GND (pin #5) of the RZ5D's digital I/O port. **(E)** This region contained 8 sets of 2.7 kΩ resistors, 510 Ω resistors, and optical relays for stepping 3.3 V signals up to 28 V. The 8 optical relays were housed in two LTV-847 Opto-Coupler chips. **(F)** This region contained 8 pairs of through-holes labeled MPC In 1-8. Segments of double-stranded wire were used to connect each through-hole with Pin B and Pin C of a 3-pin Molex connector that interfaced with the 8 input channels of the secondary SG-716B. **(G)** This region contained a micro-USB receptacle compatible with a 5 V DC power supply, a linear dropout chip that dropped the power supply's voltage from 5 V to 3.3 V, and two stabilizing capacitors of 0.47 µF and 1 µF. A second through-hole labeled TDT Digital I/O GND (the same label as that found in Region D) was also connected to TDT GND (pin #5) of the RZ5D's digital I/O port via the DB25 ribbon cable.

3.1.4 Commutator Assembly

The commutator assembly allowed the rat to remain connected to the IZ2H stimulus isolator and move freely without torsioning the wires. It consisted of a 12-channel slip-ring commutator (AdaFruit Industries, New York, NY, United States; #1196) soldered to a latched, female connector (Omnetics Connector Corporation, Minneapolis, MN, United States; #A76855-001). A flexible sheath of stainless steel "spring wrap" (Tollman Spring Company, Bristol, CT, United States) enclosed the connector's microwires and protected them from gnawing.

The connector's wires were of sufficient length to allow free movement to the farthest corners of the cage. However, when the rat stood directly beneath the slip-ring, which was affixed to one of the holes drilled into the Skinner box's ceiling, the same wires were too long and the rat risked entanglement. To mitigate this risk, a low-force extension spring (McMaster-Carr, Elmhurst, IL, United States; #9654K513) was attached to the sheath with heat-shrink tubing, forming a loop that absorbed excess slack and prevented entanglement as the rat moved about the Skinner box. When the rat moved to a far corner, the spring extended and the loop straightened out. When the rat returned beneath the slip-ring, the spring contracted and the wires formed a loop once more. **Figure 3.8** shows the commutator assembly in its contracted and extended configurations.

Based on the cage's dimensions, the extension spring had to accommodate a change in wire length of 3.2" for when the rat moved from beneath the slip-ring to the cage's farthest corner. I chose McMaster-Carr's 9654K513 extension spring for its low spring constant (0.04 lb./in.) and high extensibility. The spring had a baseline length of 2". I set the length of the loop to equal the length of the maximally extended spring ($2+3.2 = 5.2" \rightarrow$ rounded up to 5.5").
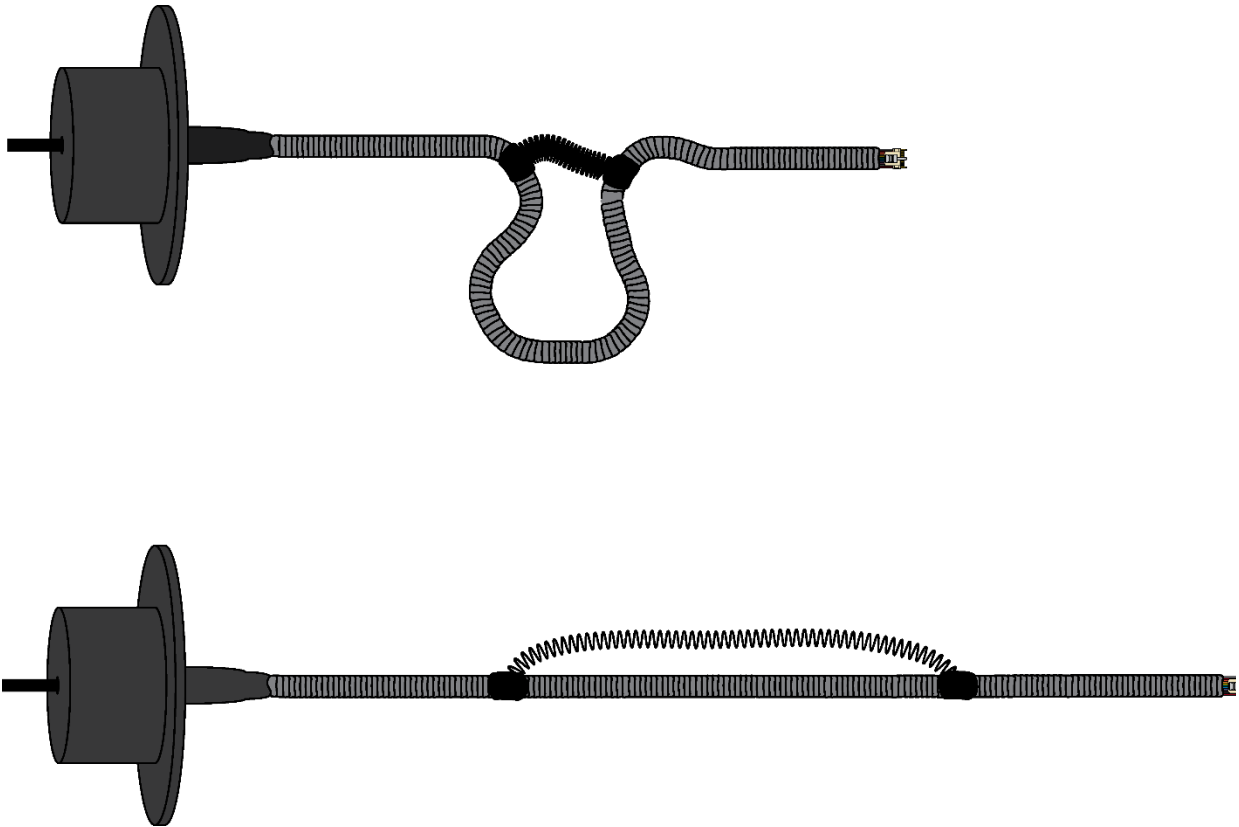
Figure 3.8: The commutator assembly in its *(top)* contracted and *(bottom)* extended configurations.

Construction of the commutator proceeded as follows:

Step 1: Cut the Omnetics connector's 18 wires to 14.25".

Step 2: Thread the Omnetics wires through a ½"-long heat-shrink tube and abut the tube against the connector.

Step 3: Shrink the tube with a heat gun.

Step 4: Strip each Omnetics wire at the tip (0.2") using the heat from a cigarette lighter.

Step 5: Thread the wires through 12⅜" of spring wrap.

Step 6: Use a second heat-shrink tube of length ½" to secure the spring wrap to the first tube from Step 2.

Step 7:   Slip two additional ¾"-long heat-shrink tubes over the spring wrap. Do not shrink until Step 12.

Step 8:   The slip-ring has two sides – one wide and one narrow. On the wide side, solder 8 of the 12 slip-ring wires to channels 1, 2, 3, 4, 7, 8, 20, and 21 of a male DB25 connector. Solder the remaining 4 wires, two-apiece, to channels 15 and 16. Make sure to reinforce and insulate each solder joint with an appropriately sized heat-shrink tube.

Step 9:   On the slip-ring's narrow side, cut the 12 wires to 1" and use a wire stripper to expose the tips (½").

Step 10:   Solder the wires to the Omnetics connector using the mapping in **Table 3.4**. Ensure that each solder joint is insulated by a heat-shrink tube.

Step 11:   Encase the 12 insulated solder joints from Step 10 in a 1–2"-long piece of large diameter heat-shrink, which should be pushed all the way up to the slip-ring's base.

Step 12:   Secure the extension spring by poking its ends through the unshrunk tubes from Step 7. Position the tubes 5.5" apart along the spring wrap's length and shrink with the heat gun.

Step 13:   Reinforce all exposed heat-shrink tubes with liberal applications of 2-part epoxy. Cure for 24 hours. **Table 3.5** lists all components used in the commutator's assembly.

Table 3.4: Channel mappings for commutator assembly's Omnetics and DB25 connectors.

Omnetics Connector	DB25 Channel
1	Unused
2	Unused
3	Unused
4	Unused
5	Unused
6	Unused
7	15
8	15
9	16
10	16
11	1
12	2
13	3
14	4
15	7
16	20
17	8
18	21

Table 3.5: Components used in commutator assembly.

Item	Manufacturer	Part Number
Slip-Ring	Prosper (Adafruit)	SRC022A-12 (1196)
Latched, Female Connector	Omnetics Connector Corporation	A76855-001
Extension Spring	McMaster-Carr	9654K513
Silicone Adhesive	Factor II, Inc.	A-564
2-Part Epoxy	Permatex	84101
DB25 D-Sub Connector	Digi-Key	225ME-ND
Solder (Sn/PB 63/37)	Multicore	MM00978
Flux	Chip Quick, Inc.	SMD291
Soldering Station	Weller	WX1
Soldering Tip	Weller	RT 5MS, RT 13MS, RT 15 MS

3.1.5 Programming the Behavioral Module

The behavioral module's hardware operated on a hardware-specific, state-based programming language called Med-State Notation (MSN). The fundamental unit of code in MSN was the "state," clusters of which were organized into "state sets." Although multiple state sets could run concurrently within the same program, within a state set only one state could run at once. Each state contained one or more command sequences to be executed when corresponding conditions were met. Example conditions that could trigger command sequence execution included the completion of a fixed time interval (e.g., the passage of 1 s after state initiation), receiving a signal from an SG-716B input channel, receiving a "Z-pulse" signal from another state set running concurrently within the same program (i.e., running on the same DIG-716B/SG-716B pair), or receiving a "K-pulse" signal from a state set running concurrently in a different program (i.e., running on a different DIG-716B/SG-716B pair). Each command sequence terminated with a
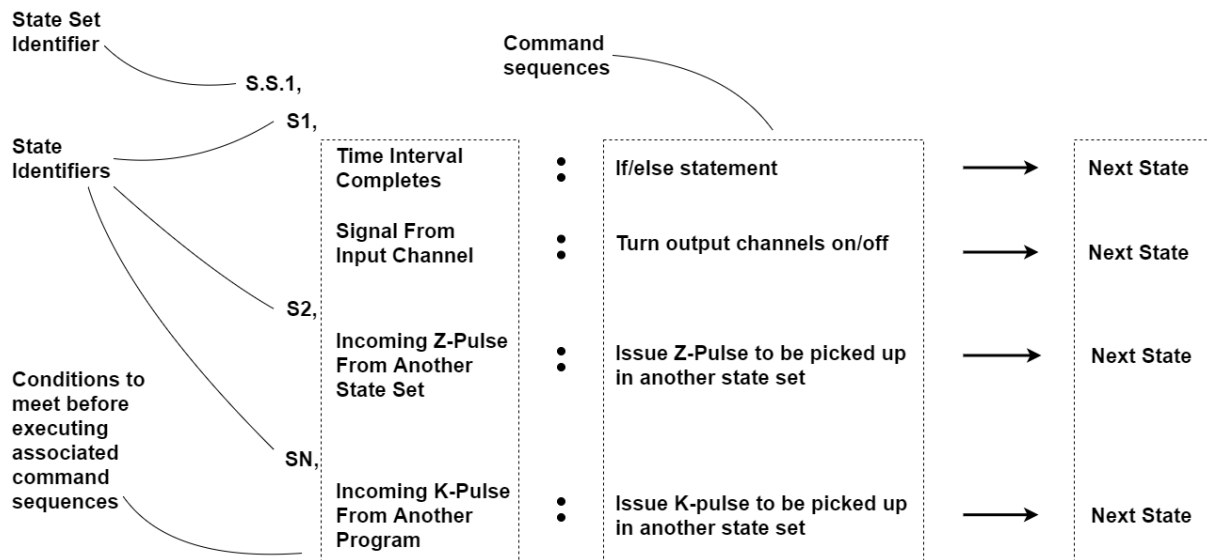
Figure 3.9: Structure of a generalized state-set written in Med-State Notation.

directive to move to another state set within the same state set or to repeat the current state set. **Figure 3.9** depicts the structure of a generalized state set.

The primary and secondary DIG-716B/SG-716B pairs ran separate MSN programs in parallel. The primary MSN program encoded the logic of the behavioral task. Six types of events caused this program to issue corresponding K-pulses. These events were: (1) stimulus onset, (2) early withdrawal from the nose-poke detector, (3) correct withdrawal, (4) late withdrawal, (5) session start, and (6) session termination. A K-pulse issued upon the occurrence of one of these events would be picked up by corresponding states in the secondary MSN program, triggering the execution of a command sequence that switched ON a pair of output channels. This, in turn, activated a pair of step-down circuits in the voltage converter, which transmitted TTL signals to a pair of corresponding bits in Byte A and B of the RZ5D's digital I/O port. (This association of each K-pulse with 2 output channels helped to block erroneous inputs to the RZ5D caused by noise in the secondary SG-716B or voltage converter.) The simultaneous arrival of stepped-down TTL signals at Byte A and Byte B induced the program running on the electrophysiological module to issue a signal of confirmation from Byte C, to be stepped up and returned to the behavioral module via one of the secondary DIG-716B/SG-716B pair's input channels. This would cause the secondary MSN program to issue a K-pulse to be picked up by the primary, which then continued with the behavioral task having received confirmation of signal receipt. The described sequence is depicted in **Figure 3.10**.

Primary DIG-716B/SG-716B Pair

Principal State Set — Z-Pulse → Subsidiary State Set

Subsidiary State Set — Z-Pulse → Principal State Set

K-Pulse → / K-Pulse →

Secondary DIG-716B/SG-716B Pair

State Set — Switch ON 2 channels / Switch OFF 2 channels → Secondary SG-716B

Voltage Converter

28 V output signals

28 V input signals

3.3 V stepped down signals

3.3 V confirmation of receipt returned to behavioral module

Electrophysiological Module

RZ5D Digital I/O Port

Byte A | Byte B | Byte C

Figure 3.10: The sequence of events underlying the transmission of a signal from the behavioral module to the electrophysiological module and the subsequent return of a confirmatory signal.

MSN programs operated on the basis of "interrupts" that occurred every 5 ms. During an interrupt, the controlling computer checked each state-set's current state, executed the first available command whose condition was met (if any), and updated the current state based on the executed command sequence's terminating directive. Only one command sequence could execute per interrupt for a given state-set. Thus, these interrupt-based programs had an effective frame rate of 200 Hz and a time resolution of 5 ms. (It should be noted that the time resolution and frame rate were adjustable through Med Associate's Hardware Configuration Utility.)

The nose-poke detector registered an ON signal for each interrupt in which the rat's snout disrupted the detector's infrared beam. Minor movements of the head, snout, or whiskers during snout insertion engaged and disengaged the infrared beam rapidly across successive interrupts, resulting in incorrectly registered withdrawals. The chances of registering false withdrawals were high since insertions had to persist for up to 4.5 seconds (corresponding to 900 interrupts). The introduction of a "smoothing factor" helped to mitigate false withdrawal registration. The smoothing factor was an integer that specified how many interrupts must pass after disengaging the infrared beam before withdrawal registration could occur. It was set to 30, corresponding to a 150-ms delay in withdrawal registration. Thus, if the ON signal re-engaged less than 150 ms after disengaging, it
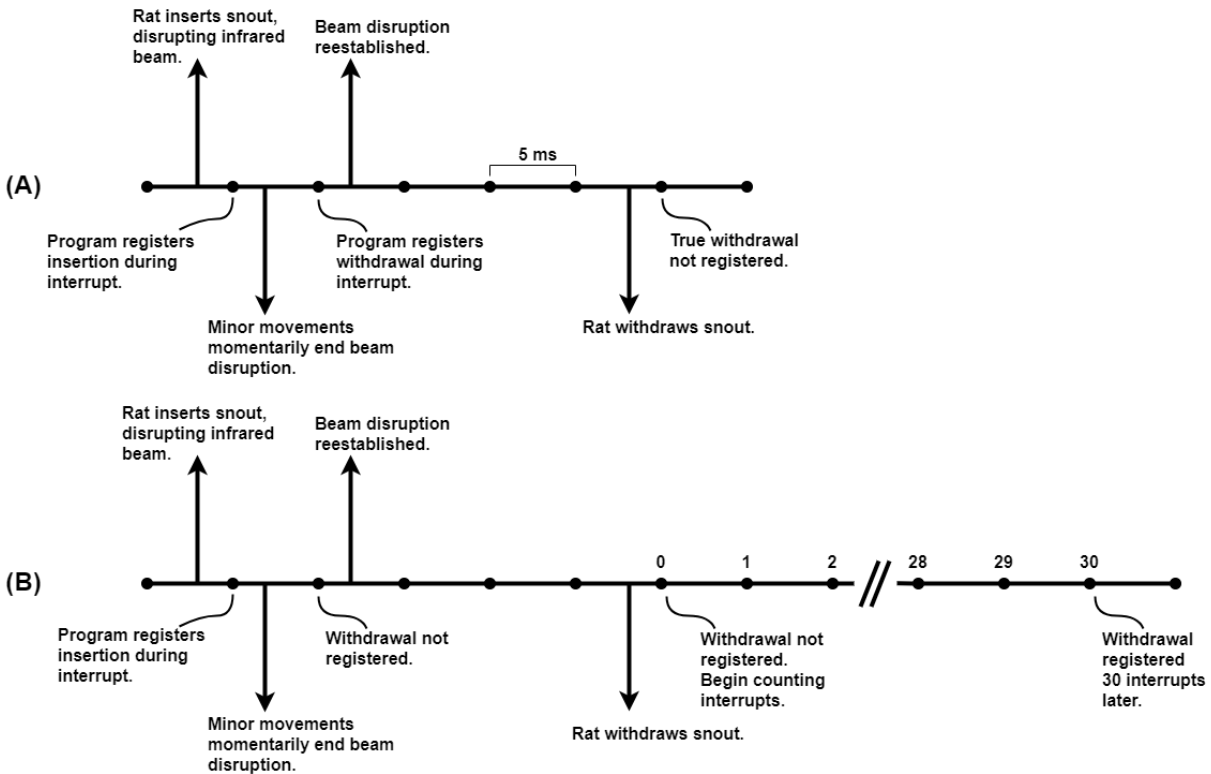
Figure 3.11: (A) The Med-State Notation programming language relied on interrupts, represented here by dots. Under normal operation, rapid disengagement and reengagement of an input signal, such as that stemming from the nose-poke detector, could inadvertently register as withdrawals. **(B)** The introduction of a smoothing factor helped mitigate this effect. By delaying withdrawal registration by a given number of interrupts (in our case, 30), the smoothing factor enabled inadvertent breaks in the input signal to be negated by subsequent reengagements.

was as if no withdrawal had occurred – the snout insertion continued uninterrupted. The 150-ms delay was accounted for when calculating the true duration of insertion. **Figure 3.11** illustrates how interrupts caused false withdrawals and how the smoothing factor prevented them.

3.1.6 Programming the Electrophysiological Module

The electrophysiological module was programmed using TDT's RPvdsEx graphical programming environment, which allows precise control of TDT digital signal processors without the need to understand programming in low-level assembly code. Programs written in this environment take the form of "circuits" comprised of linked graphical components that have predetermined functions. An RPvdsEx circuit running in the OpenEx Software Suite monitored the RZ5D's
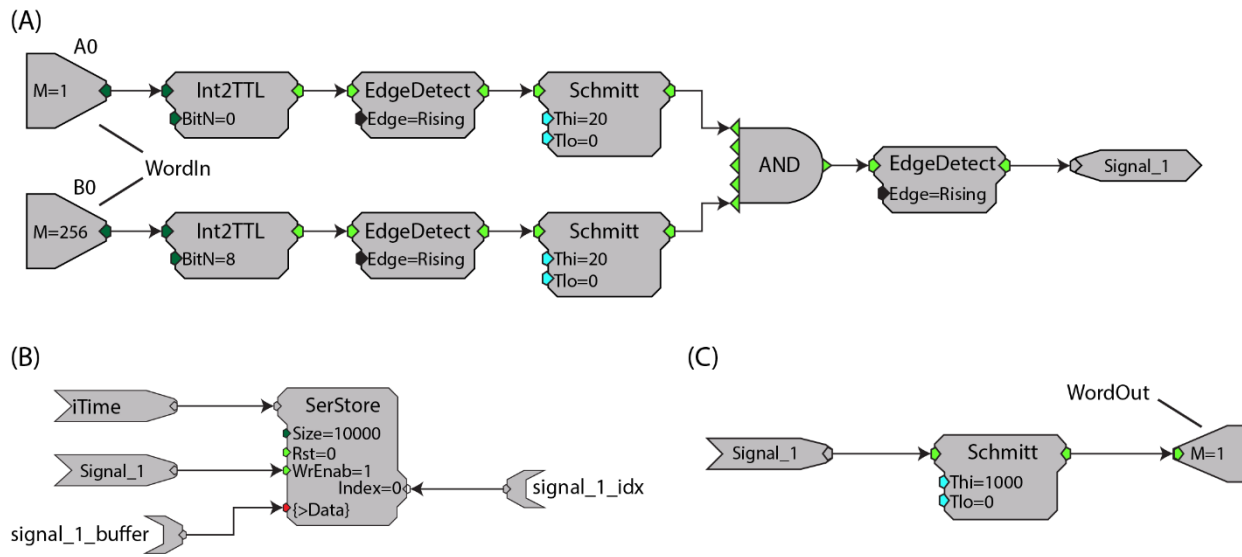
Figure 3.12: (A) RPvdsEx circuit for registering the arrival of TTL signals at Byte A/Bit 0 and Byte B/Bit 0. **(B)** RPvdsEx circuit for updating the tagged index associated with "Signal 1" to be retrieved by the MATLAB script. **(C)** RPvdsEx circuit for returning a confirmatory signal to the behavioral module via Byte C/Bit 0.

digital I/O port for incoming signals from the behavioral module. These signals included a command to trigger the stimulus, notifications of early, correct, or late withdrawals, and notifications that the behavioral experiment had started or ended. Each signal updated a corresponding buffer in the RPvdsEx circuit with the current system time and incremented by one an associated index. A script written in the MATLAB programming language sampled each index once every 10 ms and took appropriate action whenever a buffer-value changed.

Figure 3.12 depicts representative RPvdsEx circuits that facilitated communications with the behavioral module. The first circuit (**Figure 3.12A**) registered TTL signals arriving from the behavioral module via the voltage converter. The depicted circuit addressed the two WordIn components to Byte A/Bit0 and Byte B/Bit 0 by setting their M-parameters to 1 and 256, and their BitN-parameters to 0 and 8, respectively. Similar circuits were directed towards other addresses by using the M- and BitN-parameter values listed in **Table 3.6**. The use of an AND gate ensured that erroneous signals from Byte A or Byte B remained unregistered. The circuit outputted a so-

72

Table 3.6: Mapping from Byte A, Byte B, and Byte C of the RZ5D digital I/O port to M- and BitN-parameters for use in the RPvdsEx circuit.

Bit Address	M-Parameter			BitN-Parameter		
	Byte A	Byte B	Byte C	Byte A	Byte B	Byte C
Bit 0	1	256	1	0	8	N/A
Bit 1	2	512	2	1	9	N/A
Bit 2	4	1,024	3	2	10	N/A
Bit 3	8	2,048	4	3	11	N/A
Bit 4	16	4,096	5	4	12	N/A
Bit 5	32	8,192	6	5	13	N/A
Bit 6	64	16,384	7	6	14	N/A
Bit 7	128	32,768	8	7	15	N/A

Table 3.7: Designated function of each RZ5D digital I/O port bit.

Byte/Bit	Function
A0, B0	Trigger stimulus
A1, B1	Register early withdrawal
A2, B2	Register good withdrawal
A3, B3	Register late withdrawal
A4, B4	Register session start
A5, B5	Register session end
A6, B6	Not used
A7, B7	Not used
C0	Confirm receipt of stimulus trigger
C1	Confirm receipt of early, good, or late withdrawal notification
C2	Confirm receipt of session start notification
C3	Confirm receipt of session end notification
C4	Inform behavioral module that all stimuli have been applied
C5	Not used
C6	Not used
C7	Not used

called "Hop-To" component labeled "Signal_1" that linked this circuit with the other two circuits presented. The second circuit (**Figure 3.12B**) passed Signal_1 into a SerStore (i.e., serial storage) component's WrEnable-parameter. This logged the clock's current time (iTime) in the buffer tagged "signal_1_buffer," and incremented by one the index tagged "signal_1_idx." Changes to this index were detected by the MATLAB script, prompting the execution of appropriate commands. The third circuit (**Figure 3.12C**) passed Signal_1 into a 1,000-ms Schmitt trigger component that fed into a WordOut component addressed to Byte C/Bit 0. Similar circuits were directed to the other bits of Byte C using the M-value mapping shown in **Table 3.6**. This is how

confirmatory signals were returned to the behavioral module via the voltage converter. **Table 3.7**

lists the programmatic role of each bit in the RZ5D's digital I/O port.

The MATLAB script used TDT's ActiveX controls to programmatically interact with the RPvdsEx

circuit running in the OpenEx Software Suite. First, a connection between the MATLAB script

and TDT hardware was established using the following code snippet:

```matlab
h = figure('Visible', 'off', 'HandleVisibility', 'off');
DA = actxcontrol('TDevAcc.X', 'Parent', h);
DA.ConnectServer('Local');
fprintf('Connection to TDT initiated.\n');
```

Next, the MATLAB script used the command below to commence execution of the RPvdsEx

circuit within OpenEx. Note that sysModeCode = 2 corresponds to OpenEx's "Preview" mode.

Other possible values include 0 ("Idle" mode), 1 ("Standby" mode), and 3 ("Record" mode).

Preview mode was chosen over Record mode because all data logging was performed by the

MATLAB script instead of OpenEx's inbuilt data tank mechanism.

```matlab
sysModeCode = 2;
if DA.GetSysMode ~= sysModeCode
  while(DA.GetSysMode ~= sysModeCode)
    pause(0.01);
  end
end
```

The transfer of data between MATLAB and the RPvdsEx circuit relied on the use of tag

components (see **Figure 3.12B**) in conjunction with the ActiveX commands DA.ReadTargetVEX,

DA.GetTargetVal and DA.SetTargetVal. The DA.ReadTargetVEX command was used to pull data from

buffered tags. For example, the following command pulled the latest stored value in the buffer

tagged "signal_1_buffer":

```matlab
t=DA.ReadTargetVEX('RZ5D.signal_1_buffer',idx.signal_1.current-    1,1,'I32','I32');
```

The `DA.GetTargetVal` command was used to pull scalar values from the RPvdsEx circuit. For example,

idx=DA.GetTargetVal('RZ5D.signal_1_idx');

The DA.SetTargetVal command was used to set scalar values as follows:

DA.SetTargetVal('RZ5D.DemoSetValue', 1);

The MATLAB script ran a while-loop that repeated approximately once every 10 ms. Each loop iteration used `DA.GetTargetVal` to look up tagged index values associated with the SerStore components described earlier. By comparing each index with its value from the previous loop iteration, the MATLAB script could detect the arrival of TTL signals from the behavioral module via the voltage converter and take appropriate actions, which included logging TTL-signal arrivals (the resulting log file would later be collated with log data from the behavioral module) and using DA.GetTargetVal to set the current amplitude for the next round of stimulation based on MCS.

The introduction of variable current amplitudes presented in random order raised the possibility of multiple successive stimuli falling below the detection threshold. To sustain the rat's responding in the face of such repeated subthreshold stimuli, the MATLAB script defined two modes of stimulation. For "normal" trials, the script pulled stimulus amplitudes from the predefined MCS list. Failure to detect the stimulus over 1-3 consecutive normal trials caused the script to switch to "maintenance" mode, wherein the stimulus intensity was fixed at the lowest value known to elicit a visible muscle twitch in the right hind leg and foot without evident pain. **Figure 3.13** summarizes the workings of the OpenEx/RPvdsEx circuit and the MATLAB script.
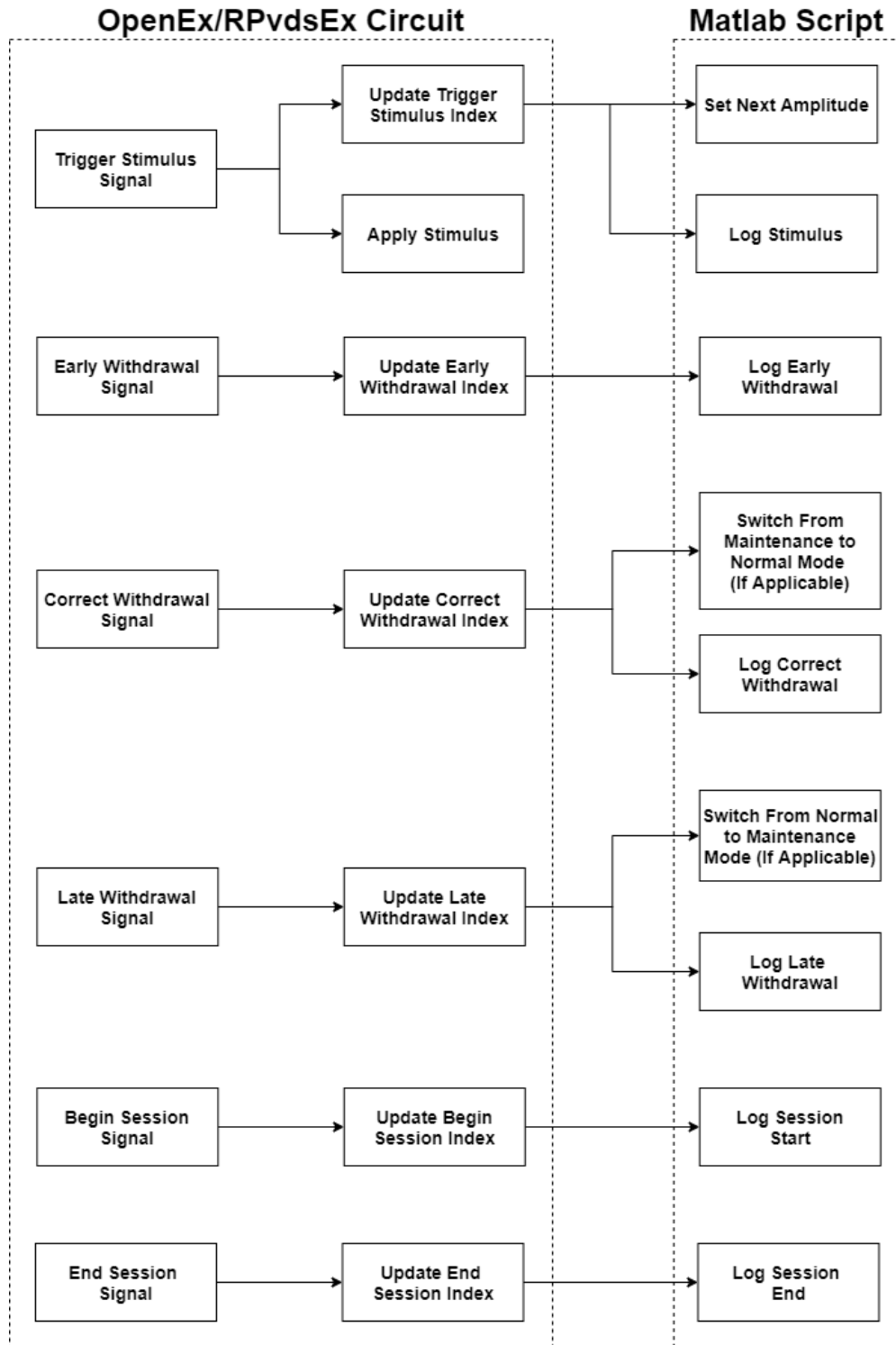
Figure 3.13: Programming schematic for the electrophysiological module depicting the interactions between the OpenEx/RPvdsEx circuit and MATLAB script.

3.2   The Macro-Sieve Assembly

The macro-sieve assembly consisted of an MSE, a latched, male connector (Omnetics Connector Corporation, Minneapolis, MN, United States; #A76854-001), a pair of silicone guidance conduits (inner diameter: 2 mm; A-M Systems, Sequim, WA, United States, #808500) affixed to the MSE's polyimide on either side, a small quantity of medical grade silicone adhesive (Factor II, Lakeside, AZ, United States, #A-564), and Parafilm (Bemis Company, Inc., Neenah, WI, United States).

Preparation of the macro-sieve assembly proceeded as follows (**Figure 3.14**):

Step 1:   Remove wires for channels 1-6 of the Omnetics connector using a pair of scissors.

Step 2:   Cut wires for channels 7-10 of the Omnetics connector to 2½" and strip them of all insulation using a cigarette lighter, taking care not to remove the insulation of any other wires.

Step 3:   Cut wires for channels 11-18 to 8¾" and strip the tips using the cigarette lighter. Solder these wires at 290°C to the MSE's eight through-holes using a lead-free alloy (96.5% Sn, 3% Ag, 0.5% Cu) and a no-clean flux (Chip Quick, Inc., Ancaster, ON, Canada; #SMD291), using the mapping shown in **Table 3.8**. The soldered joints should be conical and shiny. If they are bulbous or look pockmarked, it suggests poor electrical connectivity between the wire and the solder pad.

Step 4:   Cut a pair of 4-mm long silicone guidance conduits under a microscope, using a sharp razor blade and a ruler for measurement. Wash with isopropyl alcohol.

Step 5:   Affix the silicone guidance conduits to either side of the Omnetics connector using the A-564 silicone adhesive. This is best accomplished by mounting each conduit in turn on a specially-built stand (under the microscope), and applying a very small

quantity of the adhesive using a 3-ml syringe with a 21-gauge, ½"-long blunt-tipped needle. Next, holding the MSE by the attached Omnetics wires split evenly between both hands, lower the MSE's polyimide ring onto the mounted conduit so that the active region lines up as closely as possible to the conduit's lumen. Take care that no adhesive smears into the MSE's active region when pressing the MSE against the conduit. If any adhesive should intrude upon the MSE's radial spokes or central hub, then there is a good chance that some or all channels will be unable to pass any current. It may be preferable to affix the two conduits on successive days. In any case, make sure to wait 24 hours for the adhesive to cure between steps.

To explain how small a quantity of adhesive is recommended, it is best to depress the syringe's plunger slightly so that a tiny bubble of adhesive extrudes from the needle. Touch this bubble to the outer edge of the conduit's rim and then pull the syringe away a few inches so that the bubble turns into a thread-like filament. Using one hand, rotate the stand upon which the conduit is mounted while using the other hand to adjust the placement of the syringe so that the adhesive filament is laid around the conduit's circumference. It is best for the adhesive filament to lie as near as possible to the conduit rim's outer edge – this can be ensured by using a 0.5 ml insulin syringe's needle to push any errant adhesive towards the edge.

Step 6: Apply more adhesive on both sides of the MSE's PCB to insulate the solder joints and provide mechanical support to the conduit/polyimide interface. Repeat this step as many times as needed, allowing the adhesive to cure for 24 hours between repetitions.

Step 7:   Measure channel impedances at 1 kHz and 5 kHz using an Autolab PGSTAT128N potentiostat. A "good" MSE is one whose channel impedances are all <100 kΩ at 5 kHz.

Step 8:   Wrap the stripped wires (channels 7, 8, 9, and 10) loosely around the Omnetics connector, taking care not to fray them. Wrap the Omnetics connector and stripped wires in a protective layer of Parafilm.

Step 9:   Sterilize with ethylene oxide a few days prior to implantation.

Initially, I used unlatched Omnetics connectors (A79044-001, A79045-001), which had functioned well in stimulation experiments in which the rat was anesthetized under isoflurane. However, these did not translate well to the ambulatory environment of the Skinner box, as they would detach from each other as the rat moved around. This motivated my switch to latched Omnetics connectors (A76854-001, A76855-001), which are rated to withstand up to 30 lbs. of pull before breaking – a far greater force than any rat is likely to exert.

Table 3.9 lists all components used in the construction of the macro-sieve assembly.
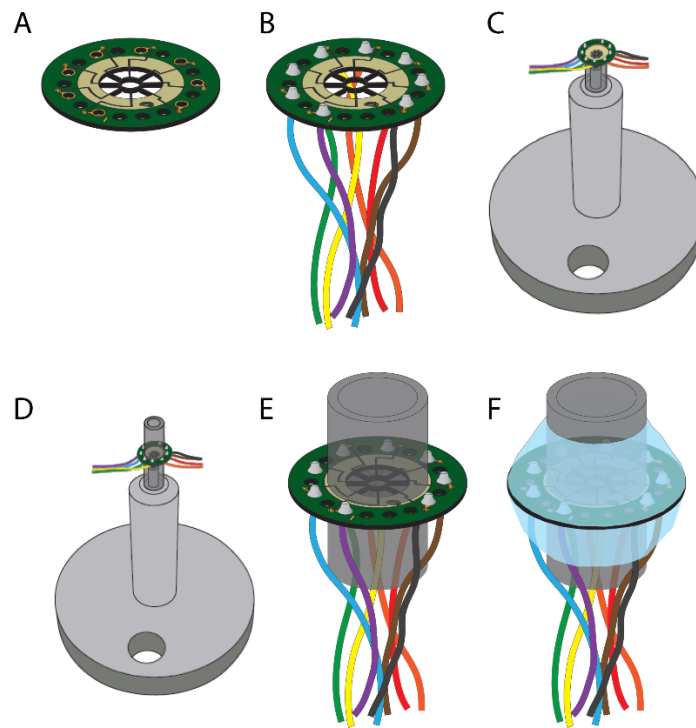
Figure 3.14: (A) A new macro-sieve electrode. **(B)** MSE with soldered Omnetics micro-wires. **(C)** Attaching the first silicone conduit. **(D)** Attaching the second silicone conduit. **(E)** MSE with two silicone conduits prior to insulation. **(F)** Completed MSE/Omnetics assembly with insulating layers of silicone adhesive.

Table 3.8: Mapping between Omnetics connector, MSE, and commutator assembly's DB25 connector.

Omnetics Channel	Wire Status	MSE Channel	DB25 Channel
1	Removed	-	-
2	Removed	-	-
3	Removed	-	-
4	Removed	-	-
5	Removed	-	-
6	Removed	-	-
7	2½", stripped	-	15
8	2½", stripped	-	15
9	2½", stripped	-	16
10	2½", stripped	-	16
11	8¾", soldered	P3	1
12	8¾", soldered	C4	2
13	8¾", soldered	P4	3
14	8¾", soldered	C1	4
15	8¾", soldered	P1	7
16	8¾", soldered	C2	20
17	8¾", soldered	P2	8
18	8¾", soldered	C3	21

Table 3.9: Components used in the construction of the macro-sieve assembly.

Item	Manufacturer	Part Number
Latched, Male Connector	Omnetics Connector Corporation	A76854-001
Macro-Sieve Electrode	NeuroNexus Technologies	N/A
Silicone Conduit	A-M Systems	808500
Silicone Adhesive	Factor II, Inc.	A-564
Parafilm	Bemis Company	-
Solder (Sn/AG/CU 96.5/3.0/0.5)	Henkel	C 511 97SC 3C 0.38MM G
Flux	Chip Quick, Inc.	SMD291
Soldering Station	Weller	WX1
Soldering Tip	Weller	RT 5MS, RT 13MS, RT 15MS

3.3 Training Rats with Auditory Stimuli

3.3.1 Acclimation and Food Restriction

This study used male, Lewis rats (Charles River Laboratories, Wilmington, MA, United States; Strain #004) that were ordered at 5 weeks of age. Upon receipt, the rats were acclimated to the rodent housing facility, human handling, and finally the Skinner box over a period of 1-2 weeks. Acclimated rats then commenced food restriction, which entailed access to food for 1 hour per day, or providing a pre-measured quantity that they would typically eat in 1 hour of unrestricted access (5-15 g depending on the rat's size). The rats' weights dropped to roughly 80% of free-feeding values under this protocol. Weights were monitored each weekday (M-F). Rats that dropped below 80% pre-restriction weight were returned to unlimited food access.

3.3.2 Manual Shaping Stage

The rats were shaped to eat from the food magazine and subsequently insert their snouts into the nose-poke detector using manual release of food pellets while monitoring behavior over a webcam. A naïve rat placed in the Skinner box would move around all parts of the cage. Release of a food pellet (using the hand-held push button) whenever the rat approached the food magazine caused the rat to quickly associate the magazine with pellets. However, now the rat would insert its head into the magazine without interruption, awaiting the next pellet's release. To discourage this

unwanted behavior, the next pellet's release was contingent upon the rat's withdrawal from the magazine. In this manner, the rat not only learned to withdraw from the magazine, but gradually learned to move around the cage and return only upon the release of a pellet. I repeated this stage over 2-3 daily sessions lasting 30-60 minutes each.

The rat next learned to interact with the nose-poke detector. Pellet release was now contingent upon the rat's approach towards the detector. Over successive trials, the rat had to move progressively closer to the detector in order to trigger pellet release. Eventually, the rat's snout would interrupt the detector's infrared beam, triggering the release of a food pellet without a manual button press. In general, the rat would make the required association between the nose-poke insertion and pellet release almost immediately (i.e., in as few as one trial). It would then bounce back and forth between the food magazine and nose-poke detector without the need for manual intervention (method of successive approximations). I repeated this stage over 2-3 daily sessions, lasting 30-60 minutes each.

3.3.3 Interval Training Stage

During manual shaping, the rat inserted its snout into the nose-poke detector for a few milliseconds before triggering the release of a pellet into the magazine. In the next training stage, the rat learned to insert its snout into the nose-poke detector for progressively longer intervals. On a given trial, maintaining uninterrupted insertion for the currently prescribed interval counted as a successful response and triggered reinforcement and an accompanying auditory tone lasting 500 ms. Failure to maintain insertion for the prescribed interval counted as a failure and resulted in a 7-s timeout with the house light switched off. The interval I_C was incremented by $\Delta_+ = 0.5$ s when the number of consecutive successes N_S exceeded a preset limit S_{Lim}, up to a maximum interval $I_{\max}$. Similarly,
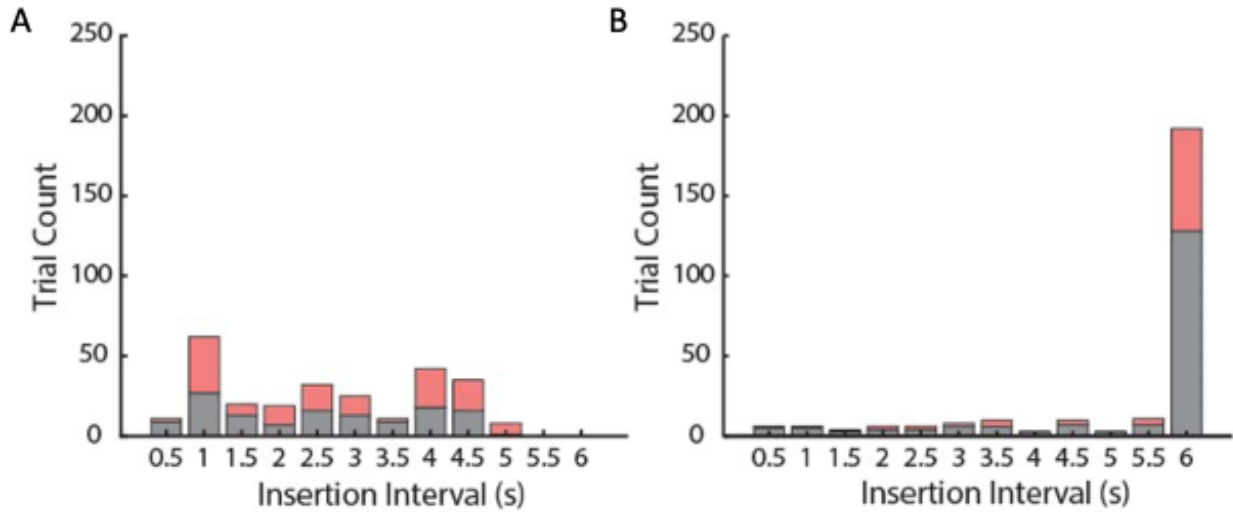
Figure 3.15: Insertion interval training data for a representative rat on the **(A)** first and **(B)** fourth days of training. The distribution of successful (black) and failed (red) insertions across several different intervals changed significantly between the two training days, signifying that the rat had learned to maintain insertion without interruption for longer intervals.

it was decremented by $\Delta_- = 0.5$ s when the number of consecutive failures N_F exceeded another preset limit F_{Lim}, down to a minimum interval I_{min}. The rat progressed to the next stage of training once it learned to quickly reach and maintain the maximum insertion interval I_{max}. This required up to six daily sessions of interval training of 1-2 h each.

In general, I set $S_{\text{Lim}} = 4$ trials, $F_{\text{Lim}} = 3$ trials, $I_{\text{max}} = 6$ s, and $I_{\text{min}} = 0.5$ s. **Figure 3.15** shows how the distribution of trials across different intervals changed over four sessions for a representative rat. On the first day of interval training (i.e., Day 1) the rat had many trials with lower interval durations. On Day 4, nearly all trials were at the 6 s interval, indicating that the rat was ready to proceed to the next stage of training.

For most rats, setting $S_{\text{Lim}} = 4$ and $F_{\text{Lim}} = 3$ was sufficient to shift the distribution as depicted in **Figure 3.15**. However, a few rats appeared to game the system (whether intentionally or not) by inserting a failure every few trials so that N_S never reached S_{Lim}. This kept I_C low and effectively

increased the number of pellets received in a given time interval. For such rats, setting $S_{\text{Lim}} = 2$ and $F_{\text{Lim}} = 6$ or $F_{\text{Lim}} = 12$ made I_C rise quickly and fall slowly. This forced the rats to abandon their strategy to maximize pellets received.

3.3.4 Withdrawal Training Stage

The insertion interval training program released food pellets and triggered auditory stimuli concurrently, making it unclear which event reinforced the behavior. Therefore, the goal of the next stage of training was to decouple stimulus presentation from pellet release by making pellet release contingent on timely withdrawal from the nose-poke detector. The requested insertion interval remained fixed at 3 s across all trials. Successful maintenance of insertion for this interval triggered an auditory tone lasting 500 ms but no pellet release. Correct withdrawals (CWs), corresponding to successful detections, occurred within 500 ms of stimulus onset and resulted in reinforcement. Late withdrawals (LWs) more than 500 ms after stimulus onset represented failed detections and went unreinforced. Early withdrawals (EWs) before stimulus onset resulted in a 7-s timeout with the house light switched off and did not contribute to detection statistics.

Two metrics to measure the rat's overall performance were defined. The stimulation rate (SR) was the proportion of trials out of the total in which the rat was stimulated. The detection rate (DR) was the proportion of stimulated trials in which the rat correctly detected the stimulus. Mathematically,

$$\text{Stimulation Rate} = \frac{\text{CW} + \text{LW}}{\text{EW} + \text{CW} + \text{LW}}, \qquad (3.1)$$

$$\text{Detection Rate} = \frac{\text{CW}}{\text{CW} + \text{LW}}. \qquad (3.2)$$
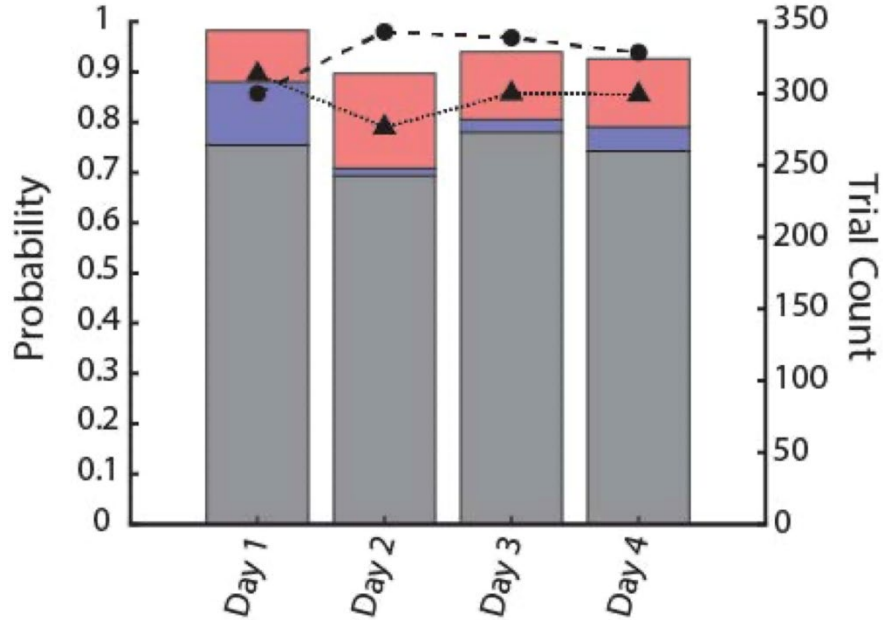
Figure 3.16: Withdrawal interval training data for a representative rat. Correct (black), late (blue), and early (red) withdrawals are shown, as well as stimulation rate (triangle markers) and detection rate (circle markers) time series.

The rat progressed to the main auditory detection task after achieving criterion on the withdrawal training task, i.e., DR ≥ 90% on two consecutive training days. This required up to five daily sessions lasting 1-2 h each. **Figure 3.16** shows representative withdrawal training data from a representative rat.

3.3.5 Auditory Detection Task

The main auditory detection task was identical to withdrawal training in all but one respect – instead of a fixed insertion interval across trials, insertion intervals were now randomized (3 ± 1.5 s, distributed uniformly). **Figure 3.17** summarizes the main behavioral task.

Consistent failure to achieve criterion resulted in disqualification. Additionally, the SR provided a measure of how efficiently the rat generated usable data – a low SR would indicate that few trials contributed to detection statistics, making the rat a poor candidate for MSE implantation even if the DR was high. Rats that achieved criterion on the main task with a sufficiently high SR ($SR \geq$
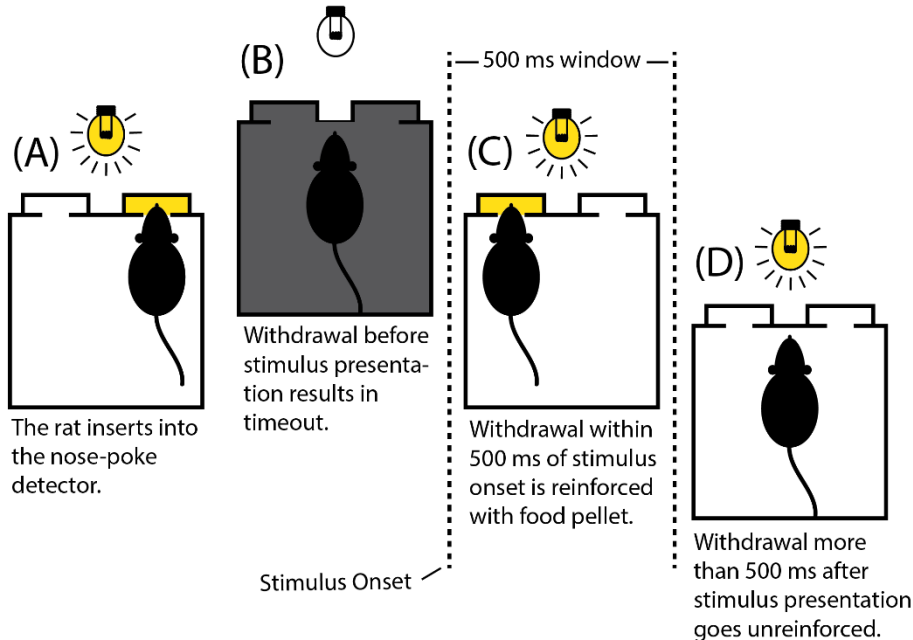
Figure 3.17: Schematic depiction of the behavioral task. **(A)** The rat must insert its snout into the nose-poke detector (right side) and maintain insertion uninterrupted until stimulus presentation. **(B)** Premature withdrawal results in a 7-s timeout during which the house light is extinguished. **(C)** Withdrawal within 500 ms of stimulus onset triggers the release of a food pellet (left side). **(D)** Withdrawal outside the 500-ms window results in a 3-s timeout without reinforcement.

70%; 3-4 daily sessions, 1-2 h each) proceeded to surgery after suspending food restriction and growing to 300+ g. **Figure 3.18** shows representative performance data for a representative rat on the auditory detection task.

3.4   Surgical Implantation of the Macro-Sieve Electrode

Rats underwent surgery to implant the MSE in the right sciatic nerve and mount the attached connector atop the skull in a dental acrylic head-cap. Construction of the head-cap included the use of a custom-designed cylindrical titanium chamber to enclose the Omnetics connector. The chamber's threaded outer walls accommodated the placement of a Delrin plastic (DuPont, Wilmington, DE, United States) screw cap to protect the Omnetics connector from damage or contamination when not in use (**Figure 3.19**).
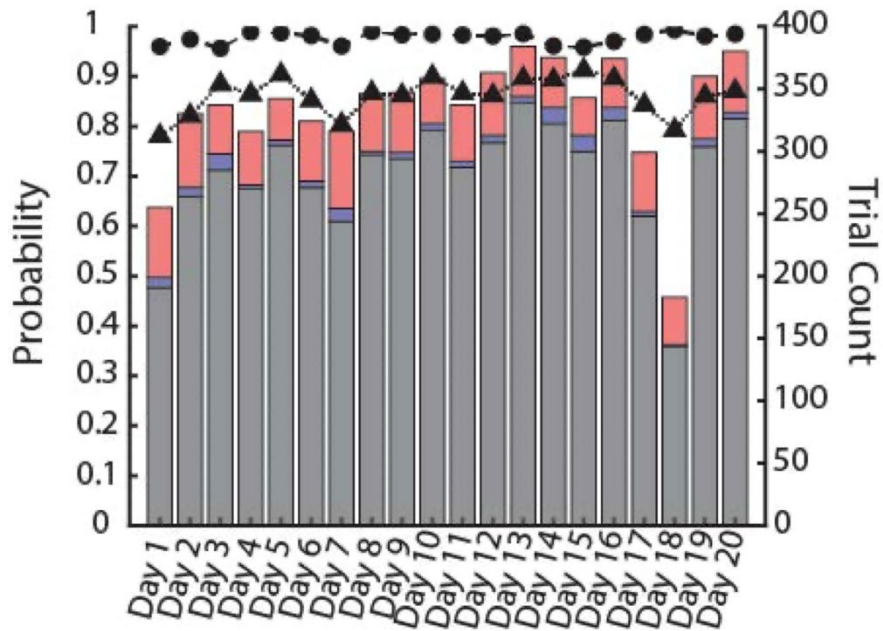
Figure 3.18: Auditory detection task data for a representative rat. Correct (black), late (blue), and early (red) withdrawals are shown, as well as stimulation rate (triangle markers) and detection rate (circle markers). The large number of training days despite reaching criterion early on is reflective of the fact that this particular rat's data was gathered at a time when the training protocol was not firmly established.
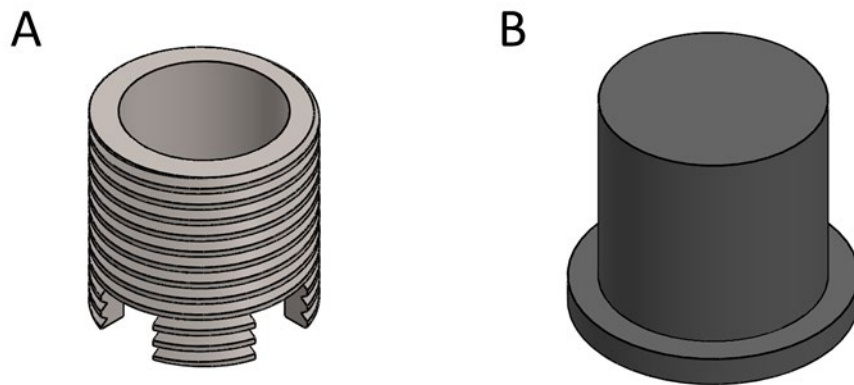
Figure 3.19: (A) Titanium chamber for enclosing Omnetics connector. **(B)** Protective Delrin screw cap to affix to the titanium chamber post-surgery when the rat was not performing the behavioral task.

A rat was eligible for surgery when it attained or exceeded a weight of 300 g. Aside from raising the odds of survival, waiting until the rat reached a certain level of maturity reduced the risk of head-cap failure due to skull elongation as the rat grew. **Table 3.10** lists materials to be assembled prior to surgery. All surgical instruments and implants were sterilized by ethylene oxide or autoclave in the days leading up to surgery.

The surgery proceeded as follows:

Initial Steps

Step 1:   Commence anesthetization with the administration of isoflurane (IH, 4% induction, 2% maintenance).

Step 2:   Inject the rat with an analgesic for post-operative pain mediation (buprenorphine SR, administered SC, 1.2 mg/kg).

Step 3:   Shave the right hind leg, back, and scalp. Sterilize by repeated applications of isopropyl alcohol and Betadine solution.

Step 4:   Apply artificial tears with a cotton-tipped swab to protect the rat's eyes from drying out during surgery.

Step 5:   Head-fix the rat in a stereotaxic frame equipped with a fitted nose cone for continued delivery of isoflurane and oxygen (**Figure 3.20**). It is advisable to elevate the rat a few inches above the base to keep its body level. This is possible with 2-3 slabs of Styrofoam. Ensure that the rat's head is firmly secured by the nose cone and ear bars, and that all adjustable knobs are closed tight.

Table 3.10: Materials required for surgery.

Item	Quantity	Seller(s)	Notes
Scalpel	1 unit	-	-
#10 Scalpel Blade	1 unit	-	-
Rat Tooth Tweezers	1 pair	-	-
Fine Tweezers	2 pairs	-	These must be in good condition. The tips must align.
Surgical Scissors	1 pair	-	These should be sharp enough to cut tissue in a single snip.
Long, Curved Tunneling Scissors	1 pair	-	These should be blunt-tipped.
Suture Driver	1 unit	-	For suturing skin and muscle with #4 nylon and #5 vicryl suture.
Micro-Suture Driver	1 unit	-	For suturing nerve into macro-sieve assembly's guidance conduits with #8 micro-suture.
0-80 1/8" Titanium Skull Screws	6 units	Allied Titanium	Part #0035962
#56 Micro Drill Bits	2 units	McMaster-Carr Amazon.com	-
Hand-Driven Pin Vise	2 units	Amazon.com	Manufactured by Migiwata.
Ball-End Driver Shaft	1 unit	McMaster-Carr	Part #6972A13
Titanium Chamber	1 unit	-	Custom-made at the medical school's machine shop.
Macro-Sieve Assembly	-	-	Wrapped in parafilm.
Saline bottle	1 unit	-	-
Cotton-tipped swabs	1-2 bags	-	-
Gauze	1-2 bags	-	-
Pipettes	2 units	-	-
Nylon 8-0 Micro-Suture threads	4-6 units	-	For suturing nerve to conduits.
4-0 Nylon Suture	-	-	For suturing skin incisions.
5-0 Vicryl Suture	-	-	For suturing muscle incisions.
Artificial Tears	-	-	For preventing the eyes from drying out.
Retractors	4 units	-	-
Retractor Plate	1 unit	-	-
UV Dental Lamp	1 unit	Amazon.com	-
Fusio Dental Acrylic	1-2 tubes	Henry Schein Inc.	Adheres to bone without the need for a separate bonding agent.
Flow-It Dental Acrylic	2-3 tubes	Henry Schein Inc.	Does not adhere to the bone.
Sterile Drapes	-	-	-
Sterile Gloves	-	-	-
Hydrogen Peroxide	-	-	-
Acetone	-	-	-
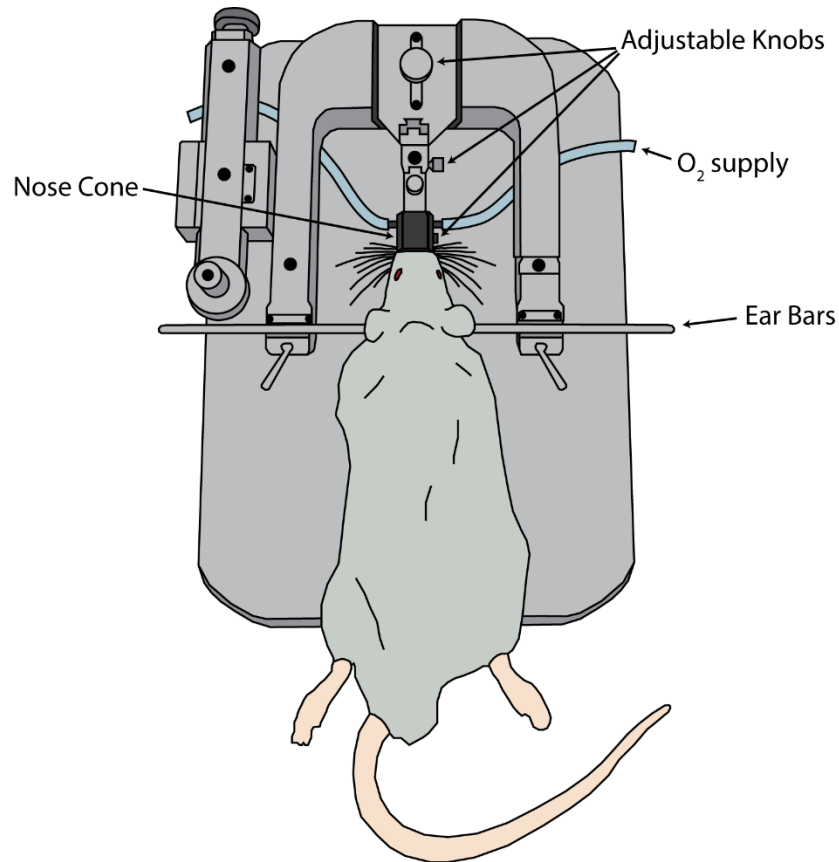
Figure 3.20: A rat head-fixed in the stereotaxic frame.

Exposing the Skull, Inserting Titanium Screws

Step 6: Expose the skull by making a sagittal incision along the midline using a #10 scalpel. Clean away blood and soft tissue by scraping the bone with the scalpel's blunt side and then scrubbing it with hydrogen peroxide. Cauterize persistent bleeding and clean the skull using a cotton-tipped swab lightly dipped in acetone (**Figure 3.21A**).

Step 7: Drill six holes in the skull using a #56 micro-drill set in a hand-driven pin vise. Apply gentle pressure only, so as not to penetrate into the cranium. Stop drilling as soon as the drill's rotation meets resistance from the bone's cancellous layer.
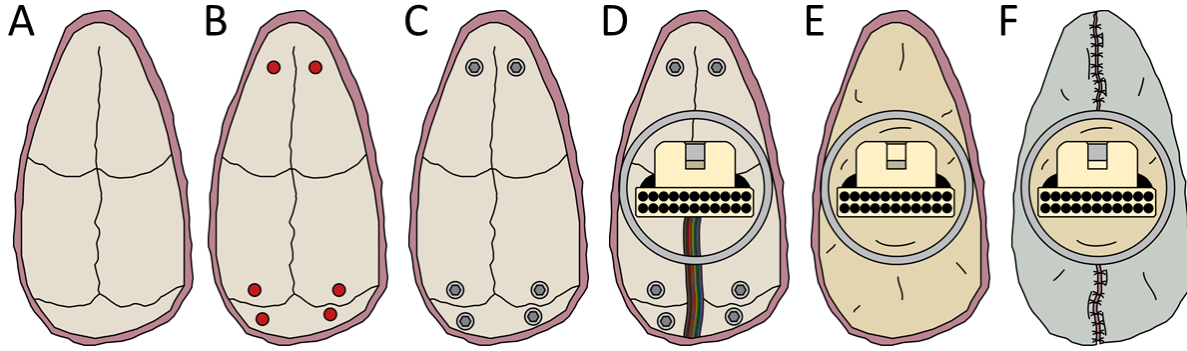
Figure 3.21: (A) The construction of the head-cap began with the exposure of the skull. **(B)** This was followed by the drilling of six holes and **(C)** driving of a 0-80 titanium hex screw into each of these holes. **(D)** Following MSE implantation in the right sciatic nerve, the attached Omnetics connector was routed subcutaneously to the skull and passed through the titanium chamber. It was positioned so that its latching mechanism rested well above the titanium chamber's upper rim. **(E)** The Omnetics connector and titanium chamber were cemented to the skull with dental acrylic. **(F)** The surrounding skin was sutured over the head-cap.

Placement of the holes should be such that they do not obstruct the placement of the titanium chamber and Omnetics wires (**Figure 3.21B**).

Step 8:   Use a ball-end driver shaft set in another hand-driven pin vise to drive a 0-80 titanium hex screw into each hole. The screws mechanically reinforce the head-cap's acrylic by anchoring it more firmly to the skull. Titanium is preferred over stainless steel due to its superior osseointegrative properties (**Figure 3.21C**).

Sciatic Nerve Exposure, Transection, MSE Implantation

Step 9:   Incise the skin along a line parallel to the femur and expose the sciatic nerve by a dorsolateral gluteal muscle-splitting incision and blunt dissection (**Figure 3.21B-C**).

Step 10:   Transect the sciatic nerve 5 mm proximal to the trifurcation.

Step 11:   Suture the nerve stumps into the MSE/Omnetics assembly's silicone guidance conduits using #8 micro-suture (**Figure 3.22**).

Step 12:   Create a subcutaneous tunnel between the leg and scalp incisions by separating the skin and fascia with a pair of blunt-tipped forceps.
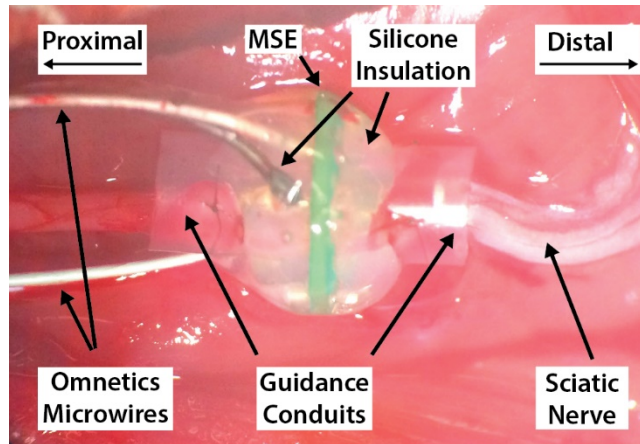
Figure 3.22: The implanted macro-sieve electrode.

Step 13: Pass the Omnetics connector through this tunnel up to the skull and place it within the confines of the protective titanium chamber (**Figure 3.21D**).

Building the Head Cap

Step 14: Ensure that the skull is <u>completely</u> dry. Wrap the stripped Omnetics wires (channels 7, 8, 9, and 10) securely around the titanium screws – these will provide a return path for monopolar stimuli. While wearing a pair of protective glasses, apply a base layer of Fusio dental acrylic to the skull. The Fusio should cover all exposed areas of the skull – the insulated Omnetics wires must not lie in direct contact with the skull. Ensure that all bright lights in the surgical station (including the microscope's lights) are switched off, as these will otherwise cure the Fusio prematurely. Allow the Fusio to set for 30 s, then cure with the handheld UV lamp for 30 s.

Step 15: Place the titanium chamber on top of the Fusio layer, while positioning the Omnetics connector within the chamber so that its latching mechanism lies wholly above the chamber's rim. This will ensure its availability during the behavioral task. Apply a layer of Flow-It dental acrylic on top of the Omnetics wires to secure them

in place and cure. (The Omnetics wires should be embedded between the Fusio and Flow-It layers. They must not lie in direct contact with the bone.)

Step 16: Gradually build up the head-cap with further additions of Flow-It. Take particular care to introduce Flow-It into the titanium chamber's interior via the 4 notches at its base. Do not apply too much at once, as this could interfere with curing.

Step 17: Ensure that all empty space between the Omnetics connector and titanium chamber's inner walls are filled with Flow-It and cure (it is best to do this in small increments). This prevents leakage of interstitial fluid from the skull and surrounding tissue, which can otherwise fill up the chamber and compromise the electrical isolation of the Omnetics channels from one another. The head-cap is now complete (**Figure 3.21E**).

End of Surgery, Post-Surgical Monitoring

Step 18: Having completed MSE implantation and head-cap construction, close all wounds with 5-0 vicryl suture for muscle incisions and 4-0 nylon suture for skin incisions (**Figure 3.21F**). Attach the Delrin screw cap to the titanium chamber.

Step 19: Release the rat from the stereotaxic frame and return it to its cage.

Step 20: Monitor the rat's condition every 10 minutes until it awakes from anesthesia.

Step 21: Place approximately $1/3^{rd}$ of the cage atop an electric heating pad to create a temperature gradient. This allows the rat to choose a comfortable temperature by selecting a point along the gradient to lie down.

Step 22: Monitor the rat for dehiscence daily for 7 days. Remove the sutures 7-10 days post-surgery.

Step 23: After allowing the rat to heal for 8-10 weeks, resume behavioral training.

3.5   Methods for Data Collection

3.5.1 Resumption of Auditory Training

Each rat resumed training with auditory stimuli 8-10 weeks following surgery. This time frame was assumed to be sufficient to allow for substantial regeneration of motor and sensory axons through the MSE's transit zones. Manual shaping was deemed unnecessary, and the rat's passage through the remaining stages of training was accelerated as they required as few as 2 days for interval training, 1 day for withdrawal training, and 3 days for the main auditory detection task to reach criterion.

3.5.2 Transferring Control to Electrical Stimuli

Having achieved criterion on the main auditory detection task, the rat was next trained on a go/no-go detection task with combined auditory and current stimuli that were presented synchronously. The commencement of experiments each day was preceded by *in vivo* measurement of channel impedances using TDT's Synapse Software Suite. The current stimuli were 500-ms, 50-Hz pulse trains with charge-balanced, biphasic (the leading and lagging phases each lasted 200 μs), rectangular pulses of a fixed amplitude chosen to induce a visible twitch response in the leg and foot without evident distress. Midway through each of these combined stimulus sessions (which were of 1-2 h duration), the auditory stimuli were suspended by pressing the handheld push button. This left the rat to be shaped solely by current stimuli. This training lasted 2-4 sessions, during which the rat the rat's DR for sole current simulation increased.

The rat next progressed to training only with fixed-intensity current stimuli – auditory stimuli were completely eliminated. Again, the intensity of the current stimulus was chosen to elicit a visible twitch response in the leg and foot without causing pain. The rat continued with daily sessions (1-

2 h each) until it reached criterion performance, at which point it proceeded to performing the detection task with variable stimuli based on MCS.

3.6 Methods for Data Analysis

3.6.1 The Method of Constant Stimuli

MCS entails the designation of a predefined list of K stimulus intensities, $\boldsymbol{x} = \{x_1, x_2, x_3, \ldots, x_K\}$, each of which must be applied a specified number of times, $\boldsymbol{n} = \{n_1, n_2, n_3, \ldots, n_K\}$. Each trial selects an intensity randomly and without replacement so that over the course of an experimental session the total number of trials is $N = \sum n_i$. If the number of correct detections for each intensity is $\boldsymbol{c} = \{c_1, c_2, c_3, \ldots, c_K\}$, then the proportion of correct trials is $\boldsymbol{y} = \{y_1, y_2, y_3, \ldots y_K\}$, where $y_i = c_i/n_i$. The 95% confidence interval for each proportion correct value can be calculated as $y_i \pm 1.96\sqrt{y_i(1 - y_i)/N}$.

For my behavioral study, the smallest amplitude in the predefined MCS list was always set to $I_{\min} = 0\ \mu\text{A}$ to enable direct measurement of how likely the rat was to withdraw within 500 ms of the prescribed interval's termination independent of any stimulus (i.e., the guess rate, γ). The largest amplitude, $I_{\max}$, was chosen based on the same criterion used for fixed-intensity sessions, i.e., the lowest level observed to elicit a visible twitch response in the leg without evident distress. The remaining amplitudes fell between these bounds.

Figure 3.23 shows the performance of a representative rat performing the behavioral task with current amplitudes chosen on the basis of MCS.
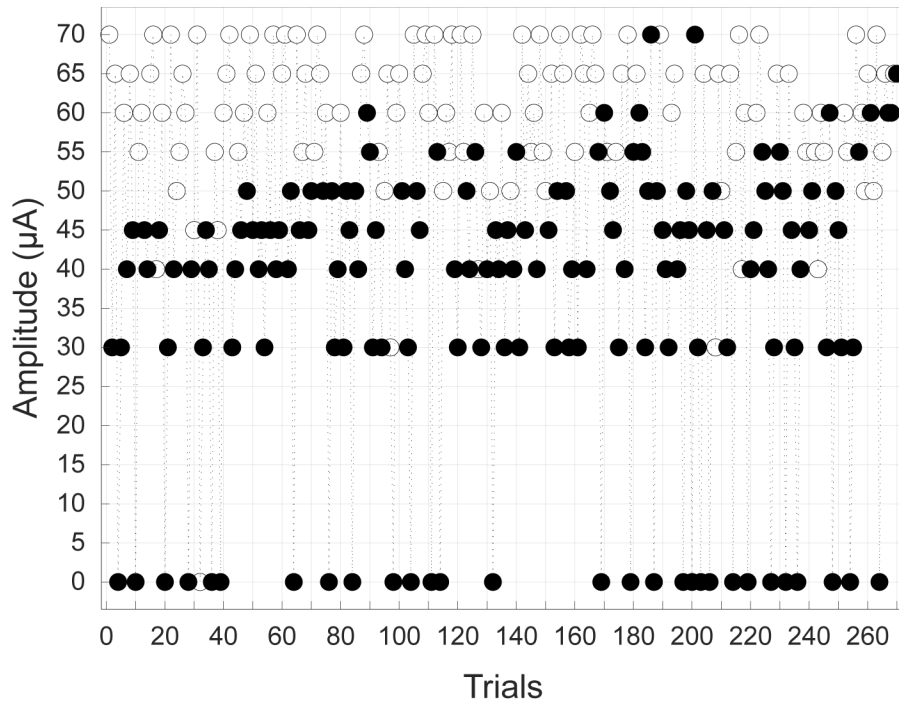
Figure 3.23: Representative performance of a rat stimulated with currents whose amplitudes varied according to MCS. Each dot represents a trial. Trials in which the rat successfully detected the stimulus (corresponding to correct withdrawals) are colored white. Trials in which the rat failed to detect the stimulus (corresponding to late withdrawals) are colored black. Maintenance trials and trials in which the rat withdrew early are not shown.

3.6.2 The Psychometric Function

The psychometric function $\psi = \psi(x)$ represents the probability of stimulus detection, ψ, as a function of stimulus intensity, x. Across a multitude of stimulus modalities and study designs, its shape consistently resembles a sigmoidal function. For an intuitive understanding of where this shape comes from, let us suppose that stimulus x triggers some level of "sensory evidence," or aggregate neural activity. Let us further suppose that due to noise, the mean sensory evidence produced by x is $\rho(x)$ and the variance is σ^2 so that the probability density function is $N(\rho(x), \sigma^2)$. Finally, let us suppose that there exists some threshold of sensory evidence T above which stimulus detection occurs. It follows that the probability of detecting the stimulus x is $\int_T^\infty N(\rho(x), \sigma^2) d\rho$, which is sigmoidal in shape (**Figure 3.24**).

96
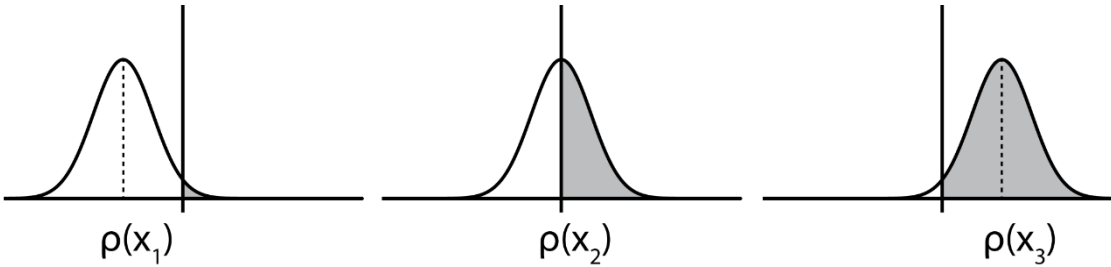
Figure 3.24: Qualitative demonstration of the basis for the psychometric function's sigmoidal shape. The horizontal line in each graph denotes the level of sensory evidence. The vertical line represents the threshold level of sensory evidence required for detection. The three Gaussians are probability density functions for how much sensory evidence is generated by stimuli of magnitudes x_1, x_2, and x_3. In each case, the area to the right of the threshold line is the probability of detection for that stimulus level.

The psychometric function is generalized as

$$\psi(x; \boldsymbol{\theta}) = \gamma + (1 - \gamma - \lambda)F(\alpha, \beta). \tag{3.3}$$

The parameter vector $\boldsymbol{\theta}$ is a collection of four parameters $\{\alpha, \beta, \gamma, \lambda\}$. As explained by Wichmann and Hill (2001a), the "guess rate" γ is the base rate of performance in the absence of the stimulus. The "lapse rate" λ reflects the rate at which the observer responds incorrectly regardless of stimulus intensity. These two parameters are of secondary scientific interest as they arise from processes independent of the underlying detection mechanism, represented by the "driving function" $F(\alpha, \beta)$. Although the precise interpretation of α and β depends on the formulation of the driving function, in general α determines its displacement along the abscissa while β determines its slope. Prins (2016) lists numerous formulations for $F(\alpha, \beta)$. These are reproduced in **Table 3.11**.

Table 3.11: Various formulations of the driving function $F(x; \alpha, \beta)$ as described by Prins (2016).

Function Name	Formulation of $F(x; \alpha, \beta)$	Notes
Cumulative Normal Distribution	$\dfrac{\beta}{2\pi} \displaystyle\int_{-\infty}^{x} \exp\left(-\dfrac{\beta^2(x-\alpha)^2}{2}\right) dx$	This is the most justifiable form of $F_N(x; \alpha, \beta)$ if one assumes that the noise underlying the variability of sensory evidence arises from independent and alike sources, i.e., is normally distributed.
Logistic	$\dfrac{1}{1 + \exp\left(-\beta(x-\alpha)\right)}$	This is a close approximation of the cumulative normal distribution, with the advantage that its calculation does not rely on solving a closed form integral. $F_L(x = \alpha) = 1/2$. Since $F_L(x = 0) \neq 0$, this formulation is unsuitable for experiments where $x = 0$ denotes an absence of stimulus.
Weibull	$1 - \exp\left(-\left(\dfrac{x}{\alpha}\right)^\beta\right)$	$F_W(x = \alpha) = 1 - 1/e = 0.6321$. The parameter β determines the slope together with α. Since $F_W(x = 0) = 0$, this formulation is suitable for experiments where $x = 0$ corresponds to an absence of stimulus.
Gumbel	$1 - \exp\left(-10^{(\beta(x-\alpha))}\right)$	This is the logarithmic analog of the Weibull function, i.e., it is suited to experiments where stimulus intensities are logarithmically distributed.
Quick	$1 - 2^{\left(-\left(\frac{x}{\alpha}\right)^\beta\right)}$	This closely resembles the Weibull function except in its use of 2 instead of e as its base. Since $F_Q(x = \alpha) = 1 - 1/2 = 0.5$, this formulation is suited to experiments where the 50% detection threshold is of interest. Here, too, do the parameters α and β determine the slope.
Log-Quick	$1 - 2^{\left(-10^{(\beta(x-\alpha))}\right)}$	This is the logarithmic analog of the Quick function.
Hyperbolic Secant	$\dfrac{2}{\pi} \tan^{-1} \exp\left(\dfrac{\pi}{2}\beta(x-\alpha)\right)$	This is rarely encountered in the psychometrics literature.

I chose the Quick function because of its implicit relationship with the 50% detection threshold, and because in my experiments $x = 0$ corresponds to a trial with no stimulus, which for an ideal observer should correspond to a DR of 0%. Thus, the psychometric function took the form

$$\psi(x; \boldsymbol{\theta}) = \gamma + (1 - \gamma - \lambda)\left(1 - 2^{\left(-\left(\frac{x}{\alpha}\right)^\beta\right)}\right). \tag{3.4}$$

3.6.3 Fitting the Psychometric Function to the Data

For each amplitude x_i, MCS provides an associated number of trials n_i and proportion of correct detections y_i. Assume that each trial has two possible outcomes – detect or do not detect. Further

assume that each trial is independent of all other trials, so that the probability of correct detection is fixed at $\psi(x_i, \boldsymbol{\theta})$. It follows that the likelihood of obtaining this particular value for y_i is

$$L_i(\theta) = \binom{n_i}{n_i y_i} [\psi(x_i; \boldsymbol{\theta})]^{n_i y_i} [1 - \psi(x_i; \boldsymbol{\theta})]^{n_i(1-y_i)}. \tag{3.5}$$

The joint likelihood of obtaining all of the values in $\boldsymbol{y}$ would then be

$$L(\boldsymbol{\theta}) = \prod_{i=1}^{K} \binom{n_i}{n_i y_i} [\psi(x_i; \boldsymbol{\theta})]^{n_i y_i} [1 - \psi(x_i; \boldsymbol{\theta})]^{n_i(1-y_i)}. \tag{3.6}$$

The "best" fit for the psychometric function is provided by the parameter vector $\hat{\theta}$ that maximizes the joint likelihood,

$$\hat{\boldsymbol{\theta}} = \arg \max_{\boldsymbol{\theta}} L(\boldsymbol{\theta}). \tag{3.7}$$

Matters are simplified by taking the logarithm of **Equation (3.6)** to obtain the following expression for the log-likelihood:

$$l(\boldsymbol{\theta}) = \sum_{i=1}^{K} \left(\log \binom{n_i}{n_i y_i} + n_i y_i \log \psi(x_i; \boldsymbol{\theta}) + n_i(1 - y_i) \log[1 - \psi(x_i; \boldsymbol{\theta})] \right). \tag{3.8}$$

Computationally, the calculation of $\binom{n_i}{n_i y_i}$ quickly becomes untenable as n_i grows larger. Fortunately, this term's independence of $\boldsymbol{\theta}$ allows its removal without impacting the calculation of $\hat{\boldsymbol{\theta}}$. The maximization problem is thus reduced to

$$\widehat{\boldsymbol{\theta}} = \arg\max_{\boldsymbol{\theta}}(n_i y_i \log \psi(x_i; \boldsymbol{\theta}) + n_i(1 - y_i) \log[1 - \psi(x_i; \boldsymbol{\theta})]) . \tag{3.9}$$

I used the Nelder-Mead simplex algorithm to minimize the negative log-likelihood function and find the optimum $\widehat{\boldsymbol{\theta}}$. For a given function of n variables, this algorithm creates a simplex with $(n + 1)$ vertices in n-dimensional space. At each iteration, it evaluates the function at each vertex and uses a set of rules to replace the highest-valued vertex with a new one. Eventually, all simplex vertices converge to a specific point corresponding to a set of values that minimize the function locally. Describing these rules falls outside the scope of this dissertation. However, they are explained in detail in Nelder and Mead (1965).

In practice, the optimization of $\widehat{\boldsymbol{\theta}}$ was subject to some boundary conditions. First, the guess rate γ was fixed to the empirically measured value $\gamma = y|_{x=0}$. Second, in keeping with the recommendation of Wichmann and Hill (2001a), the lapse rate λ was constrained to fall between 0 and 0.05. I used a bounded version of MATLAB's `fminsearch` function (which implements Nelder-Mead) to minimize the negative log-likelihood function and find the optimum $\widehat{\boldsymbol{\theta}}$ subject to these boundary conditions (D'Errico, 2021).

Having fitted the psychometric function to the empirical data, the detection threshold x_T and slope $\psi'(x_T; \widehat{\boldsymbol{\theta}})$ were calculated by taking the inverse and derivative of (3.4), respectively:

$$x_T = \alpha \left[\log_2 \left(\frac{1 - \gamma - \lambda}{0.5 - \lambda} \right) \right]^{\frac{1}{\beta}}, \tag{3.10}$$

$$\psi'(x_T; \widehat{\boldsymbol{\theta}}) = (1 - \gamma - \lambda) \cdot \ln 2 \cdot \left(\frac{\beta}{\alpha} \right) \left(\frac{x_T}{\alpha} \right)^{\beta - 1} \cdot 2^{\left(-\left(\frac{x_T}{\alpha} \right)^\beta \right)}. \tag{3.11}$$
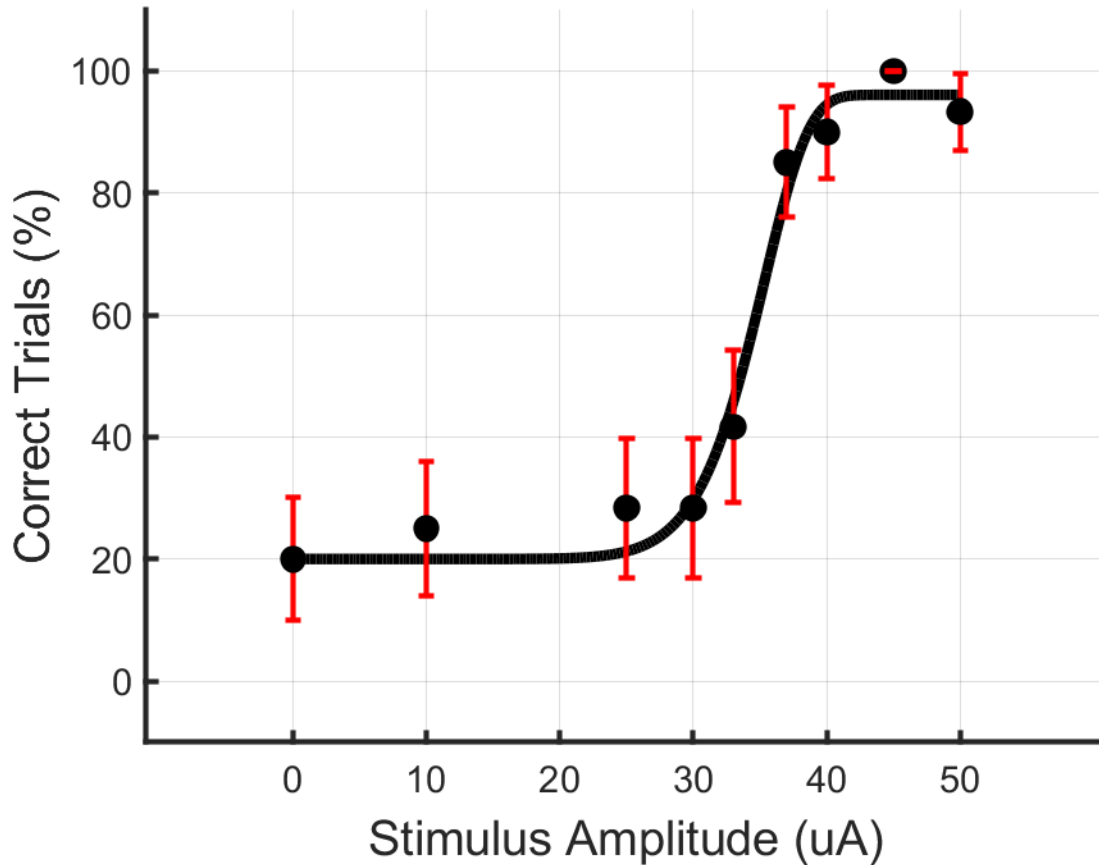
Figure 3.25: A psychometric curve fitted to the simulated performance of a hypothetical rat. The rat's generating function had parameters $\alpha = 35$ μA, $\beta = 10$, $\gamma = 20\%$, and $\lambda = 1\%$, corresponding to a 50% detection threshold of 33.72 μA and a slope of 6.94 μA^{-1}. The rat was stimulated 60 times each at current amplitudes of 0, 10, 25, 30, 33, 37, 40, 45, and 50 μA. Through maximum likelihood estimation, fitted parameters were $\alpha = 34.50$ μA, $\beta = 11.60$, $\gamma = 20\%$ (recall that this was held fixed), and $\lambda = 3.92$ %. These corresponded to a 50% detection threshold of 33.55 μA and a slope of 7.98 μA^{-1}. Error bars represent 95% confidence intervals calculated for binomial distributions based on detection probabilities, calculated as $y_i \pm 1.96\sqrt{y_i(1 - y_i)/N}$.

For illustration, **Figure 3.25** shows a psychometric curve fitted to the simulated performance data of a hypothetical rat.

3.6.4 Assessing Goodness of Fit

Goodness of fit measures the discrepancy between a model's predicted values and the empirical data. Recall that $\widehat{\theta}$ denotes the parameter vector returned by the fitting routine described in the previous section. By the definition of maximum likelihood estimation, it follows that $L(\widehat{\theta}) \geq$

$L(\boldsymbol{\theta}) \, \forall \, \boldsymbol{\theta}$. Suppose there exists some goodness of fit metric Z. A desirable property for assessing $\widehat{\boldsymbol{\theta}}$'s goodness of fit would be

$$Z(\widehat{\boldsymbol{\theta}}) \geq Z(\boldsymbol{\theta}) \, \forall \, \boldsymbol{\theta}. \tag{3.12}$$

Wichmann and Hill (2001a) advocate the use of the deviance metric D, defined as

$$D(\widehat{\boldsymbol{\theta}}) = 2 \log \left[\frac{L(\boldsymbol{\theta}_{\max}; \boldsymbol{y})}{L(\widehat{\boldsymbol{\theta}}; \boldsymbol{y})} \right] = 2 \left[l(\boldsymbol{\theta}_{\max}; \boldsymbol{y}) - l(\widehat{\boldsymbol{\theta}}; \boldsymbol{y}) \right] \tag{3.13}$$

$$D(\widehat{\boldsymbol{\theta}}) = 2 \sum_{i=1}^{K} \left\{ n_i y_i \log \left(\frac{y_i}{\psi(x_i; \boldsymbol{\theta})} \right) + n_i (1 - y_i) \left(\frac{1 - y_i}{1 - \psi(x_i; \boldsymbol{\theta})} \right) \right\}. \tag{3.14}$$

Here, $\boldsymbol{\theta}_{\max}$ is the saturated solution, i.e., the model with no residual error whose log-likelihood is found by substituting y_i for $\psi(x_i; \widehat{\boldsymbol{\theta}})$ in **Equation (3.8)**. By definition, $l(\boldsymbol{\theta}_{\max}; \boldsymbol{y})$ is independent of $\widehat{\boldsymbol{\theta}}$. Since $l(\widehat{\boldsymbol{\theta}}; \boldsymbol{y}) \geq l(\boldsymbol{\theta}; \boldsymbol{y}) \, \forall \, \boldsymbol{\theta}$, this means that

$$2 \left[l(\boldsymbol{\theta}_{\max}; \boldsymbol{y}) - l(\widehat{\boldsymbol{\theta}}; \boldsymbol{y}) \right] \leq 2 [l(\boldsymbol{\theta}_{\max}; \boldsymbol{y}) - l(\boldsymbol{\theta}; \boldsymbol{y})] \, \forall \, \boldsymbol{\theta}, \tag{3.15}$$

$$\text{or} \quad D(\widehat{\boldsymbol{\theta}}) \leq D(\boldsymbol{\theta}) \, \forall \, \boldsymbol{\theta}. \tag{3.16}$$

Thus, despite the change in the comparison operator's direction, the deviance metric satisfies the condition laid out in **Equation (3.12)**.

For large datasets, calculated deviance values may be compared with the appropriate χ^2 distribution to assess the goodness of fit. However, for smaller datasets such as those obtained through the behavioral experiments described in this text, this does not work. Wichmann and Hill
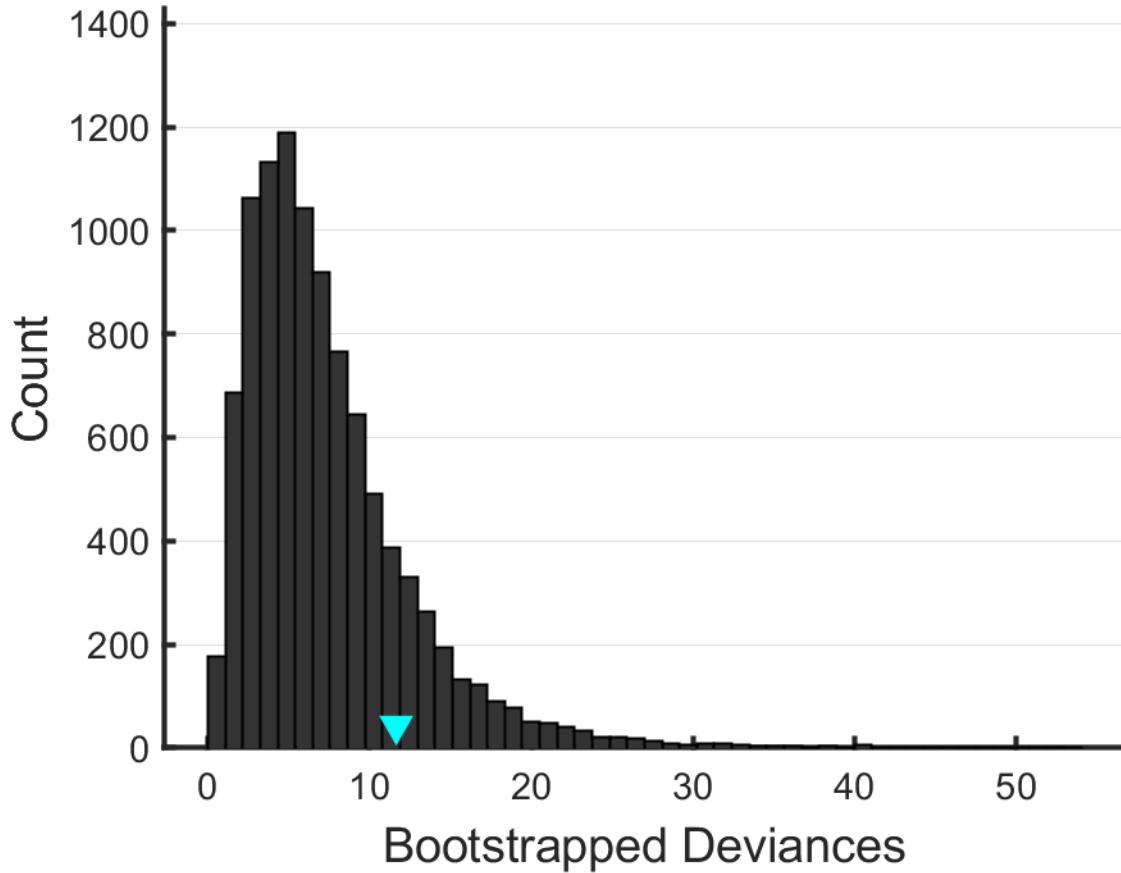
Figure 3.26: The hypothetical rat's fitted deviance value was 11.67, which was greater than 84.16% of bootstrapped deviance values (i.e., pDev = 0.84).

(2001a) advocate the use of the Monte Carlo bootstrap, a computer-based method for generating measures of accuracy for statistical estimates (Efron and Tibshirani, 1993).

Accordingly, I used the empirically derived psychometric model $\psi(x;\widehat{\boldsymbol{\theta}})$ as a generating function for $B = 10{,}000$ simulated datasets $\boldsymbol{y}^*$ with the same stimulus amplitude distribution $\{\boldsymbol{x}, \boldsymbol{n}\}$ (this was equivalent to sampling trial outcomes with replacement for each amplitude). For each simulation, I performed maximum likelihood fitting of the simulated dataset to obtain the model $\psi(x;\widehat{\boldsymbol{\theta}}^*)$ and calculated the deviance $D(\widehat{\boldsymbol{\theta}}^*)$. $\psi(x;\widehat{\boldsymbol{\theta}})$ was considered a poor fit if $\widehat{D} = D(\widehat{\boldsymbol{\theta}})$

exceeded the 95th percentile of the simulated deviance distribution D^*, i.e., $\widehat{D} > D^{*(0.95)}$ (Wichmann and Hill, 2001a) (**Figure 3.26**).

Goodness of fit was improved by identifying and removing outliers using the jackknife resampling technique (Wichmann and Hill, 2001a) and then recalculating $\widehat{\boldsymbol{\theta}}$. For a dataset $\boldsymbol{x}$ with K amplitudes, the ith jackknife dataset $\boldsymbol{x}_{(-i)}$ was derived by removing the ith amplitude x_i. Calculation of parameter vectors $\widehat{\boldsymbol{\theta}}_{(-1)}$, $\widehat{\boldsymbol{\theta}}_{(-2)}$, … $\widehat{\boldsymbol{\theta}}_{(-K)}$ by maximum likelihood estimation preceded the computation of deviances $D_{(-1)}$, $D_{(-2)}$, … $D_{(-K)}$. The ith amplitude x_i was identified as an outlier if the corresponding reduction in deviance satisfied $D(\widehat{\boldsymbol{\theta}}) - D_{(-i)} > 6.63$.

3.6.5 Calculating Confidence Intervals

As noted by Wichmann and Hill (2001b), the comparison of thresholds and slopes across different experimental conditions (such as stimulus configuration) is contingent on measures of their variability. This variability depends on the number of trials and their distribution along the stimulus axis. One approach to calculating threshold and slope variability would be to obtain error estimates for fitted parameters $\widehat{\boldsymbol{\theta}}$. However, this would require hundreds of trials for each datapoint – a criterion not met by my behavioral experiments.

In accordance with Wichmann and Hill (2001b), I used the $B = 10,000$ bootstrapped parameter vectors $\widehat{\boldsymbol{\theta}}^*$ to generate distributions for x_T^* and $\psi'(x_T^*; \widehat{\boldsymbol{\theta}}^*)$. I then calculated bias-corrected and accelerated (BCa) 95% confidence intervals (CI95) for these distributions. This allowed me to correct for bias and skewness in my bootstrapped distributions. If a distribution skewed negatively, the BCa CI95 boundaries shifted leftwards. Similarly, if the distribution skewed positively, the BCa CI95 boundaries shifted to the right.

A detailed explanation of the BC_a calculation can be found in Efron and Tibshirani's *Introduction to the Bootstrap* (1993). To summarize, the ϵ-level BC_a confidence interval endpoint for some estimated parameter $\hat{\rho}$ is calculated as

$$\hat{\rho}_{BC_a}(\epsilon) = \hat{G}^{-1}\left(\Phi\left(\hat{z}_0 + \frac{\hat{z}_0 + z^{(\epsilon)}}{1 - \hat{a}(\hat{z}_0 + z^{(\epsilon)})}\right)\right). \tag{3.17}$$

Here, $\hat{G}^{-1}$ is the inverse cumulative distribution function of the bootstrapped estimates' distribution $\hat{\rho}^*$, CG is the standard normal cumulative distribution function (e.g., $\Phi(0) = 0.5$), and $z^{(\epsilon)}$ is the $(100 \cdot \epsilon)$th percentile of the standard normal distribution (e.g., $z^{(0.5)} = 0$; $z^{(0.95)} = 1.645$). The bias-correction term $\hat{z}_0$ reflects the proportion of bootstrapped $\hat{\rho}^*$-values that fall below the observed statistic $\hat{\rho}$. It is calculated using the formula

$$\hat{z}_0 = \Phi^{-1}\left(\frac{\#\{\hat{\rho}^*(b) < \hat{\rho}\}}{B}\right). \tag{3.18}$$

Here, B is the number of bootstrap simulations, $\#\{\hat{\rho}^*(b) < \hat{\rho}\}$ is the number of bootstrapped estimates that fall below the observed statistic, and Φ^{-1} is the inverse of the standard normal cumulative distribution function (e.g., $\Phi^{-1}(0.95) = 1.645$).

The acceleration term $\hat{a}$ (see **Equation (3.17)**) measures the skewness of the bootstrapped distribution. Its calculation relies on a jackknife similar to the one used to identify outliers. As before, let $x_{(-i)}$ represent the ith jackknife dataset with the ith observed datapoint removed. Let $\hat{\rho}_{(-i)}$ be the corresponding jackknife parameter estimate. Define $\hat{\rho}_{(\bullet)} = \sum_{i=1}^{K} \hat{\rho}_{(-i)}/K$. The acceleration term may be calculated as

$$\hat{a} = \frac{\sum_{i=1}^{K}\left(\hat{\rho}_{(\cdot)} - \hat{\rho}_{(-i)}\right)^{3}}{6\left\{\sum_{i=1}^{K}\left(\hat{\rho}_{(\cdot)} - \hat{\rho}_{(-i)}\right)^{2}\right\}^{3/2}} \,. \tag{3.19}$$

Thus, the procedure I used for calculating the bias-corrected and accelerated 95% confidence interval for x_T was as follows:

Step 1: Perform $B = 10{,}000$ bootstraps using $\psi(x; \widehat{\boldsymbol{\theta}})$ as the generating function. For each bootstrapped session, perform maximum likelihood estimation to obtain $\widehat{\boldsymbol{\theta}}^{*}$ and calculate x_T^{*}.

Step 2: Calculate $\hat{z}_0$ by counting how many bootstrapped estimates of x_T^{*} fall below the observed x_T and applying **Equation (3.18)**.

Step 3: For each jackknifed set of amplitudes $x_{(-i)}$, perform maximum likelihood estimation to obtain corresponding parameter vectors $\widehat{\boldsymbol{\theta}}_{(-i)}$. Use these to calculate $\hat{x}_{T(-i)}$ and then apply **Equation (3.19)** for the calculation of $\hat{a}$.

Step 4: The corresponding ϵ-values for 95% confidence intervals are $0.5 \pm 0.95/2$, i.e., 97.5 and 2.5. $z^{(0.975)} = 1.96$. $z^{(0.025)} = -1.96$.

Step 5: Calculate $\hat{z}_0 + \frac{\hat{z}_0 + z^{(\epsilon)}}{1 - \hat{a}(\hat{z}_0 + z^{(\epsilon)})}$ for each ϵ-value and plug it into CG to obtain a corrected percentile.

Step 6: Apply G^{-1} by looking up the corrected percentile for each ϵ-value in the distribution of x_T^{*}.
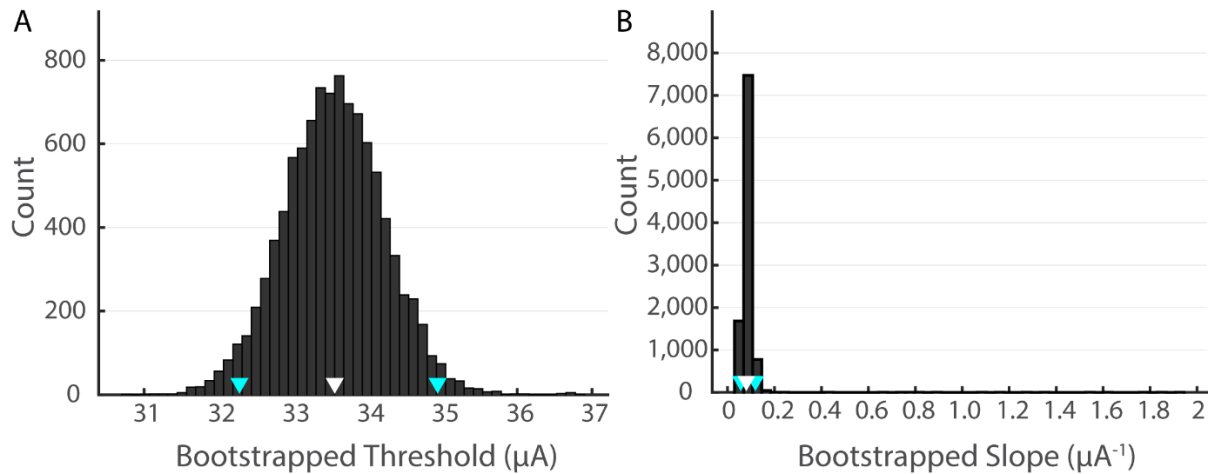
Figure 3.27: The hypothetical rat's 95% BC_a confidence intervals for threshold and slope are indicated by the blue arrows overlaid atop the histograms. For threshold, the lower and upper bounds were 32.27 µA and 34.93 µA, respectively (for a fitted value of 33.55 µA). For slope, the lower and upper bounds were 5.62 $µA^{-1}$ and 11.84 $µA^{-1}$ respectively (for a fitted value of 7.98 $µA^{-1}$).

This concludes my description of the experimental apparatus, equipment assembly, training protocols, mode of data collection, and subsequent analysis of the data. The subsequent chapters describe my application of these methods to four rats, details the results of my efforts, and discuss the implications of these results.

Chapter 4: Results and Discussion

The CRSNB model was applied to four rats (Rats A, B, C, and D) over a two-year period. This chapter gives a detailed account of the data collection, the subsequent generation of psychometric curves, and the extraction of thresholds and slopes.

4.1 Collecting the Data

Following their arrival in the laboratory, each rat adhered to a schedule of training and surgery in preparation for the main detection task with variable electrical stimuli. Briefly, after an initial period of acclimation and manual shaping to the food magazine and nose-poke detector, the rats were trained with auditory stimuli in three phases. First, the rats learned to insert their snouts into the nose-poke detector for progressively longer intervals (interval training). Second, the rats learned to withdraw from the nose-poke detector upon stimulus onset that occurred after a fixed 3-s insertion interval (withdrawal training). Third, the insertion interval was randomized uniformly between 1.5-4.5 s (main auditory detection task).

Having completed auditory training and attained 300 g, the rats underwent surgical implantation of the macro-sieve assembly in the right sciatic nerve and accompanying construction of a head-cap for awake interfacing with an external stimulator. After healing for 8-10 weeks, the rats returned to training with auditory stimuli and progressed once more through interval training, withdrawal training, and the detection task. They next underwent a period of transition whose goal was to transfer their attention from auditory to electrical stimuli. Once this transfer was complete, the rats trained with purely electrical stimuli of fixed amplitude. Finally, they performed the detection task with electrical stimuli that varied in amplitude. **Table 4.1** shows the sequence in

Table 4.1: Sequence of training, surgery, and data collection for Rats A, B, C, and D. In the leftmost column, letters in parenthesis denote the following: A – auditory stimuli; C – combined stimuli; E – electrical stimuli; F – fixed amplitude; V – variable amplitudes.

	Rat A		Rat B		Rat C		Rat D	
	Start	End	Start	End	Start	End	Start	End
Interval Training (A)	11/19/18	11/28/18	11/19/18	11/28/18	11/19/18	11/28/18	6/8/20	6/12/20
Withdrawal Training (A)	11/29/18	12/5/18	11/29/18	12/5/18	11/29/18	12/5/18	6/16/20	6/23/20
Detection (A)	12/11/18	12/14/18	12/11/18	12/14/18	12/11/18	12/14/18	6/24/20	6/29/20
Surgery	3/14/19		3/15/19		4/9/19		7/15/20	
Interval Training (A)	5/20/19	5/21/19	5/20/19	5/21/19	6/18/19	6/25/19	9/14/20	9/16/20
Withdrawal Training (A)	5/22/19	5/22/19	5/22/19	5/22/19	6/26/19	6/27/19	9/17/20	9/17/20
Detection (A)	5/23/19	5/28/19	5/23/19	5/28/29	6/28/19	7/3/19	9/18/20	9/22/20
Transition (C, F)	6/11/19	6/28/19	6/11/19	6/28/19	7/4/19	7/8/19	9/23/20	9/23/20
Detection (E, F)	7/1/19	7/4/19	7/1/19	7/4/19	7/9/19	7/9/19	9/24/20	9/26/20
Detection (E, V)	7/5/19	9/10/19	7/11/19	7/29/19	7/10/19	10/5/19	9/29/20	11/19/20

which Rats A, B, C, and D were trained on the behavioral task, underwent surgery, and generated data for subsequent analysis.

4.1.1 Rats A, B, and C

Rats A, B, and C arrived in the laboratory in early November 2018 aged roughly five weeks. Following an initial period of acclimation and hand-shaping, they each commenced training with auditory stimuli on 11/19/2018 and concluded this training on 12/11/2018. Surgery was delayed to allow the rats to attain 300 g, and also due to the unavailability of viable macro-sieve assemblies for implantation. Thus, Rat A underwent surgery on 3/14/2019, Rat B the following day on 3/15/2019, and Rat C on 4/9/2019.

Rats A and B

After approximately 10 weeks' healing, Rats A and B resumed training with auditory stimuli on 5/20/2019. Rat A reached criterion on the auditory detection task after just eight days, on 5/28/2019. Although Rat B did not strictly reach criterion on this date, its DR was close enough to 90% that I decided to introduce both rats to electrical stimulation on the same schedule.

Initial attempts to pass electric currents into the rats' sciatic nerves met with difficulty. Each experimental day began with repeated *in vivo* measurements of MSE channel impedances using TDT's Synapse Software Suite. Channel impedances varied widely across measurements, and manual triggering of current stimuli produced visible muscle twitches only intermittently. This was eventually attributed to the leakage of interstitial fluid from tissue surrounding the head-cap's base into the titanium chamber. Currents from the IZ2H stimulus isolator entered the skull-mounted Omnetics connector via the commutator assembly, passed through the interstitial fluid to GND, and bypassed the Omnetics microwires and MSE altogether. The solution was to remove gathered interstitial fluid from the titanium chamber with a cotton-tipped swab and use quick bursts from a compressed air cannister to dry the Omnetics connector completely. Only when subsequent impedance measurements yielded consistent values did the experiment proceed. Care also was taken in subsequent surgeries to ensure that all gaps in the head-cap's dental acrylic were fully sealed.

Rats A and B resumed training on 6/11/2019. At this time, I was uncertain of how best to induce the transfer of attention from auditory to electrical stimuli. On the first day, I subjected the rats to repeated training sessions in which I pressed the handheld push-button every few minutes to switch between combined stimuli (i.e., auditory and electrical stimuli presented synchronously) and electrical stimulation alone. Failure to produce immediate results led to this strategy's premature abandonment. I spent the next two weeks attempting to repeat the entire training sequence (i.e., interval training, withdrawal training, detection task) with auditory stimuli supplanted by electrical stimuli. This approach was unsuccessful. Although both rats performed well on interval training, their poor performance on the withdrawal task indicated a lack of attention transfer.
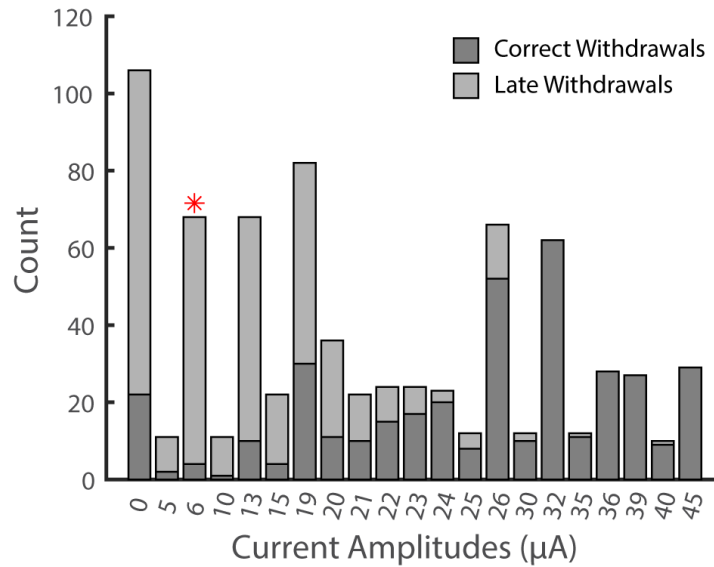
Figure 4.1: Breakdown of trials by current amplitude as performed by Rat A for the multi-channel stimulus configuration under MCS (maintenance trials excluded). The red star above current amplitude 6 µA indicates that the rat's performance at this datapoint was deemed an outlier during curve fitting (see **Section 3.6.4**) and excluded from subsequent analysis.

On 6/25/2019, Rats A and B returned to training with combined stimuli. For four days, the rats trained in daily sessions lasting 1-2 hours. Midway through each session, I pressed the handheld push-button once to toggle from combined stimuli to electrical stimulation alone. At the end of this four-day period, Rat A had achieved criterion. Rat B had not. My desire to keep the rats on the same training schedule led me to graduate both to pure electrical stimulation with fixed amplitude.

Rat A reached criterion with fixed amplitude quickly, and on 7/5/2019 progressed to electrical stimuli with variable amplitudes based on the method of constant stimuli (MCS). Over the next 24 days (i.e., 114-138 days post-implantation), it performed 11 sessions of the detection task for the multi-channel stimulus configuration. Data from 9 of these sessions were collated for psychometric analysis. The histogram in **Figure 4.1** provides a breakdown of trials by current amplitude. This
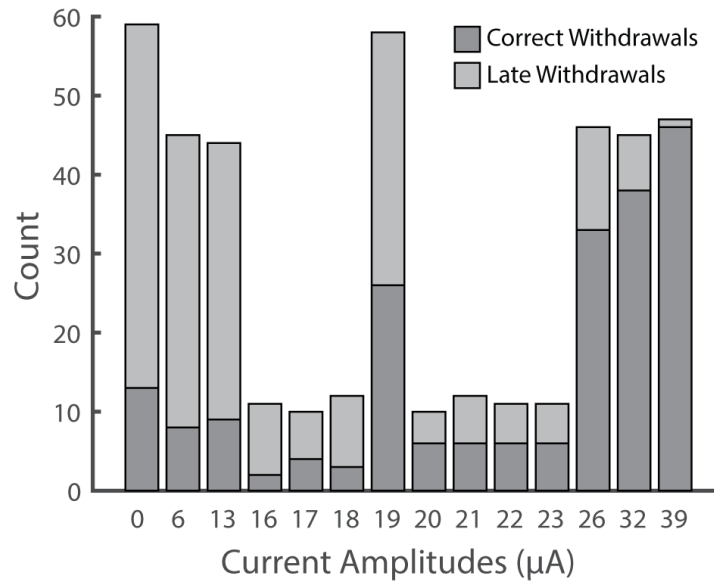
Figure 4.2: Breakdown of trials by current amplitudes as performed by Rat B for the multi-channel stimulus configuration under MCS (maintenance trials excluded).

was followed by a 1-month hiatus. Sporadic attempts to resume data collection between 8/26/2019 and 9/10/2019 were dropped due to the rat's waning performance.

Rat B progressed to variable amplitudes (MCS) on 7/11/2019. It performed six of these sessions through 7/29/2019. Five sessions' data (gathered during 119-126 days post-implantation) were collated for psychometric analysis (**Figure 4.2**).

Rat C

Rat C resumed training with auditory stimuli on 6/18/2019, roughly 10 weeks after surgery. Auditory retraining concluded on 7/3/2019 and was followed by a four-day transition period – much had been learned from the training of Rats A and B a few weeks earlier. After one day of performing the detection task with fixed amplitude electrical stimuli (the two-day standard criterion was relaxed due to the rat's superlative DR), the rat progressed to variable amplitudes for both multi-channel and single-channel configurations. Single-channel stimulation by channel C3 elicited no leg-twitch or behavioral response up to 200 μA, precluding data collection for this channel. **Table 4.2** summarizes the sequence of data collection for Rat C. Trial breakdowns for each stimulus configuration under MCS are shown in **Figure 4.3**.

Table 4.2: Sequence of data collection for Rat C. Single-channel stimulation by channel C3 elicited no leg twitch or behavioral response up to 200 μA, precluding data collection for this channel.

Start Date	End Date	Days Post-Implantation	Stimulus Configuration	Number of Sessions	Algorithm	Notes
7/10/19	7/30/19	93-113	Multi-Channel (All)	8	MCS	-
9/23/19	9/25/19	168-170	Single-Channel (C1)	3	MCS	-
9/26/19	9/26/19	171	Single-Channel (C2)	1	MCS	-
9/27/19	9/27/19	172	Single-Channel (C4)	1	MCS	-
9/30/19	9/30/19	175	Single-Channel (P1)	1	MCS	-
10/1/19	10/1/19	176	Single-Channel (P2)	1	MCS	-
10/3/19	10/4/19	178-179	Single-Channel (P3)	2	MCS	-
10/5/19	10/5/19	180	Single-Channel (P4)	2	MCS	-
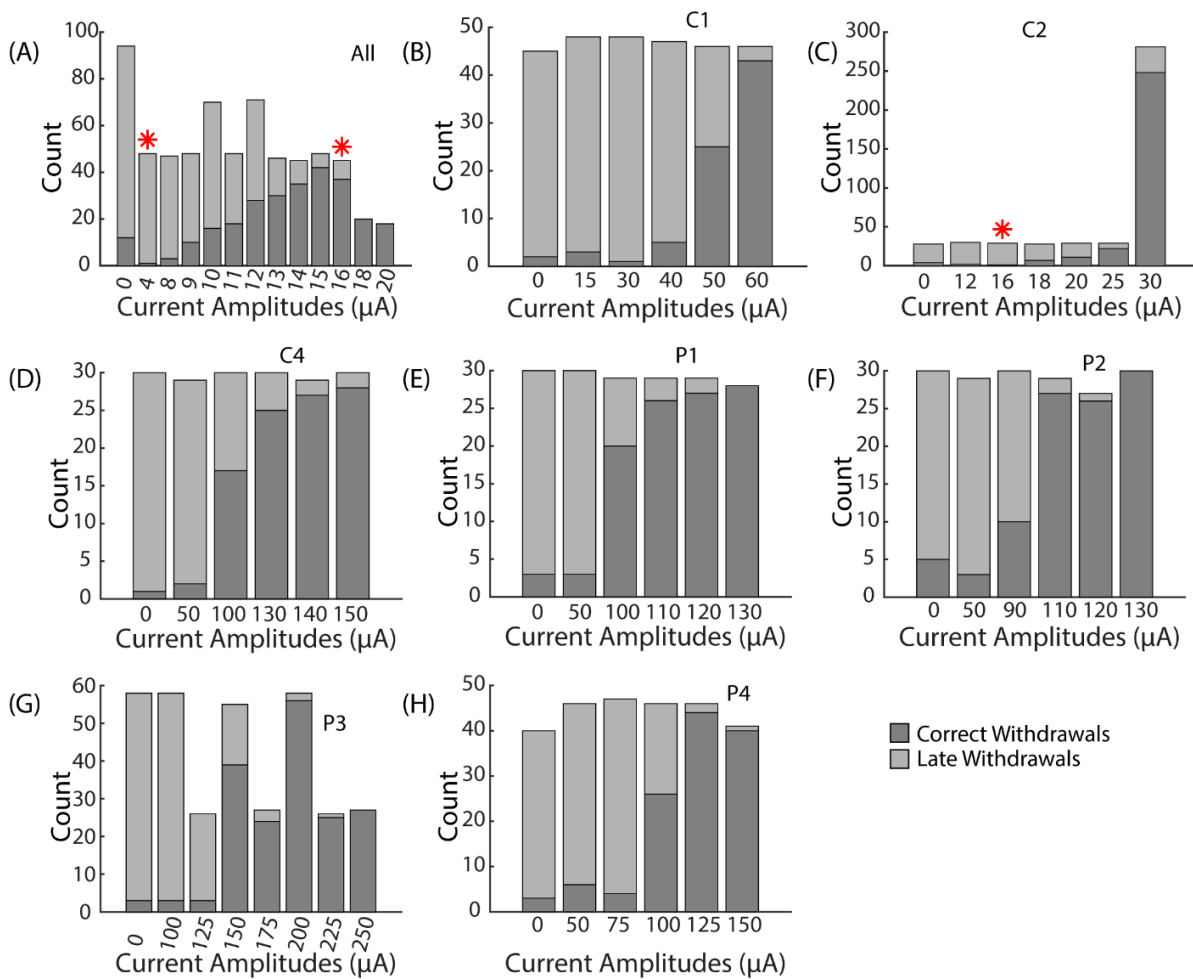
Figure 4.3: Breakdown of trials by current amplitude and stimulus configuration performed by Rat C. Single-channel stimulation by channel C3 elicited no leg twitch or behavioral response up to 200 μA, precluding data collection for this channel. Maintenance trials were excluded in all cases except for channel C2, for which their inclusion was deemed necessary to ensure an optimum fit of the psychometric curve. Red stars denote amplitudes for which the rat's performance levels were deemed outliers and excluded from data analysis (see **Section 3.6.4**).

4.1.2 Rat D

Rat D arrived in the laboratory in September 2019 (aged 5 weeks) and underwent initial shaping on the auditory discrimination task. This effort persisted for roughly 10 weeks but did not yield results, and so the rat was repurposed to the go/no-go detection task. It performed interval training, withdrawal training, and the main auditory detection task between 12/23/2019 and 1/2/2020. The unavailability of suitable macro-sieve assembles delayed surgery first to mid-February and then to mid-March. The onset of the COVID-19 pandemic and resulting lockdown delayed surgery even further.

I returned to the laboratory in early June, more than five months since the rat had last trained on the behavioral task. I therefore thought it advisable that the rat undergo another round of training with auditory stimuli before proceeding to surgery. This lasted from 6/8/2020 to 6/29/2020. Admittedly, this retraining could have concluded sooner had I adhered more strictly to criterion standards. However, given the rat's relatively advanced age at this point, I wanted to make sure that its performance sustained over multiple sessions.

Rat D underwent surgery for MSE implantation and head-cap construction on 7/15/2020. Roughly 9 weeks later (on 9/14/2020), it resumed training with auditory stimuli. Auditory retraining concluded on 9/22/2020. The rat then proceeded with the transition from auditory stimuli to electrical stimulation alone, using the same method that worked for Rats A, B, and C. It then performed three sessions of the detection task with fixed current amplitude. Finally, from 9/29/2020 to 11/19/2020, it performed the detection task for multi-channel and single-channel stimulus configurations. This included two rounds of data collection with three weeks' separation for a subset of single-channel configurations (C1, C2, C3, C4, P1). Single-channel stimulation by channel P4 elicited no leg twitch or behavioral response up to 200 μA, precluding data collection
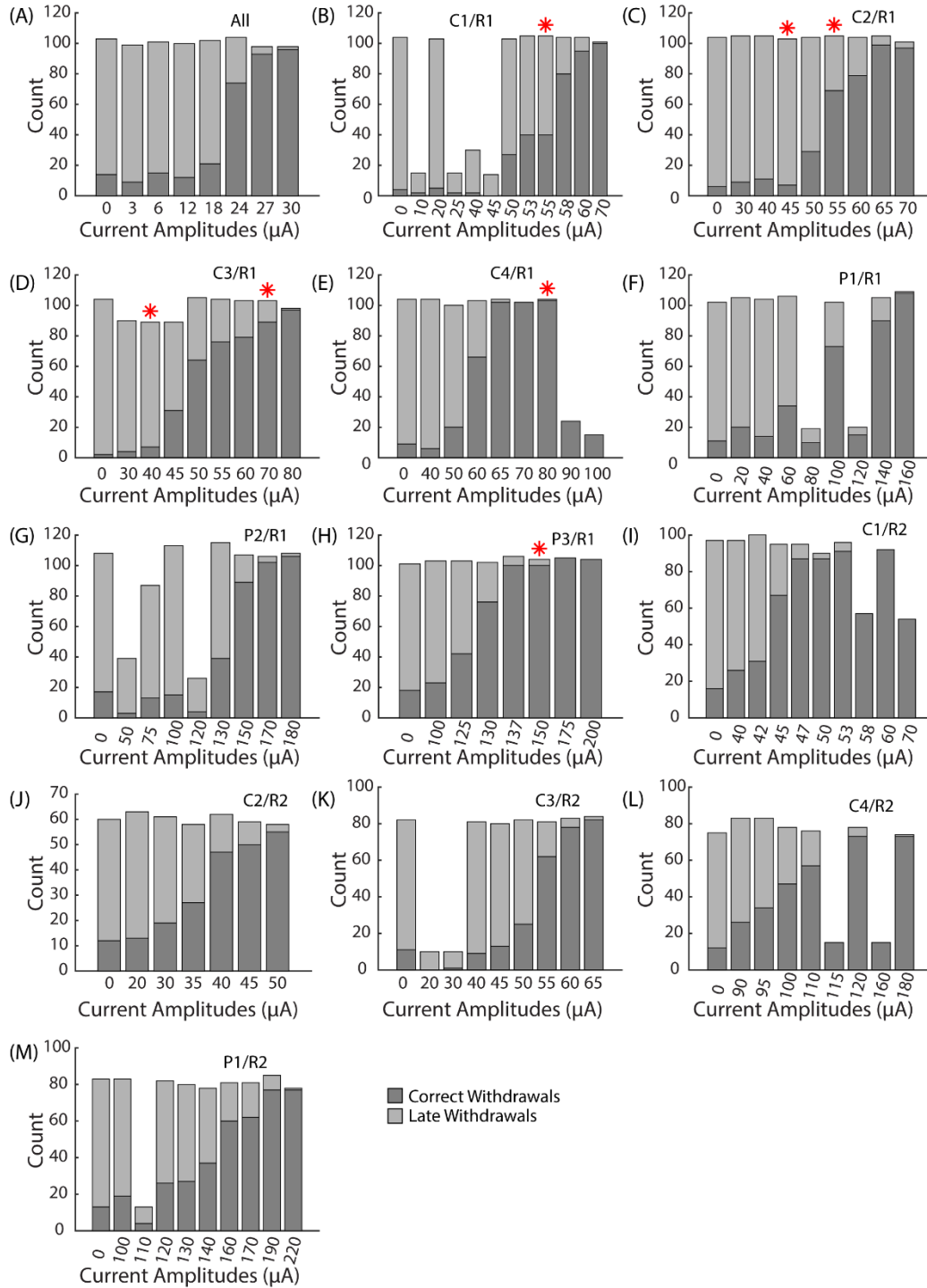
Figure 4.4: Breakdown of current amplitudes applied to Rat D for the multi-channel and single-channel stimulus configurations. Single-channel stimulation by channel P4 elicited no leg twitch or behavioral response up to 200 µA, precluding data collection for this channel. Two rounds of data collection are shown for single-channel stimulus configurations C1, C2, C3, C4, and P1. The first round (**B-F**) and second round (**I-M**) were separated longitudinally by three weeks. Red stars denote amplitudes for which the rat's performance levels were deemed outliers and excluded from subsequent data analysis.

116

Table 4.3: Sequence of data collection for Rat D. Single-channel stimulation by channel P4 elicited no leg twitch or behavioral response up to 200 μA, precluding data collection for this channel.

Start Date	End Date	Days Post-Implantation	Stimulus Configuration	Number of Sessions	Algorithm	Notes
9/29/2020	10/3/2020	76-80	Multi-Channel (All)	6	MCS	-
10/19/2020	10/20/2020	96-97	Single-Channel (C1)	8	MCS	Round 1/2
10/21/2020	10/21/2020	98	Single-Channel (C2)	5	MCS	Round 1/2
10/22/2020	10/23/2020	99-100	Single-Channel (C3)	6	MCS	Round 1/2
10/23/2020	10/24/2020	100-101	Single-Channel (C4)	5	MCS	Round 1/2
10/25/2020	10/26/2020	102-103	Single-Channel (P1)	6	MCS	Round 1/2
10/27/2020	10/30/2020	104-107	Single-Channel (P2)	5	MCS	-
11/2/2020	11/4/2020	110-112	Single-Channel (P3)	7	MCS	-
11/5/2020	11/6/2020	113-114	Single-Channel (C1)	5	MCS	Round 2/2
11/6/2020	11/7/2020	114-115	Single-Channel (C2)	3	MCS	Round 2/2
11/11/2020	11/12/2020	119-120	Single-Channel (C3)	5	MCS	Round 2/2
11/13/2020	11/13/2020	121	Single-Channel (C4)	5	MCS	Round 2/2
11/18/2020	11/19/2020	126-127	Single-Channel (P1)	7	MCS	Round 2/2

for this channel. **Table 4.3** summarizes the data collected. Breakdowns of what current amplitudes were applied and how many times under MCS are shown for each stimulus configuration in **Figure 4.4**.

4.2 Processing the Data

Time-stamped event logs were used to populate a PostgreSQL database from which trial-level information for each dataset was extracted for analysis in MATLAB. Each trial had an associated stimulus amplitude, a withdrawal time following stimulus onset, an outcome (EW, CW, or LW), and a mode (normal or maintenance). EWs were discarded at the outset. Trials in which the rat withdrew less than 100 ms after stimulus onset were also excluded from the analysis (**Figure 4.5**); CWs that occurred faster than this reaction time were deemed to have been coincidental, and not to have been in response to the actual stimulus. Finally, maintenance trials were excluded unless noted otherwise.
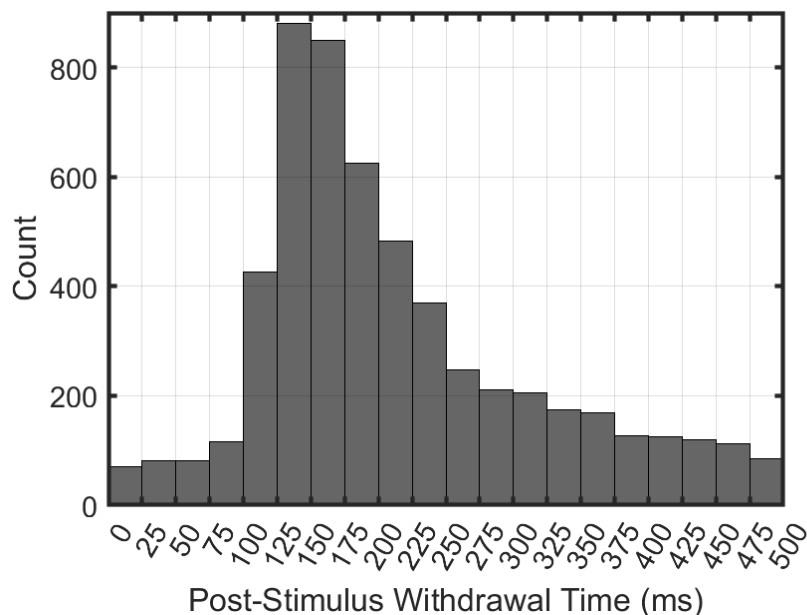
Figure 4.5: Histogram depicting the distribution of CWs for all 4 rats by post-stimulus withdrawal time. The number of CWs showed a sharp increase above 100 ms, suggesting that this would be a good cutoff for a minimum reaction time.

4.3   Analyzing the Data

The data collected for Rats A, B, C, and D produced 23 datasets (**Table 4.4**). The psychometric quick function was fitted to each dataset by maximum likelihood estimation to yield optimized parameter values $\hat{\theta} = \{\hat{\alpha}, \hat{\beta}, \hat{\gamma}, \hat{\lambda}\}$ following removal of outliers. These parameter values enabled the calculation of detection thresholds x_T and slopes $\psi'(x_T; \hat{\theta})$. They also provided a generating function for the Monte Carlo bootstrap, which generated $B = 10,000$ simulated sessions $\hat{\theta}^*$ with the same distribution of trials as the empirical dataset. Comparison of the empirical deviance against those of the simulated sessions enabled the calculation of the goodness-of-fit metric pDev. The bootstrapped sessions also facilitated the calculation of 95% BCa confidence intervals for the empirical threshold and slope values.

Table 4.4: Summary of data collected. Each dot represents one dataset. Pairs of dots indicate data collected at two timepoints (longitudinal data). Single-channel stimulation by channel C3 in Rat C and channel P4 in Rat D produced no leg twitch or behavioral response up to 200 µA, precluding data collection and subsequent generation of psychometric curves for these channels.

	Multi-Channel Stimulation	Single-Channel Stimulation							
		C1	C2	C3	C4	P1	P2	P3	P4
Rat A	●								
Rat B	●								
Rat C	●	●	●		●	●	●	●	●
Rat D	●	●●	●●	●●	●●	●●	●	●	

4.3.1 Multi-Channel Stimulation

Psychometric curves for the multi-channel stimulus configuration were generated for Rats A, B, C, and D (see **Figure 4.6** and **Table 4.5**). For this stimulus configuration, the average threshold current per channel necessary to elicit a behavioral response was 19.37 µA (3.87 nC), and the average slope was 9.30 µA^{-1} (46.50 nC^{-1}). Bootstrapped estimates of the thresholds' CI$_{95}$ widths ranged from 0.87 to 4.34 µA ($0.17 - 0.87$ nC). For slopes, CI$_{95}$ widths for Rats A, B, and C were

3.60, 2.43, and 7.16 µA^{-1} (18.03, 12.13, and 35.79 nC^{-1}), respectively. Rat D's CI$_{95}$ for slope was much larger, spanning 88.57 µA^{-1} (442.84 nC^{-1}).
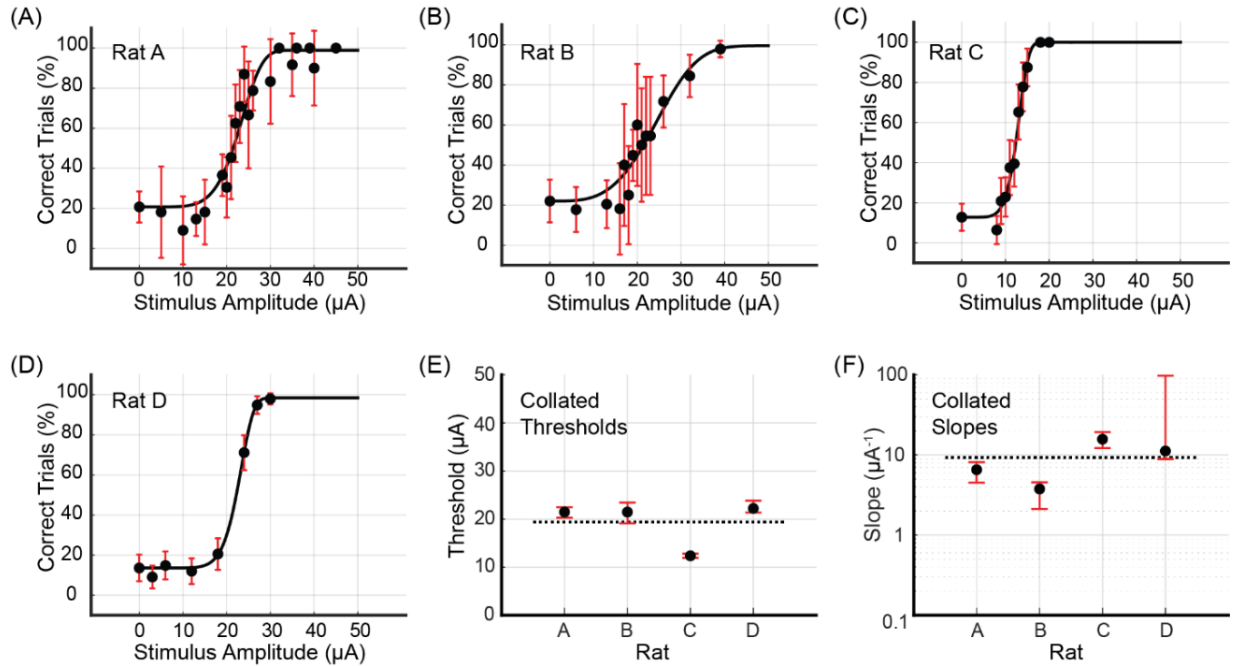
Figure 4.6: (A-D) Psychometric curves for Rats A, B, C, and D stimulated with the multi-channel configuration, in which equal currents passed through all eight channels simultaneously. Reported stimulus amplitudes correspond to currents passed through each individual channel, and not the total current. Error bars represent 95% confidence intervals for binomial distributions based on detection probabilities. See **Table 4.5** for fitted parameters, 50% detection thresholds, slopes, and goodness of fit metrics. **(E-F)** Collated 50% detection thresholds (x_T) and slopes ($\psi'(x_T; \hat{\theta})$) extracted from the preceding four psychometric curves. Horizontal dotted lines represent the mean values across all 4 rats. Error bars represent 95% BC_a confidence intervals.

Table 4.5: Fitted parameters α, β, γ, and λ for the four psychometric curves generated by multi-channel stimulation of Rats A, B, C, and D (see **Figure 4.6**). Also presented are the total number of trials N (excluding outliers), the 50% detection threshold x_T and slope $\psi'(x_T; \hat{\theta})$, their 95% confidence intervals (expressed as upper bound/lower bound), and the goodness of fit measure pDev.

	Days	N	α (µA)	β	γ	λ	x_T (µA) (nC)	$\psi'(x_T; \theta)$ (µA^{-1}) (nC^{-1})	pDev
Rat A	114-138	687	22.87	6.12	20.75%	1.08%	21.46 ± 1.02/1.15 (4.29 ± 0.20/0.23)	6.54 ± 1.59/2.01 (32.71 ± 7.96/10.07)	0.93
Rat B	119-126	421	24.19	3.64	22.03%	0.48%	21.45 ± 1.99/2.35 (4.29 ± 0.40/0.47)	3.76 ± 0.79/1.64 (18.82 ± 3.94/8.19)	0.11
Rat C	82-102	555	12.76	6.98	12.77%	0.00%	12.37 ± 0.45/0.42 (2.47 ± 0.09/0.08)	15.71 ± 3.55/3.61 (78.57 ± 17.76/18.03)	0.49
Rat D	76-80	805	22.73	9.14	13.59%	1.57%	22.21 ± 1.61/0.85 (4.44 ± 0.32/0.17)	11.18 ± 86.28/2.29 (55.88 ± 431.40/11.44)	0.17

4.3.2 Single-Channel Stimulation

Rat C

Single-channel stimulation of Rat C yielded seven psychometric curves, one each for channels C1, C2, C4, P1, P2, P3, and P4 (see **Figure 4.7** and **Table 4.6**). Stimulation by C3 up to 200 µA produced no visible leg movement or behavioral response, precluding the generation of a psychometric curve for this channel. Detection thresholds calculated for the three functioning core channels (C1, C2, and C4) ranged from 22.32 to 96.76 µA (4.64 to 19.35 nC; average value 56.17 µA or 11.21 nC), with CI_{95} widths between 3.95 and 23.53 µA (0.79 and 4.71 nC). Corresponding slopes ranged from 1.35 to 7.27 $µA^{-1}$ (6.73 to 36.37 nC^{-1}; average value 4.88 $µA^{-1}$ or 24.39 nC^{-1}), with CI_{95} widths from 3.26 to 72.17 $µA^{-1}$ (16.28 to 431.40 nC^{-1}). For the peripheral channels (P1, P2, P3, and P4), detection thresholds ranged from 90.18 to 144.20 µA (18.04 to 28.84 nC; average value 107.35 µA or 21.47 nC), with CI_{95} widths between 11.26 and 25.09 µA (2.25 and 5.02 nC). The corresponding slopes varied from 1.94 to 5.07 $µA^{-1}$ (9.70 to 25.37 nC^{-1}; average value 3.46 $µA^{-1}$ or 17.29 nC^{-1}), with CI_{95} widths between 2.31 and 29.15 $µA^{-1}$ (11.56 to 145.75 nC^{-1}).
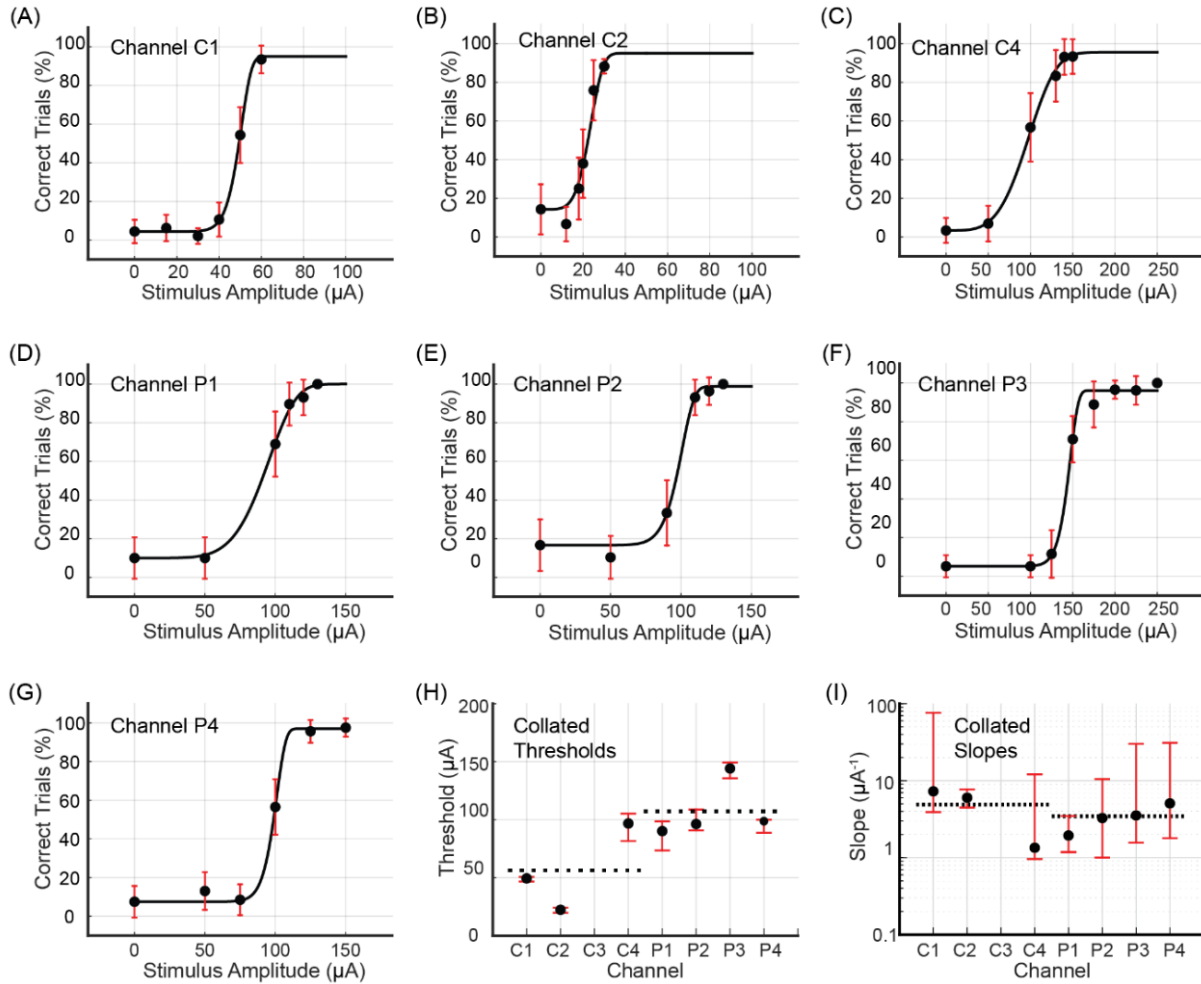
Figure 4.7: (A-G) Psychometric curves for Rat C generated by single-channel stimulation through individual channels C1, C2, C4, P1, P2, P3, and P4. Single-channel stimulation by channel C3 elicited no leg twitch or behavioral response up to 200 μA, precluding the generation of a psychometric curve for this channel. Error bars represent 95% confidence intervals for binomial distribution based on detection probability. See **Table 4.6** for fitted parameters, 50% detection thresholds, slopes, and goodness of fit metrics. **(H,I)** Collated 50% detection thresholds (x_T) and slopes $(\psi'(x_T; \hat{\theta}))$ extracted from the preceding seven psychometric curves. Horizontal dotted lines depict mean values for core and peripheral channels. Error bars represent 95% BC_a confidence intervals.

Table 4.6: Fitted parameters α, β, γ, and λ for psychometric curves generated by single-channel stimulation of channels C1, C2, C4, P1, P2, P3, and P4 in Rat C (see **Figure 4.7**). Also presented are the total number of trials N (excluding outliers), the 50% detection threshold x_T and slope $\psi'(x_T; \theta)$, their 95% confidence intervals (expressed as upper bound / lower bound), and the goodness of fit measure pDev. The data underlying channel C2's psychometric curve included a relatively large number of maintenance trials. For this channel, the number of non-maintenance (*i.e.,* normal) trials is reported in parentheses.

Channel	Days	N	α (μA)	β	γ	λ	x_T (μA) (nC)	$\psi'(x_T; \theta)$ (μA^{-1}) (nC^{-1})	pDev
C1	149-151	280	49.38	11.42	4.44%	5.00%	49.42 ± 1.23/2.72 (9.88 ± 0.25/0.54)	7.27 ± 68.82/3.35 (36.37 ± 344.10/16.74)	0.23
C2	160	425 (180)	23.08	5.11	14.29%	5.00%	22.32 ± 1.80/2.53 (4.46 ± 0.36/0.51)	6.02 ± 1.71/1.55 (30.08 ± 8.55/7.73)	0.68
C4	161	178	96.32	4.05	3.33%	4.51%	96.76 ± 8.46/15.07 (19.35 ± 1.69/3.01)	1.35 ± 10.77/0.39 (6.73 ± 53.86/1.94)	0.09
P1	164	175	92.71	5.95	10.00%	0.00%	90.18 ± 8.41/16.68 (18.04 ± 1.68/3.34)	1.94 ± 1.55/0.76 (9.70 ± 7.75/3.80)	0.28
P2	165	175	98.51	12.41	16.67%	1.22%	96.26 ± 12.59/5.46 (19.25 ± 2.52/1.09)	3.27 ± 7.22/2.27 (16.37 ± 36.11/11.34)	0.56
P3	167-168	335	144.38	16.30	5.17%	3.89%	144.20 ± 5.18/8.49 (28.84 ± 1.04/1.70)	3.54 ± 26.70/1.98 (17.70 ± 133.51/9.90)	0.45
P4	169	266	99.18	16.54	7.50%	2.98%	98.74 ± 1.26/9.99 (19.75 ± 0.25/2.00)	5.07 ± 25.87/3.28 (25.37 ± 129.37/16.38)	0.33

Rat D

Rat D underwent two rounds of data collection for single-channel stimuli. The first round resulted in the generation of seven psychometric curves for channels C1, C2, C3, C4, P1, P2, and P3 (see **Figure 4.8** and **Table 4.7**). Stimulation by P4 produced no muscle twitch or behavioral response up to 200 μA, preventing psychometric curve generation for this channel. In the first round, the core channels (C1, C2, C3, and C4) had detection thresholds ranging from 49.05 to 57.75 μA (9.81 to 11.55 nC; average value 54.00 μA or 10.80 nC), with CI$_{95}$ widths between 1.58 and 3.28 μA (0.32 and 0.66 nC). Corresponding slopes were between 3.29 and 7.82 μA^{-1} (16.44 and 39.10 nC^{-1}; average value 6.04 μA^{-1} or 30.18 nC^{-1}), with CI$_{95}$ widths from 1.26 to 4.35 μA^{-1} (6.29 to 21.77 nC^{-1}). The 3 functioning peripheral channels (P1, P2, and P3) had detection thresholds between 81.47 and 138.15 μA (16.29 and 27.63 nC; average value 115.20 μA or 23.04 nC), with CI$_{95}$ widths from 3.72 to 14.53 μA (0.74 to 2.91 nC). The corresponding slopes ranged from
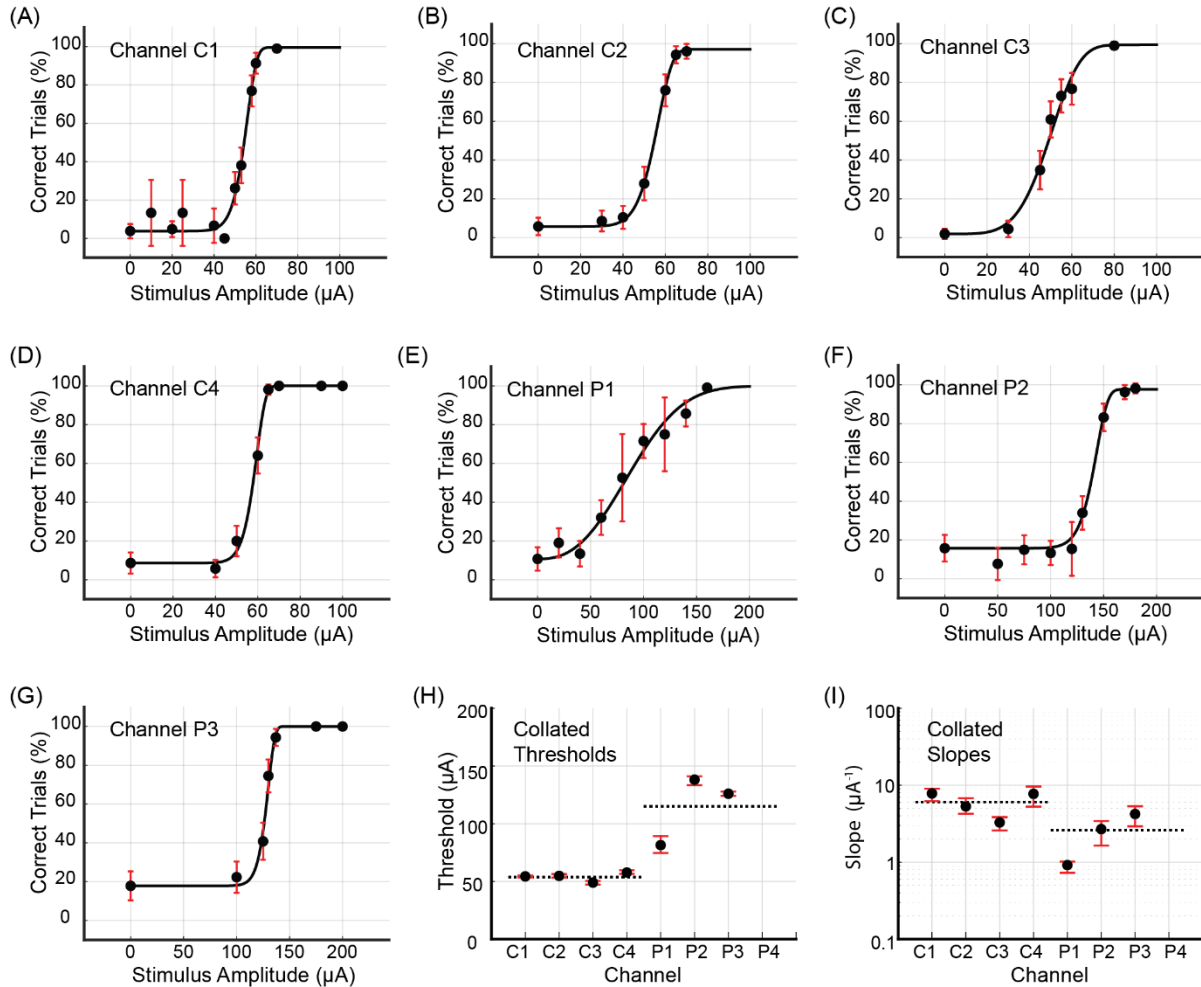
Figure 4.8: (A-G) Psychometric curves for Rat D generated by the first round of single-channel stimulation through individual channels C1, C2, C3, C4, P1, P2, and P3. Single-channel stimulation by channel P4 elicited no leg twitch or behavioral response up to 200 μA, precluding the generation of a psychometric curve for this channel. Error bars represent 95% confidence intervals for binomial distribution based on detection probability. See **Table 4.7** for fitted parameters, 50% detection thresholds, slopes, and goodness of fit metrics. **(H,I)** Collated 50% detection thresholds (x_T) and slopes ($\psi'(x_T; \hat{\theta})$) extracted from the preceding seven psychometric curves. Horizontal dotted lines depict mean thresholds for core and peripheral channels. Error bars represent 95% BC$_a$ confidence intervals.

0.92 to 4.23 μA^{-1} (4.59 to 21.14 nC^{-1}; average value 2.61 μA^{-1} or 13.07 nC^{-1}), with CI$_{95}$ widths between 0.29 and 2.40 μA^{-1} (1.43 and 11.99 nC^{-1}).

Data collection for the second round occurred approximately three weeks after the first, yielding a second set of psychometric curves for channels C1, C2, C3, C4, and P1 (see **Figure 4.9** and **Table 4.8**). Channels P2 and P3 were excluded from this round because the rat's waning performance

Table 4.7: Fitted parameters α, β, γ, and λ for psychometric curves generated by the first round of single-channel stimulation of channels C1, C2, C3, C4, P1, P2, and P3 in Rat D (see **Figure 4.8**). Also presented are the total number of trials N (excluding outliers), the 50% detection threshold x_T and slope $\psi'(x_T; \theta)$, their 95% confidence intervals (expressed as upper bound / lower bound), and the goodness of fit measure pDev.

Channel	Days	N	α (µA)	β	γ	λ	x_T (µA) (nC)	$\psi'(x_T; \theta)$ (µA^{-1}) (nC^{-1})	pDev
C1	96-97	798	54.59	13.04	3.85%	0.45%	54.38 ± 0.68/0.90 (10.88 ± 0.14/0.18)	7.82 ± 1.22/1.60 (39.10 ± 6.08/7.98)	0.57
C2	98	728	55.09	9.34	5.77%	2.92%	54.82 ± 1.53/1.52 (10.96 ± 0.31/0.30)	5.31 ± 1.45/1.06 (26.55 ± 7.26/5.31)	0.26
C3	99-100	693	49.25	4.8	1.92%	0.59%	49.05 ± 1.44/1.84 (9.81 ± 0.29/0.37)	3.29 ± 0.57/0.69 (16.44 ± 2.84/3.46)	0.94
C4	100-101	656	58.3	14.81	8.65%	0.00%	57.75 ± 2.02/1.17 (11.55 ± 0.40/0.23)	7.73 ± 1.90/2.46 (38.63 ± 9.49/12.28)	0.74
P1	102-103	772	87.34	2.59	10.78%	0.00%	81.47 ± 7.77/6.76 (16.29 ± 1.55/1.35)	0.92 ± 0.10/0.19 (4.59 ± 0.49/0.94)	0.94
P2	104-107	809	140.53	14.41	15.74%	2.34%	138.15 ± 3.06/4.71 (27.63 ± 0.61/0.94)	2.69 ± 0.75/1.04 (13.47 ± 3.73/5.19)	0.33
P3	110-112	724	127.95	21.44	17.82%	0.00%	125.98 ± 1.94/1.78 (25.20 ± 0.39/0.36)	4.23 ± 1.10/1.30 (21.14 ± 5.49/6.50)	0.77

lowered the stimulation rate and prevented the accumulation of sufficient trials for analysis. Detection thresholds for C1 and C2 decreased by 20% and 36%, respectively. While C3's threshold increased marginally by 7%, thresholds for C4 and P1 increased markedly by 70% and 75%, respectively. **Figure 4.10** shows the longitudinal development of Rat D's thresholds and slopes.
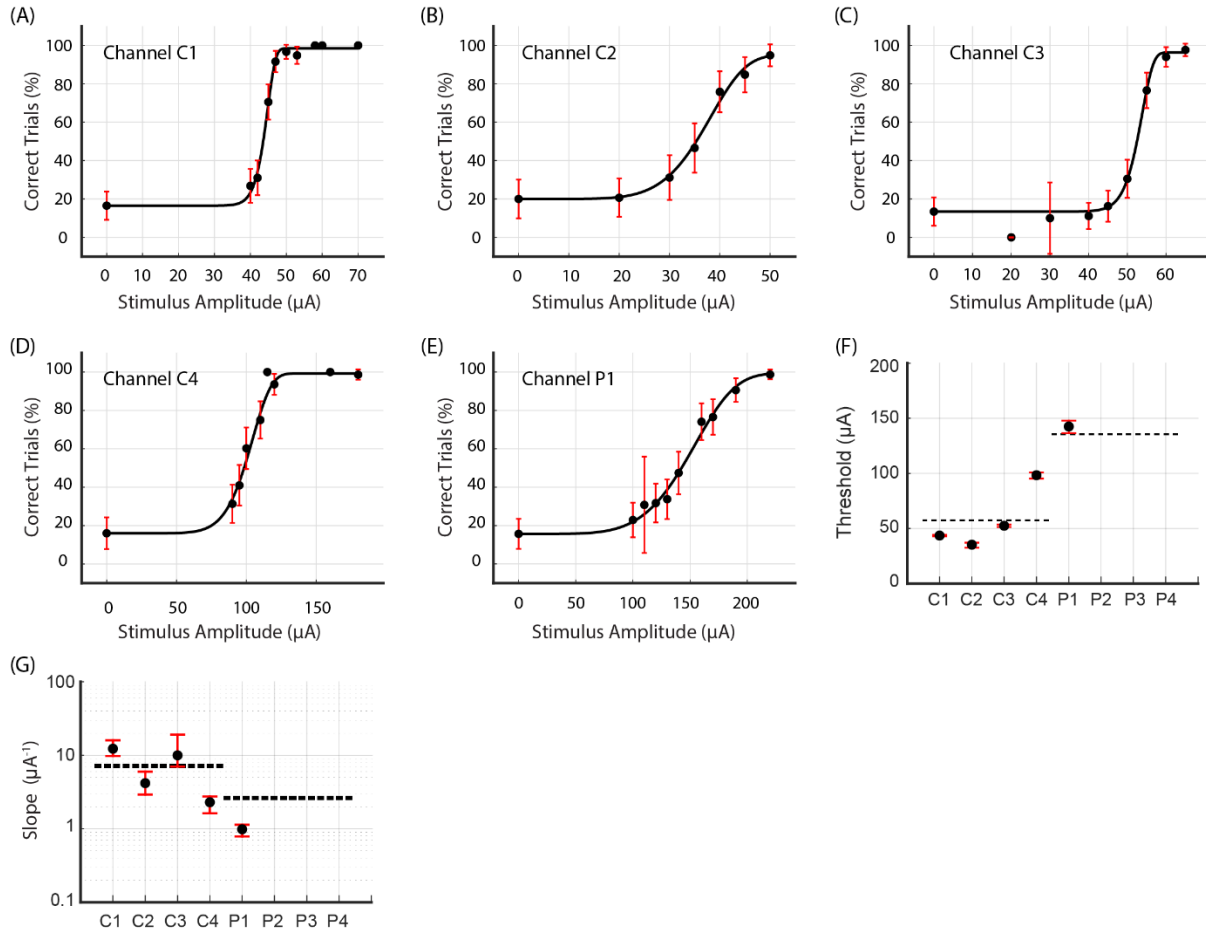
Figure 4.9: (A-E) Psychometric curves for Rat D generated by the second round of single-channel stimulation through individual channels C1, C2, C3, C4, and P1. Channels P2 and P3 were excluded from this round of data collection because of the rat's waning performance. Error bars represent 95% confidence intervals for binomial distribution based on detection probability. See **Table 4.8** for fitted parameters, 50% detection thresholds, slopes, and goodness of fit metrics.

Table 4.8: Fitted parameters α, β, γ, and λ for psychometric curves generated by the second round of single-channel stimulation of channels C1, C2, C3, C4, and P1 in Rat D (see **Figure 4.9**). Also presented are the total number of trials N (excluding outliers), the 50% detection threshold x_T and slope $\psi'(x_T; \theta)$, their 95% confidence intervals (expressed as upper bound / lower bound), and the goodness of fit measure pDev.

Channel	Days	N	α (µA)	β	γ	λ	x_T (µA) (nC)	$\psi'(x_T; \theta)$ (µA^{-1}) (nC^{-1})	pDev
C1	113-114	873	44.14	21.02	16.49%	1.58%	43.57 ± 0.66/0.59 (8.71 ± 0.13/0.12)	12.29±3.70/2.52 (61.44±18.48/12.59)	0.91
C2	114-115	421	37.05	6.41	20.00%	4.90%	35.32 ± 1.84/2.81 (7.06 ± 0.37/0.56)	4.18±1.80/1.25 (20.88±8.99/6.25)	0.2
C3	119-120	593	52.96	19.43	13.41%	3.70%	52.49±1.06/1.16 (10.50±0.21/0.23)	9.98±9.11/2.98 (49.91±45.53/14.88)	0.36
C4	121	577	101.53	8.72	16.00%	0.71%	98.34±2.57/3.05 (19.67±0.51/0.61)	2.29±0.45/0.67 (11.47±2.26/3.36)	0.76
P1	126-127	744	149.94	5.37	15.66%	0.58%	142.51±5.32/5.97 (28.50±1.06/1.19)	0.98 ± 0.15/0.20 (4.92 ± 0.75/0.98)	0.12

126
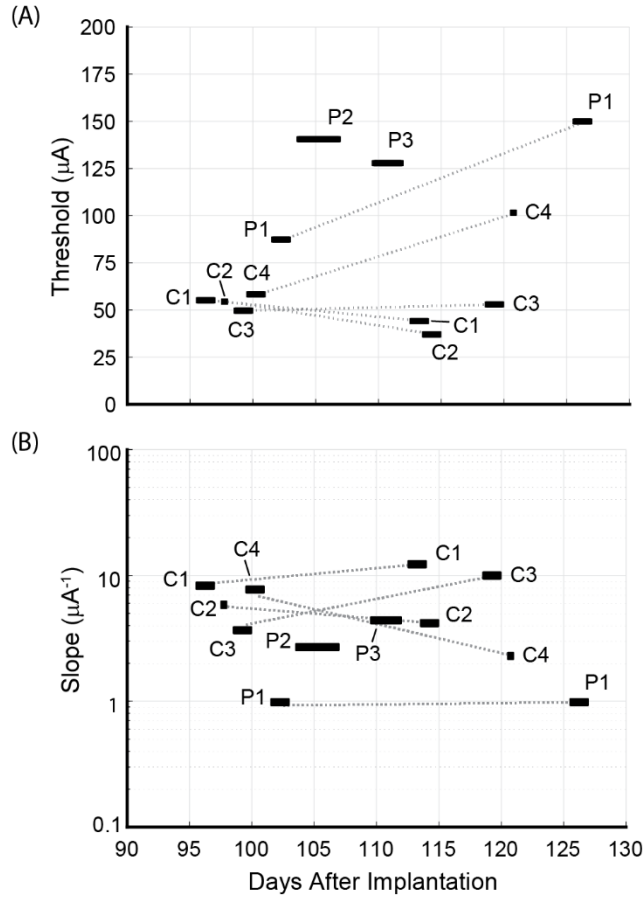
Figure 4.10: Longitudinal development of **(A)** detection thresholds x_T and **(B)** slopes $\psi'(x_T; \hat{\theta})$ for Rat D. Psychometric data for individual channels C1, C2, C3, C4, and P1 were calculated using behavioral data gathered at two timepoints spaced 3 weeks apart. The rat's waning performance beyond 127 days post-implantation precluded a 2nd round of data collection for channels P2 and P3. Detection thresholds for channels C1, C2, and C3 remained steady or decreased slightly across timepoints. Detection thresholds for C4 and P1 increased dramatically. No pattern was evident for the longitudinal development of slopes.

4.4 Discussion

The complex and irreversible nature of MSE implantation precludes human testing at this early stage of development. Nevertheless, there remains an urgent need for characterization of the MSE's sensory performance in a preclinical setting to set the stage for future human studies. Previous work by MacEwan et al. (2016) has shown that the rat sciatic nerve can successfully regenerate through the MSE's nine transit zones, allowing selective recruitment of distal musculature. This motivated my development of the CRSNB model and its application to the

measurement of MSE detection thresholds. Psychometric curves generated by MCS yielded a range of thresholds and slopes for multi-channel and single-channel stimulus configurations. I discuss my findings in the sections that follow.

4.4.1 Detection Thresholds Under Multi-Channel Stimulation

Under multi-channel stimulation, Rats A, B, and D had similar detection thresholds of 21-22 μA per channel (corresponding to 4.2-4.4 nC of charge injection per channel, or a charge density of 157-163 nC/mm^2). Rat C had a considerably lower threshold of 12 μA per channel (2.4 nC, 91 nC/mm^2). Notably, the threshold currents injected per channel for Rat C (12 μA) and Rat D (22 μA) fell well below their corresponding lowest single-channel thresholds of 22 μA (channel C2) and 49 μA (channel C3, first round), respectively. This can be explained by assuming that the axons activated by these single channels must have been the first to be activated under multi-channel stimulation. Since axon activation depends on local current density, the addition of equal currents from seven other channels likely lowered the per-channel current needed to achieve the current density required for activation.

4.4.2 Detection Thresholds Under Single-Channel Stimulation

For single-channel stimulation, a one-tailed Mann-Whitney U test indicated that the average detection threshold for the core channels (median 52.49 μA) was less by approximately half that of the peripheral channels (median 112.36 μA), $U = 6, p = 0.0003969$. This relationship held true for both Rat C (56 μA vs. 107 μA, or 11.2 nC vs. 21.5 nC) and Rat D (56 μA vs. 115 μA, or 11.2 nC vs. 23.0 nC). In terms of current density, the discrepancy was even more pronounced (reflecting the core channels' larger areas): 351 nC/mm^2 vs. 954 nC/mm^2 for Rat C; 348 nC/mm^2

vs. 1,085 nC/mm^2 for Rat D. This divergence of core and peripheral channel thresholds may have had multiple causes. I discuss these below.

Differential Distribution of Sensory Axons

Following transection, peripheral nerve regeneration commences with the formation of a bridge of dense extracellular matrix and inflammatory cells between the proximal and distal stumps. Vascularization of this intervening tissue creates a pathway for migrating Schwann cells to tow proximal axons towards distal innervation targets (Cattin and Lloyd, 2016). Suzuki et al. (1998) have shown that regeneration of sensory axons precedes that of motor axons immediately after axotomy. Accordingly, there is an increased proliferation of sensory axons toward the nerve's center and of motor axons toward the periphery (Negredo et al., 2004; Lago et al., 2005). This differential proliferation implies that the distance from a core channel to an average regenerated sensory axon should be less than from a peripheral channel. Previous simulations by Zellmer et al. (2018) have predicted that regenerated axons' thresholds for activation are not inherently higher or lower than those of undisrupted axons, but rather depend on proximity to the stimulating lead. Essentially, thresholds for nearby regenerated axons should be lower than for naïve axons of the same caliber, while thresholds for more distant regenerated axons should be higher than for their naïve counterparts. Thus, the higher density of regenerated axons at the nerve's center, coupled with the pronounced dependence of regenerated axons' recruitment on lead proximity, may have contributed to the observed discrepancy between core and peripheral channels' detection thresholds.

Lead Geometry

Differences in the core and peripheral leads' geometries may also have contributed to the threshold discrepancy (**Figure 4.11**). The MSE's core channels are 32,000 μm^2 in area and curved. Its
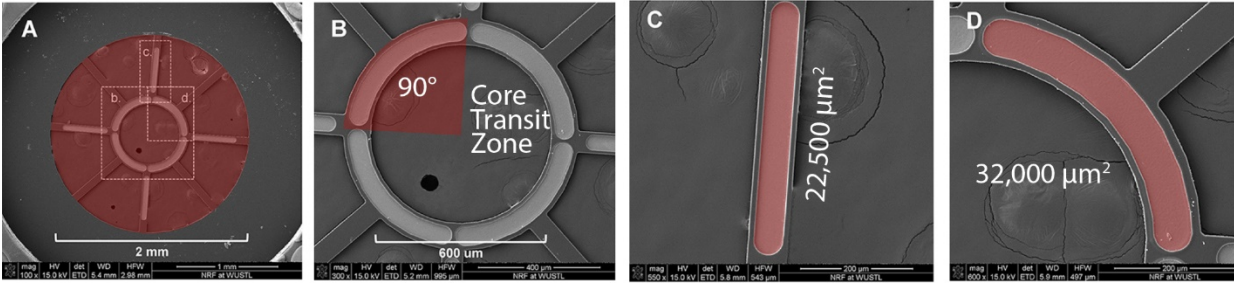
Figure 4.11: Scanning electron micrographs of (A) the complete MSE active region, (B) the four core channels with their curved geometries, (C) a peripheral channel with its straight geometry, and (D) a single core channel. Adapted from MacEwan et al. (2016).

peripheral channels are 22,500 μm^2 in area and straight. The core channels' greater areas means that their current density for a given current level is lower than the corresponding current density for the peripheral channels. Generally, higher current density is associated with increased axon recruitment. Concurrently, the core channels' curved geometry means that their "centers of mass" lie closer to centrally located axons than if their geometry was straight. Thus, the core channels may have had an outsized effect on central axons despite their larger areas, pushing their thresholds down. This effect would be magnified by the higher concentration of sensory axons toward the nerve's center.

Partial Extrusion of Peripheral Channels
The MSE's peripheral channels extend to a radius of 850 μA from the active region's center, far exceeding the 1-mm diameter of regenerated rat sciatic nerve (MacEwan et al., 2016), and even the 1.4-mm diameter of undisrupted nerve (Tyler and Durand, 2003). This suggests that some fraction of the peripheral channels' currents was injected into the extraneural space. However, the enclosure of the active region within a pair of 4-mm silicone guidance conduits would have ensured that any extraneural current must have flowed along the nerve's periphery, contributing to axon recruitment. It remains unclear to what extent the peripheral nerve channels extruded from the regenerated nerve, and how much their extrusion affected detection thresholds.

4.4.3 Longitudinal Trends for Detection Thresholds

Longitudinal examination of Rat D's detection thresholds using single-channel stimulation revealed disparate trends (**Figure 4.10A**). Five channels (C1, C2, C3, C4, and P1) were measured at two timepoints spaced 3 weeks apart. The decline in C1 and C2's thresholds may have been caused by the ongoing maturation of nearby regenerated axons (increased calibers, thicker myelin sheaths, and a greater proportion of myelinated axons), which is known to continue for up to 7 months post-implantation (Ceballos et al., 2002). Channel C3's threshold was stable, showing a minor increase between the two rounds. The dramatic rise in C4 and P1's thresholds coincided with increased channel impedances (**Figure 4.12**). For C4, the first round of data was gathered 100-101 days post-implantation. Corresponding impedances at 1 kHz ranged between 62.28 and 94.45 kΩ. From the 119th day onward, C4's impedance became erratic. Measured values on this day ranged between 26.74 and 397.08 kΩ. The second round of data was gathered on the 121st day. Although the impedances measured on this day were lower than 2 days prior, on subsequent days (up to 127 days post-implantation) some measurements exceeded 1 MΩ. For P1, the first and second rounds of data were gathered 102-103 and 126-127 days post-implantation, respectively. The corresponding impedances for these two rounds ranged between 86.16 and 166.66 kΩ, and between 161.34 and 771.69 kΩ, respectively. Impedances for P2 and P3 also rose drastically after their respective first rounds of data collection, which may explain why the rat's performance degraded during the attempted second round of data collection for these channels. Such sudden degradation of impedance suggests failure of the lead, the solder joint, the associated microwire, or damage to the skull-mounted connector. It remains unclear where the failure occurred.
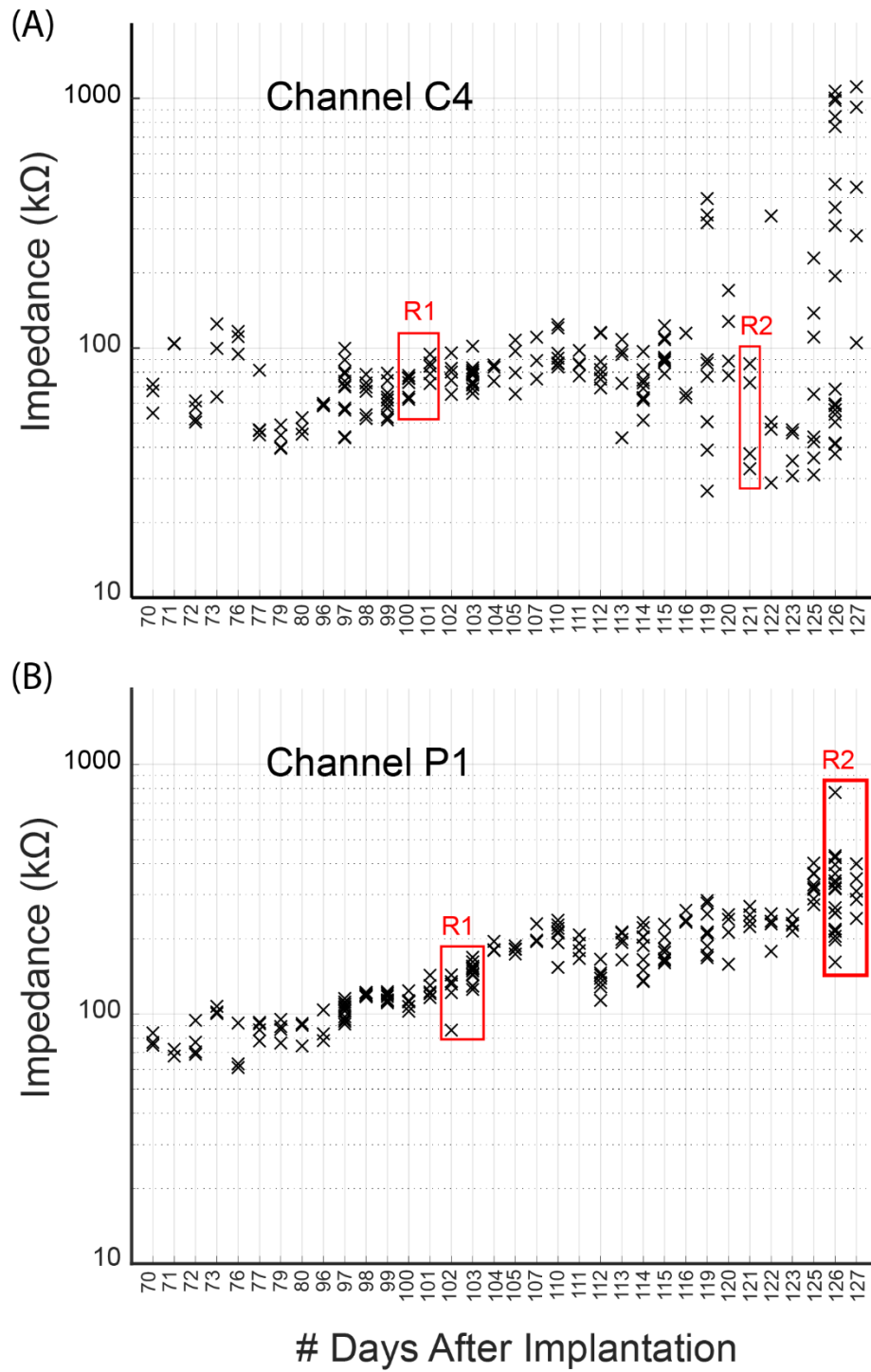
Figure 4.12: Impedance values measured for channels C4 and P1 of Rat D at the start of each experimental day. Values enclosed within red boxes correspond to the days on which the first (R1) and second (R2) rounds of data were collected for these channels.

Table 4.9: Reported thresholds for LIFE, FINE, TIME, and USEA electrodes expressed in units of charge density.

Electrode	Reported Threshold	Lead Area	Charge Density	Sources
LIFE	4.85 nC	79,030 μm^2	61 nC/mm^2	Nannini and Horch (1991) Dhillon et al. (2004)
FINE	69.1-109.7 nC	125,663 μm^2	550-873 nC/mm^2	Tyler and Durand (2002) Tan et al. (2015)
TIME	4-14 nC	5,654 μm^2	707-2,476 nC/mm^2	Boretius et al. (2010) Raspopovic et al. (2014)
USEA	12-27 μA	5,000 μm^2	480-1,080 nC/mm^2	Branner et al. (2012) Davis et al. (2016)

Table 4.10: MSE thresholds in units of current density.

	Multi-Channel Configuration (nC/mm^2)		Single-Channel Configurations (nC/mm^2)							
			C1	C2	C3	C4	P1	P2	P3	P4
Rat A	157		-	-	-	-	-	-	-	-
Rat B	157		-	-	-	-	-	-	-	-
Rat C	91		309	139	-	605	802	856	1,282	878
Rat D	163	R1	340	343	307	361	724	1,228	1,120	-
		R2	272	221	328	615	1,267	-	-	-

4.4.4 Comparing MSE Detection Thresholds with Other Electrodes

To assess how the MSE's ability to elicit sensory percepts compares with other electrodes, it is useful to look at detection thresholds not in units of current (μA) but of charge density (nC/mm^2). To understand why, recall that axon recruitment depends on the local density of current along its length ($\mu A/mm^2$). Therefore, converting currents to current densities accounts for differences in lead geometry – a given amplitude of current delivered via a large electrode will correspond to a lower current density than a smaller electrode. Likewise, converting current (μA) to charge (nC) standardizes for different pulse shapes and widths that can produce widely different axon recruitment profiles for the same current level. **Table 4.9** lists thresholds for LIFEs, FINEs, TIMEs, and USEAs, converted to units of current density. These may be compared against **Table 4.10**, which shows the threshold values in units of current density calculated for MSEs from each of the 23 datasets. We see that the range of threshold current densities for MSE stimulation is

comparable with those of other electrode classes, supporting the MSE's viability as a sensory interface for human trials.

4.4.5 Psychometric Slopes

The psychometric slope $\psi'(x_T; \hat{\theta})$ is a sensitivity measure that signifies the rapidity with which the percentagewise probability of stimulus detection rises with stimulus intensity. Measured slopes for multi-channel stimulation ranged from 3.76 to 15.71 μA^{-1} per channel, and for single-channel stimulation from 0.92 to 12.29 μA^{-1}. A steep slope implies that activation of nearby axons occurs with sufficient reliability that the transition from low to high detection probability occurs over a short span of increasing current; a shallow slope implies the opposite. For both Rats C and D, a one-tailed Mann-Whitney U test indicated that single-channel stimulation yielded steeper average slopes for the core channels (median 6.02 μA^{-1}) than the peripheral channels (median 2.98 μA^{-1}), $U = 72, p = 0.01017$. This may reflect the differential proliferation of sensory axons described by Suzuki et al. (1998). Since core channels reside in a region of high axon density, small current increments should significantly increase the number of axons recruited and hence the probability of a behavioral response (steep slope). Conversely, the lower density of axons surrounding the peripheral channels means that small current increments should recruit fewer additional axons, producing little change in the behavioral response probability (shallow slope). Other possible explanations mirror those provided for threshold discrepancies in **Section 4.3.2**, regarding differences in lead geometry and the partial extrusion of the peripheral channels' leads from the nerve's epineurium.

4.4.6 Longitudinal Trends for Psychometric Slopes

No clear longitudinal trends for Rat D's slope values were evident (**Figure 4.10B**). Five channels (C1, C2, C3, C4, and P1) were measured across two timepoints. Two channels' slopes became markedly steeper (C1 and C3 by 57 and 203%, respectively). One channel's slope increased slightly (P1 by 7%). The remaining two channels' slopes became shallower (C2 and C4 by 21 and 70%, respectively). There was no consistent relationship between changes in threshold and changes in slope.

4.4.7 Confidence Intervals

Wichmann and Hill (2001b) stress that bootstrapped confidence intervals do not measure a parameter's underlying variability, but rather the variability inherent in the sampling scheme (i.e., the selection of current amplitudes), the number of trials for each amplitude, and interactions between the sampling scheme and parameter calculation. In the present study, the relation between choice of sampling scheme and CI_{95} widths was readily apparent, as datasets whose sampling schemes placed fewer amplitudes in the sloped domain of the psychometric curve showed greater variation in bootstrapped parameter values and hence wider confidence intervals. This effect was more pronounced for slopes than thresholds. Bootstrapped slope values for Rat D under multi-channel stimulation showed considerable variation due to the placement of only one amplitude (24 µA) in the psychometric curve's sloped domain (see **Figure 4.6D,F**). Similarly, bootstrapped slopes for Rat C under single-channel stimulation also varied considerably with the exception of channel C2, for which multiple amplitudes lay in the sloped domain (see **Figure 4.7B,I**). Bootstrapped thresholds also showed a degree of variation for some channels. In contrast, Rat D's threshold and slope confidence intervals for single-channel stimulation were more constrained (see **Figure 4.9**), reflecting the adoption of a pseudo-adaptive strategy that evaluated the psychometric

curve at multiple mid-session timepoints to determine whether the sampling scheme's placement of amplitudes located them optimally in the curve's sloped domain, so that more amplitudes could be added as necessary.

4.5 Conclusions

The present study deployed the CRSNB model for the measurement of detection thresholds and associated psychometric slopes for MSE multi-channel and single-channel stimulus configurations. The MSE can elicit percepts using monopolar, single-channel stimulus configurations at charge densities that range from 139 to 1,282 nC/mm^2, which is comparable with other electrode designs (LIFE, FINE, TIME, USEA). Moreover, single-channel thresholds are not uniform across the nerve, but instead are lower for the core channels and higher for the peripheral channels. Longitudinally, the observed 3-week decline for a subset of channels' thresholds is consistent with continuing regeneration and maturation of nearby axons. These results represent an important step in establishing the MSE's viability as a sensory feedback interface and advancing the clinical translation of this technology.

Chapter 5: Future Directions

The preceding chapters of this dissertation have reported the successful deployment of the CRSNB model for the measurement of MSE detection thresholds and slopes under various monopolar stimulus configurations. Despite this success, there remains room for significant improvement. This chapter explores various ideas for extending the CRSNB model's utility and turning it into a truly formidable tool for the characterization of an electrode's capacity as a sensory interface.

5.1 Withdrawal Time Cutoff and Detection Threshold

In the go/no-go detection task, timely withdrawal from the nose-poke detector is taken as a proxy for stimulus detection. Reinterpreted in this context, the threshold x_T is that current amplitude for which the probability of withdrawal before the 500 ms cutoff is 50%. This means that when stimulated at x_T, the rat's withdrawal time will exceed 500 ms on 50% of trials and fall below 500 ms on the other 50% of trials. Similarly, each point on the psychometric curve corresponds to a different distribution of withdrawal times, where the probability represents the proportion of trials whose withdrawals fall below 500 ms. This is illustrated in **Figure 5.1**, which plots the withdrawal time for every CW and LW trial across all datasets as a function of the trial's current amplitude (normalized to the psychometric probability using the corresponding dataset's fitted parameters). Each gray dot represents a single trial. The large black markers denote the median withdrawal time over a small window of adjacent probabilities. The decrease in median withdrawal time as a function of probability is clearly visible.

The dependence of withdrawal time on current amplitude implies that the choice of cutoff must contribute in some manner to the values measured for detection thresholds. To test this, the psychometric analysis of **Chapter 4** was repeated using the same set of empirical data with
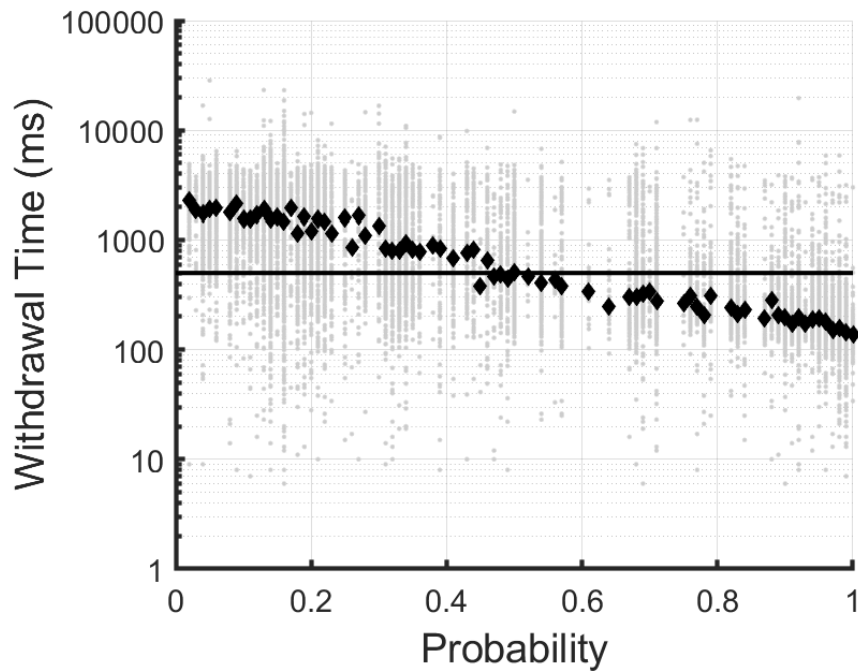
Figure 5.1: Withdrawal times for CW and LW trials across all datasets, plotted as a function of current amplitude normalized to the associated probability using the dataset's fitted psychometric parameters.

artificially imposed cutoffs of 350, 300, and 250 ms. Withdrawals once deemed correct for falling below the original 500 ms cutoff were now deemed late for falling above the newly imposed cutoffs. An obvious flaw with this approach was that the pattern of reinforcement no longer matched the order in which updated CWs and LWs occurred. Additionally, it remained unclear to what extent training the rat with a 500 ms cutoff would have affected the speed of its withdrawal. Nevertheless, this exercise confirmed the dependence of measured threshold values on the withdrawal cutoff (**Table 5.1**). The maximum percentagewise increases in threshold for 350, 300, and 250 ms were 30%, 54%, and 77%, respectively. The median percentagewise increases were 7%, 11%, and 17%.

Table 5.1: Detection thresholds calculated for artificially imposed withdrawal cutoffs of 350, 300, and 250 ms. The original 500-ms thresholds are shown for comparison.

Rat	Channel	Round	x_T (µA) (500 ms)	x_T (µA) (350 ms)	x_T (µA) (300 ms)	x_T (µA) (250 ms)
A	Multi	-	21.46	23.33	24.71	27.07
B	Multi	-	21.45	27.93	33.07	37.98
C	Multi	-	12.37	13.33	13.85	14.71
D	Multi	-	22.21	23.52	23.69	24.34
C	C1	-	49.42	53.07	54.93	57.58
C	C2	-	22.32	25.19	26.1	27.5
C	C4	-	96.76	103.13	113.87	120.52
C	P1	-	90.18	96.85	100.21	107.71
C	P2	-	96.26	100.04	100.92	104.35
C	P3	-	144.2	149.69	155.46	166.31
C	P4	-	98.74	104.57	108.36	113.74
D	C1	R1	54.38	56.96	57.62	58.46
D	C2	R1	54.82	57.06	58.85	61.26
D	C3	R1	49.05	53.72	55.75	59.22
D	C4	R1	57.75	59.79	59.98	60.97
D	P1	R1	81.47	93.06	101.72	108.39
D	P2	R1	138.15	143.87	149.57	154.17
D	P3	R1	125.98	130.7	133.01	137.05
D	C1	R2	43.57	44.87	46.43	48.12
D	C2	R2	35.32	39.22	41.69	44.34
D	C3	R2	52.49	54.64	55.13	56.13
D	C4	R2	98.34	106.19	111.73	116.38
D	P1	R2	142.51	155.35	160.49	167.87

One way to remove this dependence on withdrawal time would be to switch from the go/no-go task paradigm to a 2-alternative forced choice task (2AFC), in which the rat would signal its detection of the stimulus (or lack thereof) by choosing one of two manipulanda – be they retractable levers, nose-poke detectors, or food magazines fitted with infrared beam detectors. Precedent for using the 2AFC paradigm to measure detection thresholds in a rodent model has been provided by Huber et al. (2008), who trained optogenetic mice to select the left or right water port depending on the presence or absence of optical microstimulation in the barrel cortex. Notably, the rat had 10 s to respond after stimulus onset, rendering its reaction time following stimulus onset meaningless.

Table 5.2: Number of trials (CW + LW) and total session duration for the 23 datasets described in Chapter 4.

RatID	Channel	Round	Number of Trials	Total Session Duration
A	Multi	-	1496	9h 33m 57s
B	Multi	-	880	5h 15m 40s
C	Multi	-	1431	5h 23m 14s
D	Multi	-	1151	8h 20m 31s
C	C1	-	758	2h 38m 19s
C	C2	-	474	1h 44m 36s
C	C4	-	398	1h 33m 10s
C	P1	-	316	1h 27m 1s
C	P2	-	331	1h 21m 35s
C	P3	-	656	4h 15m 13s
C	P4	-	568	3h 8m 42s
D	C1	R1	1098	4h 31m25s
D	C2	R1	1146	5h 14m 36s
D	C3	R1	1087	5h 50m 3s
D	C4	R1	868	4h 20m 47s
D	P1	R1	997	7h 38m 42s
D	P2	R1	1135	9h 19m 12s
D	P3	R1	945	7h 57m 46s
D	C1	R2	981	6h 40m 46s
D	C2	R2	589	4h 37m 50s
D	C3	R2	730	5h 4m 18s
D	C4	R2	679	4h 18m 41s
D	P1	R2	1009	9h 4m 20s

5.2 Efficiency of Data Collection

Table 5.2 shows how many trials were performed for each of 23 datasets, along with how long it took to perform those trials. By plotting these data and fitting a simple linear model (**Figure 5.2**), we find that $D = 0.0063N - 0.2007$. This suggests that on average, each additional trial's worth of useful data required 0.0063 hours, or 23 seconds, to gather. There are several opportunities for increasing the efficiency of data collection. These include (but are not limited to) lowering the range of randomized insertion intervals from the present 1.5-4.5 s, lowering the duration of timeouts from 7 s, switching from the present ambulatory model to a head-fixed model, and moving away from MCS in favor of adaptive methods.
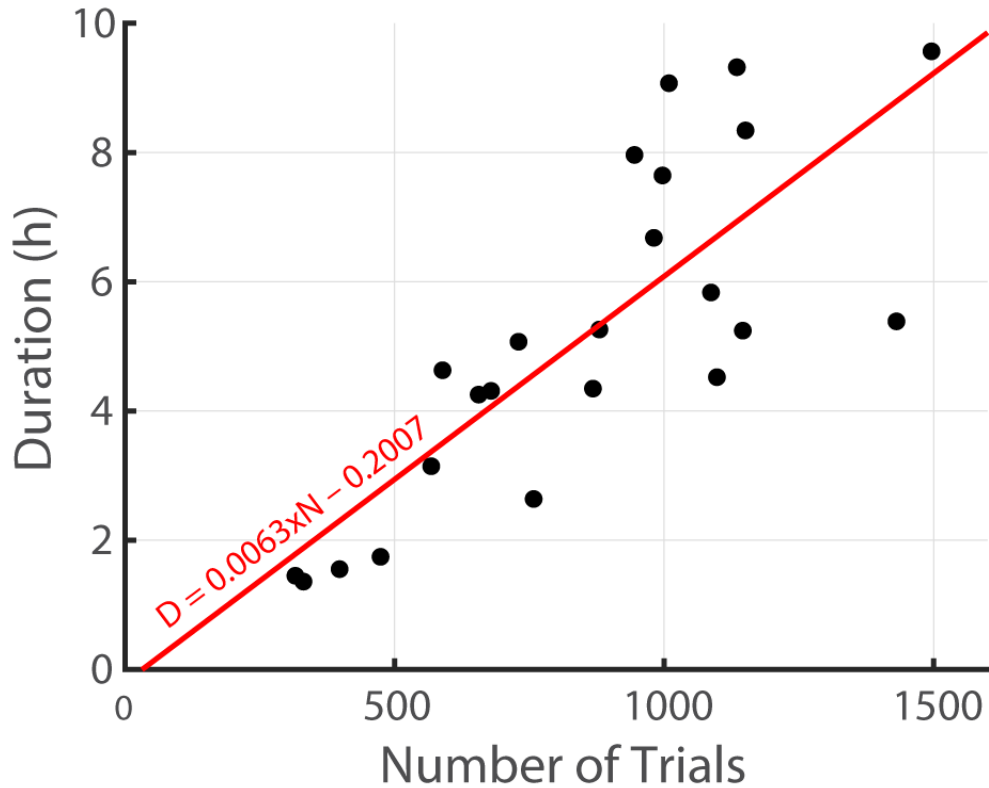
Figure 5.2: Duration of data collection as a function of the number of trials.

5.3   Ambulatory Model vs. Head-Fixed Model

5.3.1 Challenges Posed by the Ambulatory Model

The CRSNB model in its present iteration uses an ambulatory rat that is free to move about the Skinner box as it performs the go/no-go detection task. Having demonstrated that the model works, it is now feasible to address various pitfalls associated with free-moving rats. To start, building the slip-ring commutator assembly is a complex, time-consuming process (it can take 6 hours to build just one). When in use, it is highly vulnerable to gnawing by the rat despite being ensconced within

a protective layer of stainless-steel spring wrap, hardened with epoxy, and doused in bitter apple spray. Thus, preservation of commutator assemblies requires nonstop monitoring of the behavioral task over the webcam, which makes it impossible for the experimenter to do more productive work in parallel.

The slip-ring commutator also uses a latched, female Omnetics connector (#A76855-001) for interfacing with its male counterpart (#A76854-001) atop the head-cap. Not only are these latched connectors more expensive than their latchless brethren (#A79044-001, #A79045-001), but the skull-mounted male connector's latching mechanism must be situated well above the rim of the head-cap's titanium chamber to ensure continued access post-surgery. This necessitates the use of an especially tall Delrin screw cap that is prone to catching on nearby objects and ripping the head-cap off of the skull.

Additionally, the rat's freedom of movement means that there are periods when its attention may stray from the Skinner box's right wall that houses the various manipulanda. Instead of focusing on the task and generating data, the rat may instead resort to grooming, digging through the bedding underneath the Skinner box's barred floor, or falling asleep. This drastically lowers the rate of data collection.

Finally, reduced motor function following sciatic nerve transection and repair is conducive to the formation of ankle sores. If this sore grows too large, the pain it causes can interfere with the ambulatory rat's performance of the behavioral task and reduce its productivity to zero.

5.3.2 The Virtues of Head-Fixing

Instead of giving the rat free reign over its Skinner box domain, a potential solution to these challenges would be to severely restrict its movement during the behavioral task (e.g., Mayrhofer

et al., 2013). By securing the rat's head firmly in front of one or more lickometer spouts for dispensation of water (i.e., head-fixing), the need for the commutator assembly, constant monitoring, latched Omnetics connectors, and tall screw caps would be eliminated. The rat's performance of the task would no longer be beset by ankle sores. A head-fixed model would be particularly favorable to the inducement of leg paralysis by the application of botulinum toxin, in order to isolate the behavioral response to sensory axon recruitment. Head-fixing would also be conducive to a 2AFC task design and for increasing the efficiency of data collection.

5.4 Adaptive Methods

The present iteration of the CRSNB model selects current amplitudes based on MCS, in which each trial's amplitude is drawn from a predefined list without replacement. In its purest form, this method is agnostic as to the threshold's true location along the amplitude continuum – it simply applies the listed amplitudes the specified number of times. A problem with this approach is that without prior knowledge of the threshold's approximate location, chosen amplitudes may fall outside the psychometric curve's sloped domain, residing instead in uninteresting regions where the detection probability approaches γ or λ. The resulting data points are of little value for maximum likelihood estimation of psychometric parameters (based on **Equation (3.6)**), and needlessly increase the number of trials and duration of the experiment.

Having encountered this problem while gathering data for Rats A, B, and C, I adopted a pseudo-adaptive strategy for Rat D in which I assessed the distribution of amplitudes in relation to the emerging psychometric curve's sloped region between sessions, and added or removed amplitudes as necessary. While this certainly produced tighter estimates of threshold and slope (see **Figure**

4.8H,I), each measurement was based on hundreds of trials and required several hours of data collection (**Table 5.2**).

Adaptive algorithms (e.g., BEST PEST, QUEST, etc.) do not rely on a predefined list for amplitude selection, but instead calculate the next trial's amplitude based on the rat's performance in the preceding trials. By systematically varying the amplitude across successive trials, the algorithms eventually home in on an estimate of the threshold. The incorporation of an adaptive algorithm into the CRSNB model would reduce the number of trials (and hence the amount of time) needed to measure a threshold value. This would enable a more robust longitudinal analysis of threshold stability by allowing thresholds for multiple channels to be measured in a single day (rather than a 3-week span as was the case for Rat D). Shorter sessions made possible by adaptive algorithms would also enable the generation of high-resolution maps of detection thresholds across the nerve using multipolar stimulus configurations (i.e., current steering).

5.5 Further Recommendations

In the long-term, the CRSNB model should be adapted to a 2AFC discrimination task that will assess whether the MSE's selectivity in fact translates to an ability to evoke multiple discriminable sensations. Additionally, more simulation work is needed to understand the interplay of non-uniform sensory axon distribution, lead geometry, and peripheral channel extrusion on axon recruitment, and how these together produce the differential in detection thresholds for core and peripheral channels. Finally, the methods presented in this paper are not restricted to the MSE but can be harnessed for the investigation of other electrodes as well. For example, the micro-channel sieve electrode (MCSE) is an RE design with extruded transit zones that form electrically isolated "micro-channels" (FitzGerald et al., 2008; Lacour et al., 2008). Recent simulations by Coker et al.

(2019a, 2019b) have shown that the MCSE is well-suited for bidirectional interfacing of peripheral nerve tissue, as it allows for the simultaneous stimulation of sensory axons and recording of motor axons without stimulus artifact. The combined rat sciatic nerve and behavioral model could provide an ideal platform for evaluating the MCSE's bidirectional capabilities in an *in vivo* setting.

References

Adibi, M., and Arabzadeh, E. (2011). A Comparison of Neuronal and Behavioral Detection and Discrimination Performances in Rat Whisker System. *Journal of Neurophysiology* 105, 356–365. doi:10.1152/jn.00794.2010.

Akin, T., Najafi, K., Smoke, R. H., and Bradley, R. M. (1994). A Micromachined Silicon Sieve Electrode for Nerve Regeneration Applications. *IEEE Transactions on Biomedical Engineering* 41, 305–313. doi:10.1109/10.284958.

Antfolk, C., Björkman, A., Frank, S. O., Sebelius, F., Lundborg, G., and Rosen, B. (2012). Sensory feedback from a prosthetic hand based on airmediated pressure from the hand to the forearm skin. *Journal of Rehabilitation Medicine* 44, 702–707. doi:10.2340/16501977-1001.

Antfolk, C., D'alonzo, M., Rosén, B., Lundborg, G., Sebelius, F., and Cipriani, C. (2013). Sensory feedback in upper limb prosthetics. *Expert Review of Medical Devices* 10, 45–54. doi:10.1586/erd.12.68.

Ashmore, K., Cialdella, S., Giuffrida, A., Kon, E., Marcacci, M., and Di Matteo, B. (2019). ArtiFacts: Gottfried "Götz" von Berlichingen—The "Iron Hand" of the Renaissance. *Clinical Orthopaedics and Related Research®* 477, 2002–2004.

Atkins, D. J., Heard, D. C. Y. Y., and Donovan, W. H. (1996). Epidemiologic overview of individuals with upper-limb loss and their reported research priorities. *Journal of Prosthetics and Orthotics* 8, 2–11. doi:10.1097/00008526-199600810-00003.

Beeker, T. W., During, J., and Den Hertog, A. (1967). Artificial touch in a hand-prosthesis. *Medical and biological engineering* 5, 47–49. doi:10.1007/BF02478841.

Berning, K., Cohick, S., Johnson, R., Miller, L. A., CP, and Sensinger, J. W. (2014). Comparison of body-powered voluntary opening and voluntary closing prehensor for activities of daily life. *J Rehabil Res Dev* 51, 253–262. doi:10.1682/JRRD.2013.05.0123.

Beuche, W., and Friede, R. L. (1985). A new approach toward analyzing peripheral nerve fiber populations. II. Foreshortening of regenerated internodes corresponds to reduced sheath thickness. *Journal of Neuropathology & Experimental Neurology* 44, 73–84.

Biddiss, E., and Chau, T. (2007). Upper limb prosthesis use and abandonment: A survey of the last 25 years. *Prosthetics and Orthotics International* 31, 236–257. doi:10.1080/03093640600994581.

Boretius, T., Badia, J., Pascual-Font, A., Schuettler, M., Navarro, X., Yoshida, K., et al. (2010). A transverse intrafascicular multichannel electrode (TIME) to interface with the peripheral nerve. *Biosensors and Bioelectronics* 26, 62–69. doi:10.1016/j.bios.2010.05.010.

146

Bradley, R. M., Smoke, R. H., Akin, T., and Khalil, N. (1992). Functional regeneration of glossopharyngeal nerve through micromachined sieve electrode arrays. *Brain Research* 594, 84–90.

Branner, A., Stein, R. B., Fernandez, E., Aoyagi, Y., and Normann, R. A. (2004). Long-Term Stimulation and Recording with a Penetrating Microelectrode Array in Cat Sciatic Nerve. *IEEE Transactions on Biomedical Engineering* 51, 146–157. doi:10.1109/TBME.2003.820321.

Branner, A., Stein, R. B., and Normann, R. a (2012). Selective Stimulation of Cat Sciatic Nerve Using an Array of Varying-Length Microelectrodes Selective Stimulation of Cat Sciatic Nerve Using an Array of Varying-Length Microelectrodes. 1585–1594.

Brown, J. D., Kunz, T. S., Gardner, D., Shelley, M. K., Davis, A. J., and Gillespie, R. B. (2017). An Empirical Evaluation of Force Feedback in Body-Powered Prostheses. *IEEE Transactions on Neural Systems and Rehabilitation Engineering* 25, 215–226. doi:10.1109/TNSRE.2016.2554061.

Brushart, T. M. E. (1991). Central course of digital axons within the median nerve of macaca mulatta. *Journal of Comparative Neurology* 311, 197–209. doi:10.1002/cne.903110203.

Butovas, S., and Schwarz, C. (2007). Detection psychophysics of intracortical microstimulation in rat primary somatosensory cortex. *European Journal of Neuroscience* 25, 2161–2169. doi:10.1111/j.1460-9568.2007.05449.x.

Castro, J., Negredo, P., and Avendaño, C. (2008). Fiber composition of the rat sciatic nerve and its modification during regeneration through a sieve electrode. *Brain Research* 1190, 65–77. doi:10.1016/j.brainres.2007.11.028.

Cattin, A. L., and Lloyd, A. C. (2016). The multicellular complexity of peripheral nerve regeneration. *Current Opinion in Neurobiology* 39, 38–46. doi:10.1016/j.conb.2016.04.005.

Ceballos, D., Valero-Cabré, A., Valderrama, E., Schüttler, M., Stieglitz, T., and Navarro, X. (2002). Morphologic and functional evaluation of peripheral nerve fibers regenerated through polyimide sieve electrodes over long-term implantation. *Journal of Biomedical Materials Research* 60, 517–528. doi:10.1002/jbm.10099.

Charkhkar, H., Shell, C. E., Marasco, P. D., Pinault, G. J., Tyler, D. J., and Triolo, R. J. (2018). High-density peripheral nerve cuffs restore natural sensation to individuals with lower-limb amputations. *Journal of Neural Engineering* 15, 056002.

Childress, D. S. (1973). Powered Limb Prostheses: Their Clinical Significance. *IEEE Transactions on Biomedical Engineering* BME-20, 200–207. doi:10.1109/TBME.1973.324273.

Chiu, S. Y., Ritchie, J. M., Bogart, R. B., Stagg, D., Rogart, R. B., and Stagg, D. (1979). A quantitative description of membrane currents in rabbit myelinated nerve. *The Journal of ...* 292, 149–166. doi:10.1113/jphysiol.1979.sp012843.

Choi, A. Q., Cavanaugh, J. K., and Durand, D. M. (2001). Selectivity of multiple-contact nerve cuff electrodes: a simulation analysis. *IEEE Transactions on Biomedical Engineering* 48, 165–172. doi:10.1109/10.909637.

Coker, R. A., Zellmer, E. R., and Moran, D. W. (2019a). Micro-channel sieve electrode for concurrent bidirectional peripheral nerve interface. Part A: recording. *J. Neural Eng.* 16, 026001. doi:10.1088/1741-2552/aaefcf.

Coker, R. A., Zellmer, E. R., and Moran, D. W. (2019b). Micro-channel sieve electrode for concurrent bidirectional peripheral nerve interface. Part B: stimulation. *J. Neural Eng.* 16, 026002. doi:10.1088/1741-2552/aaefab.

Conzelman, J. E., Ellis, H. B., and O'Brien, C. W. (1953). Prosthetic Device Sensory Attachment (U.S. Patent 2,656,545).

Dario, P., Garzella, P., Toro, M., Micera, S., Alavi, M., Meyer, U., et al. (1998). Neural interfaces for regenerated nerve stimulation and recording. *IEEE Transactions on Rehabilitation Engineering* 6, 353–363. doi:10.1109/86.736149.

Darnall, B. D., Ephraim, P., Wegener, S. T., Dillingham, T., Pezzin, L., Rossbach, P., et al. (2005). Depressive symptoms and mental health service utilization among persons with limb loss: Results of a national survey. *Archives of Physical Medicine and Rehabilitation* 86, 650–658. doi:10.1016/j.apmr.2004.10.028.

Davis, T. S., Wark, H. A. C. C., Hutchinson, D. T., Warren, D. J., O'Neill, K., Scheinblum, T., et al. (2016). Restoring motor control and sensory feedback in people with upper extremity amputations using arrays of 96 microelectrodes implanted in the median and ulnar nerves. *Journal of Neural Engineering* 13, 36001. doi:10.1088/1741-2560/13/3/036001.

D'Errico, J. (2021). *fminsearchbnd, fminsearchcon*. Available at: https://www.mathworks.com/matlabcentral/fileexchange/8277-fminsearchbnd-fminsearchcon.

Dhillon, G. S., and Horch, K. W. (2005). Direct neural sensory feedback and control of a prosthetic arm. *IEEE Transactions on Neural Systems and Rehabilitation Engineering* 13, 468–472. doi:10.1109/TNSRE.2005.856072.

Dhillon, G. S., Lawrence, S. M., Hutchinson, D. T., and Horch, K. W. (2004). Residual function in peripheral nerve stumps of amputees: Implications for neural control of artificial limbs. *Journal of Hand Surgery* 29, 605–615. doi:10.1016/j.jhsa.2004.02.006.

Dillingham, T. R., Pezzin, L. E., and Mackenzie, E. J. (2002). Limb Amputation and Limb Deficiency : Epidemiology and Recent Trends in the United States. *South Med J* 95, 875–884. doi:10.1097/00007611-200208000-00018.

Dorrance, D. W. (1912). Artificial hand. Available at: https://patents.google.com/patent/US1042413A/en [Accessed September 21, 2021].

Edell, D. J. (1986). A Peripheral Nerve Information Transducer for Amputees: Long-Term Multichannel Recordings from Rabbit Peripheral Nerves. *IEEE Transactions on Biomedical Engineering* BME-33, 203–214. doi:10.1109/TBME.1986.325892.

Efron, B., and Tibshirani, R. J. (1993). *An Introduction to the Bootstrap*. Boca Raton, FL: Chapman & Hall.

Finch, J. (2011). The ancient origins of prosthetic medicine. *The Lancet* 377, 548–549.

FitzGerald, J. J., Lacour, S. P., McMahon, S. B., and Fawcett, J. W. (2008). Microchannels as axonal amplifiers. *IEEE transactions on biomedical engineering* 55, 1136–1146. doi:10.1109/TBME.2007.909533.

Friede, R. L., and Beuche, W. (1985). A new approach toward analyzing peripheral nerve fiber populations. I. Variance in sheath thickness corresponds to different geometric proportions of the internodes. *Journal of Neuropathology & Experimental Neurology* 44, 60–72.

Gaese, B. H., King, I., Felsheim, C., Ostwald, J., and Von Der Behrens, W. (2006). Discrimination of direction in fast frequency-modulated tones by rats. *JARO - Journal of the Association for Research in Otolaryngology* 7, 48–58. doi:10.1007/s10162-005-0022-7.

Hallin, R. G. (1990). Microneurography in relation to intraneural topography: somatotopic organisation of median nerve fascicles in humans. *Journal of Neurology, Neurosurgery & Psychiatry* 53, 736–744.

Hernigou, P. (2013). Ambroise Paré IV: the early history of artificial limbs (from robotic to prostheses). *International orthopaedics* 37, 1195–1197.

Hodgkin, A. L., and Huxley, A. F. (1952a). A quantitative description of membrane current and its application to conduction and excitation in nerve. *The Journal of Physiology* 117, 500–544.

Hodgkin, A. L., and Huxley, A. F. (1952b). Currents carried by sodium and potassium ions through the membrane of the giant axon of Loligo. *The Journal of Physiology* 116, 449–472. doi:10.1113/jphysiol.1952.sp004717.

Hodgkin, A. L., and Huxley, A. F. (1952c). The components of membrane conductance in the giant axon of Loligo. *The Journal of Physiology* 116, 473–496. doi:10.1113/jphysiol.1952.sp004718.

Hodgkin, A. L., and Huxley, A. F. (1952d). The dual effect of membrane potential on sodium conductance in the giant axon of Loligo. *The Journal of Physiology* 116, 497–506.

Hodgkin, A. L., Huxley, A. F., and Katz, B. (1952). Measurement of current-voltage relations in the membrane of the giant axon of Loligo. *The Journal of Physiology* 116, 424–448.

Huber, D., Petreanu, L., Ghitani, N., Ranade, S., and Hromádka, T. (2008). Sparse optical microstimulation drives behavior in freely moving mice Brain mechanisms of behavior (. 451, 61–64.

Jabaley, M. E., Wallace, W. H., and Heckler, F. R. (1980). Internal topography of major nerves of the forearm and hand: A current view. *Journal of Hand Surgery* 5, 1–18. doi:10.1016/S0363-5023(80)80035-9.

Johansson, R. S., and Vallbo, Å. B. (1983). Tactile sensory coding in the glabrous skin of the human hand. *Trends in Neurosciences* 6, 27–32. doi:10.1016/0166-2236(83)90011-5.

Kawamura, J. (1971). Sensory feedback device for the artificial arm. *Nihon Seikeigeka Gakkai zasshi* 45, 755.

Kelly, J. B., and Masterton, B. (1977). Auditory sensitivity of the albino rat. *Journal of Comparative and Physiological Psychology* 91, 930–936. doi:10.1037/h0077356.

Kovacs, G. T. A. A., Storment, C. W., and Rosen, J. M. (1992). Regeneration Microelectrode Array for Peripheral Nerve Recording and Stimulation. *IEEE Transactions on Biomedical Engineering* 39, 893–902. doi:10.1109/10.256422.

Kuiken, T. a, Dumanian, G. a, Lipshutz, R. D., Miller, L. a, and Stubblefield, K. a (2004). The use of targeted muscle reinnervation for improved myoelectric prosthesis control in a bilateral shoulder disarticulation amputee. *Prosthetics and Orthotics International* 28, 245–253. doi:10.3109/03093640409167756.

Kuiken, T. (2006). Targeted reinnervation for improved prosthetic function. *Physical Medicine and Rehabilitation Clinics of North America* 17, 1–13. doi:10.1016/j.pmr.2005.10.001.

Kuiken, T. A., Li, G., Lock, B. A., Lipschutz, R. D., Miller, L. A., Stubblefield, K. A., et al. (2011). Targeted Muscle Reinnervation for Reeal-time Myoelectric Control of Multifunction Artificial Arms. *Jama* 301, 619–628. doi:10.1001/jama.2009.116.Targeted.

Kuiken, T. A., Marasco, P. D., Lock, B. A., Harden, R. N., and Dewald, J. P. A. (2007a). Redirection of cutaneous sensation from the hand to the chest skin of human amputees with targeted reinnervation. *Proceedings of the National Academy of Sciences* 104, 20061–20066. doi:10.1073/pnas.0706525104.

Kuiken, T. A., Miller, L. A., Lipschutz, R. D., Lock, B. A., Stubblefield, K., Marasco, P. D., et al. (2007b). Targeted reinnervation for enhanced prosthetic arm function in a woman with a proximal amputation: a case study. *Lancet* 369, 371–380. doi:10.1016/S0140-6736(07)60193-7.

Labbe, S. A. (2018). Inspirations of War: Innovations in Prosthetics after the Civil War.

Lacour, S. P., Atta, R., FitzGerald, J. J., Blamire, M., Tarte, E., and Fawcett, J. (2008). Polyimide micro-channel arrays for peripheral nerve regenerative implants. *Sensors and Actuators, A: Physical* 147, 456–463. doi:10.1016/j.sna.2008.05.031.

Lago, N., Ceballos, D., Rodríguez, F. J., Stieglitz, T., and Navarro, X. (2005). Long term assessment of axonal regeneration through polyimide regenerative electrodes to interface the peripheral nerve. *Biomaterials* 26, 2021–2031. doi:10.1016/j.biomaterials.2004.06.025.

Lago, N., and Navarro, X. (2006). Correlation between target reinnervation and distribution of motor axons in the injured rat sciatic nerve. *Journal of neurotrauma* 23, 227–40. doi:10.1089/neu.2006.23.227.

Lago, N., Udina, E., Ramachandran, A., and Navarro, X. (2007). Neurobiological assessment of regenerative electrodes for bidirectional interfacing injured peripheral nerves. *IEEE Transactions on Biomedical Engineering* 54, 1129–1137. doi:10.1109/TBME.2007.891168.

Laing, D. G., Murray, K. E., Ryde, N., Cairncross, K. D., Ryde, N., King, M. G., et al. (1974). A Study of Olfactory Discrimination in the Rat with the Aid of a New Odor Delivery Technique. *Chemical Senses and Flavor* 1, 197–212.

Lefurge, T., Goodall, E., Horch, K., Stensaas, L., and Schoenberg, A. (1991). Chronically implanted intrafascicular recording electrodes. *Annals of biomedical engineering* 19, 197–207.

Loeb, G. E., and Peck, R. A. (1996). Cuff electrodes for chronic stimulation and recording of peripheral nerve activity. *Journal of Neuroscience Methods* 64, 95–103. doi:10.1016/0165-0270(95)00123-9.

MacEwan, M. R., Zellmer, E. R., Wheeler, J. J., Burton, H., and Moran, D. W. (2016). Regenerated sciatic nerve axons stimulated through a chronically implanted macro-sieve electrode. *Frontiers in Neuroscience* 10, 1–12. doi:10.3389/fnins.2016.00557.

Malagodi, M. S., Horch, K. W., and Schoenberg, A. A. (1989). An intrafascicular electrode for recording of action potentials in peripheral nerves. *Annals of biomedical engineering* 17, 397–410.

Mann, R. W., and Reimers, S. D. (1970). Kinesthetic Sensing for the EMG Controlled "Boston Arm." *IEEE Transactions on Man-Machine Systems* 11, 110–115.

Mannard, A., Stein, R. B., and Charles, D. (1974). Regeneration electrode units: implants for recording from single peripheral nerve fibers in freely moving animals. *Science* 183, 547–549.

Marks, A. F. F. (1969). Bullfrog nerve regeneration into porous implants. *Anat. Rec.* 163, 226.

Mayrhofer, J. M., Skreb, V., von der Behrens, W., Musall, S., Weber, B., and Haiss, F. (2013). Novel two-alternative forced choice paradigm for bilateral vibrotactile whisker frequency discrimination in head-fixed mice and rats. *Journal of Neurophysiology* 109, 273–284. doi:10.1152/jn.00488.2012.

Meek, S. G., Jacobsen, S. C., and Goulding, P. P. (1989). Extended physiologic taction: Design and evaluation of a proportional force feedback system. *Journal of Rehabilitation Research and Development* 26, 53–62.

Meijer, R., and Nazarpour, K. (2014). Multi-modal upper limb prosthetic device control using myoelectric signals.

Merzenich, M. M., and Jenkins, W. M. (1993). Reorganization of Cortical Representations of the Hand Following Alterations of Skin Inputs Induced by Nerve Injury, Skin Island Transfers, and Experience. *Journal of Hand Therapy* 6, 89–104. doi:10.1016/S0894-1130(12)80290-0.

Nannini, N., and Horch, K. (1991). Muscle recruitment with intrafascicular electrodes. *IEEE Transactions on Biomedical Engineering* 38, 769–776.

Navarro, X., Calvet, S., Butí, M., Gómez, N., Cabruja, E., Garrido, P., et al. (1996). Peripheral nerve regeneration through microelectrode arrays based on silicon technology. *Restorative Neurology and Neuroscience* 9, 151–160.

Navarro, X., Calvet, S., Rodriguez, F., Stieglitz, T., Blau, C., Buti, M., et al. (1998). Stimulation and recording from regenerated peripheral nerves through polyimide sieve electrodes. *J Peripher Nerv Syst.* 3, 91–101.

Navarro, X., Krueger, T. B., Lago, N., Micera, S., Stieglitz, T., and Dario, P. (2005). A critical review of interfaces with the peripheral nervous system for the control of neuroprostheses and hybrid bionic systems. *Journal of the Peripheral Nervous System* 10, 229–258. doi:10.1111/j.1085-9489.2005.10303.x.

Negredo, P., Castro, J., Lago, N., Navarro, X., and Avendaño, C. (2004). Differential growth of axons from sensory and motor neurons through a regenerative electrode: A stereological, retrograde tracer, and functional study in the rat. *Neuroscience* 128, 605–615. doi:10.1016/j.neuroscience.2004.07.017.

Nelder, J. A., and Mead, R. (1965). A simplex method for function minimization. *The computer journal* 7, 308–313.

Nerlich, A. G., Zink, A., Szeimies, U., and Hagedorn, H. G. (2000). Ancient Egyptian prosthesis of the big toe. *The Lancet* 356, 2176–2179.

Nguyen, Q. T., Sanes, J. R., and Lichtman, J. W. (2002). Pre-existing pathways promote precise projection patterns. *Nature Neuroscience* 5, 861–867. doi:10.1038/nn905.

Otte, A. (2020). 3D computer-aided design reconstructions and 3D multi-material polymer replica printings of the first "iron hand" of Franconian knight Gottfried (Götz) von Berlichingen (1480–1562): an overview. *Prosthesis* 2, 304–312.

Otte, A., and Hazubski, S. (2021). The Ancient Artificial Leg of Capua: First 3D Print after 2300 Years.

Otto, K. J., Rousche, P. J., and Kipke, D. R. (2005). Microstimulation in auditory cortex provides a substrate for detailed behaviors. *Hearing Research* 210, 112–117. doi:10.1016/j.heares.2005.08.004.

Patterson, P. E., and Katz, J. A. (1992). Design and evaluation of a sensory feedback system that provides grasping pressure in a myoelectric hand. *Journal of Rehabilitation Research and Development* 29, 1–8.

Petrini, F. M., Valle, G., Bumbasirevic, M., Barberi, F., Bortolotti, D., Cvancara, P., et al. (2019). Enhancing functional abilities and cognitive integration of the lower limb prosthesis. *Science Translational Medicine*. Available at: https://www.science.org/doi/abs/10.1126/scitranslmed.aav8939 [Accessed August 31, 2021].

Pillet, J., and Didierjean-Pillet, A. (2001). Aesthetic hand prosthesis: Gadget or therapy? Presentation of a new classification. *Journal of Hand Surgery* 26 B, 523–528. doi:10.1054/jhsb.2001.0658.

Prins, N. (2016). *Psychophysics: A Practical Introduction*. Academic Press.

Prior, R. E., Lyman, J., and Case, P. A. (1976). Supplemental Sensory Feedback for the VA/NU Myoelectric Hand. Background and Preliminary Designs. *Bulletin of Prosthetics Research* 10, 170–191.

Purves, D., Augustine, G. J., Fitzpatrick, D., Hall, W. C., LaMantia, A.-S., and White, L. E. (2012). "The Somatic Sensory System: Touch and Proprioception," in *Neuroscience* (Sinauer Associates, Inc.), 189–208.

Raspopovic, S., Capogrosso, M., Petrini, F. M., Bonizzato, M., Rigosa, J., Pino, G. D., et al. (2014). Restoring natural sensory feedback in real-time bidirectional hand prostheses. *Science Translational Medicine* 6, 222ra19. doi:10.1126/scitranslmed.3006820.

Rosen, J. M., Grosser, M., and Hentz, V. R. (1990). Preliminary experiments in nerve regeneration through laser-drilled holes in silicon chips. *Restorative Neurology and Neuroscience* 2, 89–102. doi:10.3233/RNN-1990-2205.

Rosset, F. (1916). Artificial Limbs (German Patent 301,108).

Savastano, L. E., Laurito, S. R., Fitt, M. R., Rasmussen, J. A., Gonzalez Polo, V., and Patterson, S. I. (2014). Sciatic nerve injury: A simple and subtle model for investigating many aspects of nervous system damage and recovery. *Journal of Neuroscience Methods* 227, 166–180. doi:10.1016/j.jneumeth.2014.01.020.

Seddon, H. J. (1942). A classification of nerve injuries. *British medical journal* 2, 237.

Shannon, G. F. (1979). A myoelectrically-controlled prosthesis with sensory feedback. *Medical & biological engineering & computing* 17, 73–80. doi:10.1007/BF02440956.

Shukla, G. D., Sahu, S. C., Tripathi, R. P., and Gupta, D. K. (1982). A psychiatric study of amputees. *British Journal of Psychiatry* 141, 50–53. doi:10.1192/bjp.141.1.50.

Stewart, J. D. (2003). Peripheral nerve fascicles: anatomy and clinical relevance. *Muscle & nerve* 28, 525–541. doi:10.1002/mus.10454.

Stieglitz, T., Beutel, H., and Meyer, J.-U. (1997). A flexible, light-weight multichannel sieve electrode with integrated cables for interfacing regenerating peripheral nerves. *Sensors and Actuators A: Physical* 60, 240–243. doi:10.1016/S0924-4247(97)01494-5.

Stuttgen, M. C., Ruter, J., and Schwarz, C. (2006). Two Psychophysical Channels of Whisker Deflection in Rats Align with Two Neuronal Classes of Primary Afferents. *Journal of Neuroscience* 26, 7933–7941. doi:10.1523/JNEUROSCI.1864-06.2006.

Suzuki, G. I., Ochi, M., Shu, N., Uchio, Y., and Matsuura, Y. (1998). Sensory neurons regenerate more dominantly than motoneurons during the initial stage of the regenerating process after peripheral axotomy. *NeuroReport* 9, 3487–3492. doi:10.1097/00001756-199810260-00028.

Sweeney, J. D., Mortimer, J. T., and Durand, D. (1987). Modeling of Mammalian Myelinated Nerve for Functional Neuromuscular Stimulation. *IEEE 9th Annual Conference of the Engineering in Medicine and Biology Society* 3, 1577–1578.

Tan, D., Schiefer, M., Keith, M. W., Anderson, R., and Tyler, D. J. (2015). Stability and selectivity of a chronic, multi-contact cuff electrode for sensory stimulation in a human amputee. *International IEEE/EMBS Conference on Neural Engineering, NER* 12, 859–862. doi:10.1109/NER.2013.6696070.

Tan, D. W., Schiefer, M. A., Keith, M. W., Anderson, J. R., Tyler, J., and Tyler, D. J. (2014). A neural interface provides long-term stable natural touch perception. *Science Translational Medicine* 6. doi:10.1126/scitranslmed.3008669.

Thurston, A. J. (2007). Paré and prosthetics: the early history of artificial limbs. *ANZ journal of surgery* 77, 1114–1119.

Tyler, D. J., and Durand, D. M. (1997). A slowly penetrating interfascicular nerve electrode for selective activation of peripheral nerves. *IEEE transactions on rehabilitation engineering* 5, 51–61.

Tyler, D. J., and Durand, D. M. (2002). Functionally selective peripheral nerve stimulation with a flat interface nerve electrode. *IEEE Transactions on Neural Systems and Rehabilitation Engineering* 10, 294–303. doi:10.1109/TNSRE.2002.806840.

Tyler, D. J., and Durand, D. M. (2003). Chronic response of the rat sciatic nerve to the flat interface nerve electrode. *Annals of biomedical engineering* 31, 633–642.

Uchida, N., and Mainen, Z. F. (2003). Speed and accuracy of olfactory discrimination in the rat. *Nature Neuroscience* 6, 1224–1229. doi:10.1038/nn1142.

Veraart, C., Grill, W. M., and Mortimer, J. T. (1993). Selective Control of Muscle Activation with a Multipolar Nerve Cuff Electrode. *IEEE Transactions on Biomedical Engineering* 40, 640–653. doi:10.1109/10.237694.

Wallman, L., Zhang, Y., Laurell, T., and Danielsen, N. (2001). The geometric design of micromachined silicon sieve electrodes influences functional nerve regeneration. *Biomaterials* 22, 1187–1193.

Wichmann, F. A., and Hill, N. J. (2001a). The psychometric function: I. Fitting, sampling, and goodness of fit. *Perception & Psychophysics* 63, 1293–1313. doi:10.3758/BF03194544.

Wichmann, F. A., and Hill, N. J. (2001b). The psychometric function: II. Bootstrap-based confidence intervals and sampling. *Perception and Psychophysics* 63, 1314–1329.

Zellmer, E. R. (2014). *Restoring Upper Extremity Mobility through Functional Neuromuscular Stimulation using Macro Sieve Electrodes*. Washington University in St. Louis.

Zellmer, E. R., MacEwan, M. R., and Moran, D. W. (2018). Modelling the impact of altered axonal morphometry on the response of regenerative nervous tissue to electrical stimulation through macro-sieve electrodes. *J. Neural Eng.* 15, 026009. doi:10.1088/1741-2552/aa9e96.

Ziegler-Graham, K., MacKenzie, E. J., Ephraim, P. L., Travison, T. G., and Brookmeyer, R. (2008). Estimating the Prevalence of Limb Loss in the United States: 2005 to 2050. *Archives of Physical Medicine and Rehabilitation* 89, 422–429. doi:10.1016/j.apmr.2007.11.005.